To the Graduate Council:

I am submitting herewith a dissertation written by Mark Allen Davis entitled "Magnetic Resonance Imaging: The Development and Evaluation of Several Gd-DTPA Derivatives for Use as MRI Contrast Enhancement Agents and The Application of Boron-11 Spectroscopy and Imaging for the Detection and Localization of a BNCT Agent In-Vivo." I have examined the final copy of this dissertation for form and content and recommend that it be accepted in partial fulfillment of the requirements for the degree of Doctor of Philosophy, with a major in Chemistry.

George W. Kabalka, Major Professor

We have read this dissertation
and recommend its acceptance:

D. C. Kleinfelter

Charles Feigerle

Leo Huang

Accepted for the Council:

Vice Provost
and Dean of The Graduate School

MAGNETIC RESONANCE IMAGING: THE DEVELOPMENT AND EVALUATION OF SEVERAL Gd-DTPA DERIVATIVES FOR USE AS MRI CONTRAST ENHANCEMENT AGENTS

AND

THE APPLICATION OF BORON-11 SPECTROSCOPY AND IMAGING FOR THE DETECTION AND LOCALIZATION OF A BNCT AGENT IN-VIVO

A Dissertation

Presented for the

Doctor of Philosophy

Degree

The University of Tennessee, Knoxville

Mark Allen Davis

May 1990

DEDICATION

The author wishes to dedicate this work to his wife, Julia Woods Davis, for without her love, understanding and motivation, completion of this degree would not have been possible. Her support through it all has been greatly appreciated.

ACKNOWLEDGEMENTS

The author wishes to thank Dr. George W. Kabalka for his research ideas, advise and generous support during the course of this work. The author also wishes to thank Dr. Peter Bendel and Dr. Elisha Berman for their ideas and assistance associated with the boron magnetic resonance work. Further appreciation goes to Dr. Leaf Huang, Dr. Eric Holmberg and Dr. Kazuo Maruyama for their assistance with the biochemical studies. A special thanks goes to Dr. Edward Buonocore for the opportunity to utilize the facilities at the Biomedical Imaging Center, Knoxville, Tennessee.

The author also wishes to thank his wife, Julia Woods Davis, not only for her love and support but also for the typing of this entire manuscript as well as the incorporation of all the figures. Appreciation goes to Dr. Laila Guindi for the drawing of the molecular structures. Finally, a special thanks goes to my parents, Richard and Dorothy Davis, and my in-laws, Roddy and Ann Woods, for their confidence and support.

ABSTRACT

Gadolinium diethylenetriaminepentaacetic acid (Gd-DTPA) has been extensively investigated as a contrast enhancement agent for MRI because of its low toxicity and high spin number (7/2). The high solubility and rapid excretion of Gd-DTPA make it an ideal agent for mapping vascular spaces and leakage through the blood-brain barrier. However, it is limited in value for imaging the liver since the complex does not accumulate in that organ. Recently, in order to extend its utility toward contrast enhancement of the liver, a Gd-DTPA derivative which contained hydrophobic alkyl chains that were connected to the ionic polar moiety via an amide linkage was developed and used to construct a new class of paramagnetic gadolinium-labeled liposomes (GLL). This agent effectively enhanced the T_1 relaxation of liver tissue. However, it exhibited a very long retention time in that organ. In this work, new Gd-DTPA derivatives were developed to be utilized as GLL agents that would retain the relaxation properties of the previous Gd-DTPA amide derivative but also exhibit a shorter biological lifetime. This was accomplished utilizing two approaches: the existing Gd-DTPA amide complex was modified by decreasing the length of the hydrophobic alkyl chains and new Gd-DTPA derivatives were developed that would degrade more rapidly into Gd-DTPA residues. The preparation, biological clearance rate and contrast enhancing abilities of these new agents are discussed.

Boron neutron capture therapy (BNCT) is brachyradiotherapy by heavy charged particles which depends on the successful delivery of agents enriched with the boron-10 isotope to a targeted organ or lesion. A current problem associated

with BNCT is the inability to noninvasively verify, localize and quantitate in-vivo boron content. Magnetic resonance spectroscopy (MRS) and imaging (MRI) are potentially valuable techniques for the non-invasive evaluation of BNCT agents in-vivo. In this work, boron-11 magnetic resonance techniques were developed for the detection and localization of a representative BNCT agent in solution as well as in animal tissue. The results of these endeavors, from both a spectroscopic and imaging standpoint, as well as the problems encountered when attempting to achieve these purposes are discussed.

TABLE OF CONTENTS

Part I. The Development and Evaluation of Several Gd-DTPA Derivatives for Use as MRI Contrast Enhancement Agents

LIST OF FIGURES

CHAPTER I

BASIC INTRODUCTION TO MAGNETIC RESONANCE IMAGING

A. INTRODUCTION

Nuclear Magnetic Resonance (NMR) spectroscopy has become a valuable tool for chemists, biochemists and biologists since the first observation of the NMR phenomenon in 1946.[1] More recently, this technique has become useful in the field of medicine with the development of Magnetic Resonance Imaging (MRI). MRI has proven to be an important diagnostic imaging modality much like computerized tomography (CT) with the advantage that ionizing radiation is not required. This technique has become the imaging modality of choice for the brain, spinal cord and central nervous system due to its superior ability in depicting soft tissue contrast.

The idea of applying NMR to the study of biological systems originated over 30 years ago with the detection of the first proton MR signal from living tissue.[2] The first two-dimensional proton MR image of a water sample was generated in 1972 and the first application to a human was in 1977.[3,4] It is now possible to utilize NMR signals from the hydrogen in human tissues (water, fat, etc.) to generate images of the type shown in Figure 1. In this chapter, the basic principles and techniques of MRI will be discussed.

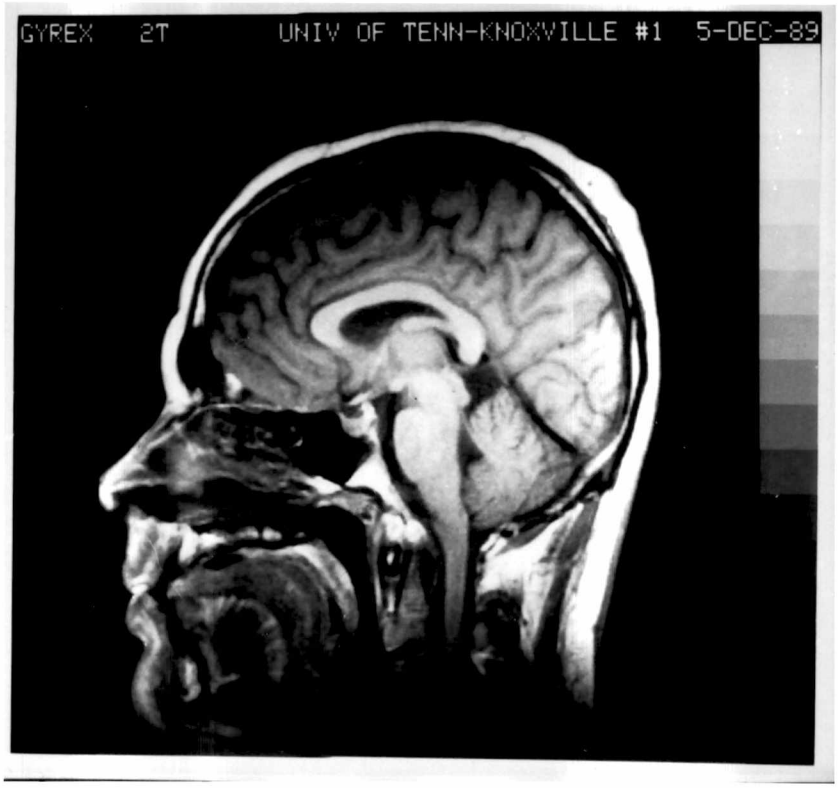

Figure 1. Sagittal MRI of the human head.

B. BASIC NMR THEORY

There have been exhaustive treatments of the theory of the NMR phenomenon.[5-7] Although a vigorous treatment is beyond the scope of this thesis, an understanding of the basic principles of NMR is important to the appreciation of its application in imaging: only those nuclei that have nuclear spin can undergo the NMR phenomenon; all nuclei possessing spin contain either an odd number of protons, an odd number of neutrons or both; the spin of a nucleus is represented by the nuclear spin quantum number I (if their mass number is odd, the nuclei have I values that are integral multiples of 1/2, I=n/2, whereas nuclei with even mass numbers but odd atomic numbers have integral values of I). There are many nuclei that experience the NMR phenomenon but this discussion will be restricted to the hydrogen nucleus (I=1/2) because it is the predominant nucleus used in MRI due to its strong NMR signal and large natural abundance in living systems.[8]

1. Magnetic Properties of the Proton

Since nuclei bear electric charges, their spinning produces a magnetic moment, μ, expressing the strength and direction of the magnetic field surrounding the nucleus. The fields produced by these magnetic dipoles are analogous to those of a tiny bar magnet and when exposed to a static magnetic field, B_o, the randomly oriented magnetic dipoles line up with the magnetic field. For the proton, there are two allowable basic states with orientations "parallel" and "antiparallel" corresponding to magnetic quantum numbers $m = +1/2$ and $-1/2$ which pertain to a low- and high-energy state, respectively.

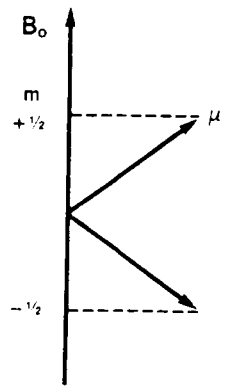

The spin vectors experience a torque when subjected to a magnetic field analogous to a spinning top in the earth's gravitational field. As a result, they precess around the axis of the magnetic field at a rate given by the Larmor relationship,

$$f=\omega/2\pi=\gamma B_o/2\pi \qquad (1)$$

where f is the resonance frequency in Hz, ω is the angular frequency in radians per second, γ is the gyromagnetic ratio and B_o is the static magnetic field. The gyromagnetic ratio is a constant for a particular nucleus and represents the ratio of the magnetic moment of the nucleus to the angular momentum of the nucleus.

The two spin states of the proton are almost of equal probability due to the small energy difference between them. In fact, for protons in a magnetic field of 1.5 T (15,000 gauss), the fractional excess population in the lower level is approximately 1×10^{-5}.[5] Since there are slightly more nuclei parallel to the field, there will be a net magnetization Mz that is oriented along the direction of the magnetic field (B_o is always aligned along the z axis in an xyz coordinate system).

It is this net magnetic moment that is responsible for the induction of the NMR signal in the receiver coil.

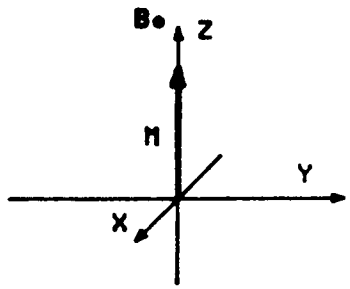

2. Resonance Phenomenon

Resonance is the induction of transitions between two different energy states which for a proton are the m = +1/2 and m = -1/2 states. The energy required to produce a transition in NMR is the difference in magnetic energy between the states. Resonance can be induced in NMR by applying a radiofrequency (RF) energy that is equal to the Larmor frequency, flipping the magnetic moments from their m = +1/2 (lower energy) to their m = -1/2 (higher energy) states. The energy difference between the two states is $\gamma h B_o/2\pi$ where h is Planck's constant.

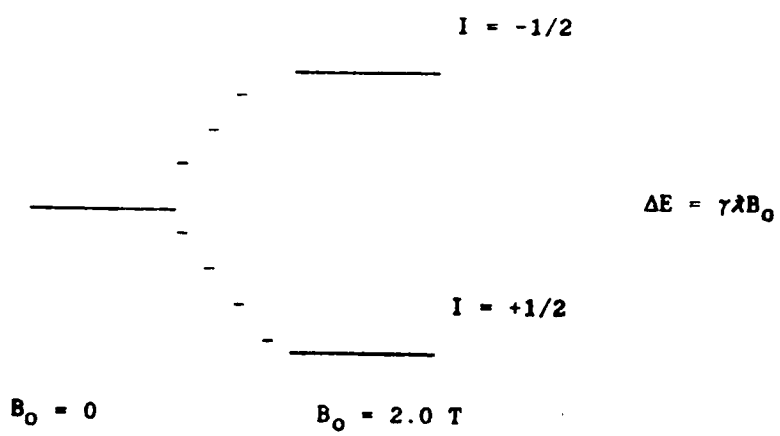

Magnetic resonance absorption can only be detected if transverse magnetization (i.e. magnetization perpendicular to B_o) is created. The transverse magnetization component Mxy is time dependent and thus, according to Faraday's law of induction, can induce a voltage in a receiver coil. The longitudinal magnetization Mz is static and does not meet the requirements for magnetic induction. Transverse magnetization is created by applying a small radiofrequency (RF) field of amplitude B_1 in a direction perpendicular to the main field B_o. The net magnetization Mz now experiences a torque from the radiofrequency field B_1 forcing the magnetization to rotate about it. The angle of rotation Θ, the so-called RF flip angle, is defined by

$$\Theta=\gamma B_1 \tau \qquad (2)$$

where τ is the duration of the B_1 field. If the duration of the B_1 field is such that the net magnetization is rotated by an angle of 90 degrees, it will become transverse or perpendicular to the static field.

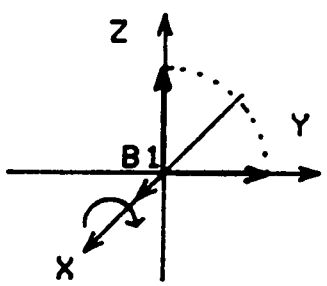

Once the B_1 field is removed, the magnetization is subjected to the effect of the static field B_o only and hence precesses about it. If a receiver coil is positioned with it's axis oriented along the y axis of the xyz coordinate system, an AC voltage is induced in the coil. The signal induced is a cosine whose amplitude is

proportional to the transverse magnetization Mxy and whose frequency is equal to the Larmor resonance frequency. However, the transverse magnetization does not persist but decays to zero exponentially as does the amplitude of the detected voltage. Therefore, the induced voltage V can be defined by

$$V \propto Mxy^{\circ} e^{-\tau / T2^{*}} \cos \omega \tau \qquad (3)$$

where Mxy° is the initial transverse magnetization following the 90 degree RF pulse, $T_2{}^*$ is a time constant representing exponential decay and τ is the time interval between the pulse and the voltage measurement. This equation represents a damped oscillation that is called a "free induction decay" or FID signal.

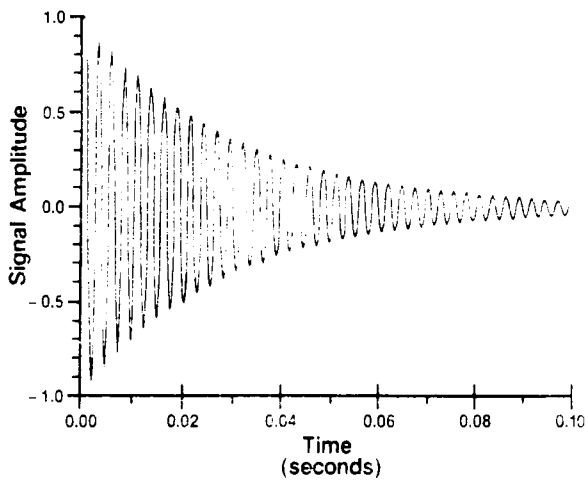

The FID is a time-domain spectrum representing the time evolution of the transverse magnetization. By a mathematical process known as Fourier transformation, a conventional frequency-domain NMR spectrum can be obtained from the FID. The position of the signal corresponds to the frequency (in Hz) of oscillation of the transverse magnetization.

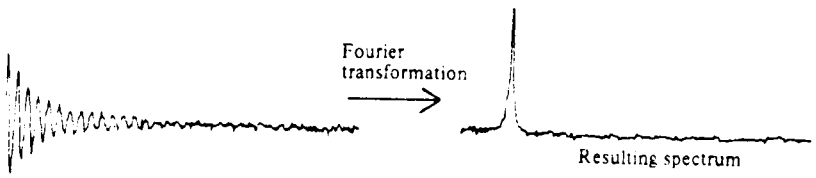

3. Relaxation Mechanisms

The process by which the transverse magnetization decays exponentially following excitation by an RF pulse is termed "relaxation". There are two important relaxation mechanisms termed as longitudinal (T_1) and transverse (T_2) relaxation. These two mechanisms are key processes in distinguishing different tissues in MR images.[9]

Longitudinal relaxation is the return of the magnetization vector along the z axis to it's equilibrium value, Mo, following perturbation. This return to equilibrium is exponential and is described by the following equation, which shows that the intensity of Mz increases with time:

$$dMz/dt=(Mo-Mz)/T_1 \qquad (4)$$

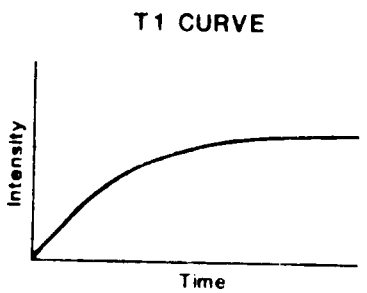

T_1 relaxation occurs due to an exchange of energy between the nuclear spins and their molecular lattice (i.e. environment); therefore, this process has been

termed "spin-lattice" relaxation. The exchange of energy with the environment is the result of the interaction of the nucleus with fluctuating magnetic fields in the environment. The two major pathways which give rise to fluctuating magnetic fields are fields due to magnetic moments of other nuclei (intra- and inter-molecular) and fields associated with spins of unpaired electrons. The second pathway is the most important contribution if paramagnetic species are present, as will be discussed later.

Transverse relaxation is the decay of the magnetization vector in the xy plane following perturbation. This decay of magnetization is exponential and is defined by the following equation, which shows that the intensity of Mxy decreases with time:

$$dMxy/dt=-Mxy/T_2 \quad (5)$$

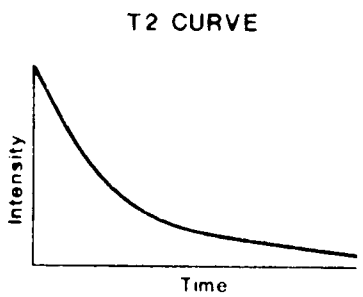

T_2 relaxation results from the interactions of the spins of the various nuclei being observed; therefore, this process has been termed "spin-spin" relaxation. The interactions involve the absorption of energy of one nucleus that is released from a neighboring nucleus. These interactions cause the nuclei to precess at slightly different rates resulting in a dephasing of the magnetization vector. This spread of resonance frequencies results in a subsequent net loss of transverse magnetization.

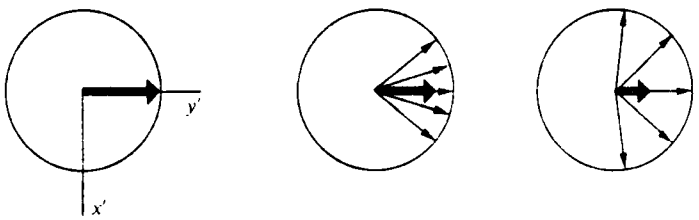

The greater the spread of frequencies, the more rapidly Mxy decays. The relationship between the frequency spread of the signal and the transverse relaxation can be expressed as

$$\Delta f_{1/2}=1/\pi T_2 \qquad (6)$$

where $\Delta f_{1/2}$ is the difference in frequency of the signal at half height (i.e. linewidth of the signal).

The magnitude of the T_1 and T_2 relaxation rates can be associated with molecular motion. The molecular motion of concern is the tumbling of molecules and is defined by the correlation time (τ_c). Large molecules have longer correlation times than small molecules because they tumble more slowly. There is an inverse relationship between transverse relaxation and correlation time; i.e. as τ_c increases, the T_2 relaxation time decreases. The relationship between τ_c and the T_1 relaxation time is not as straightforward.

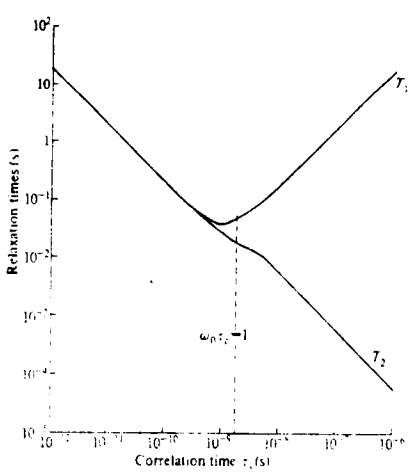

4. The Spin Echo Experiment

Following a 90 degree pulse, the signal should decay with a time constant T_2 but the transverse magnetization actually decays much faster with a time constant T_2^* (eqn. 3), the effective transverse relaxation rate. The reason for this increased rate in magnetization decay is due to spatial inhomogeneity of the magnetic field B_o. Spins at different locations experience slightly different magnetic fields causing them to have different precession frequencies. Consequently, the spins begin to dephase and as a result the transverse magnetization decays faster than it would on the basis of T_2 processes alone.

In order to avoid this increased decay rate, one can create and then observe a "spin echo" (instead of simply detecting the FID) in which the dephasing magnetization is rephased upon signal detection. The pulse sequence used to generate a spin echo signal involves application of the 90 degree pulse which is followed by the application of a 180 degree pulse at time τ and then detection of the signal at time 2τ.

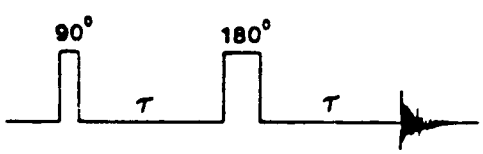

The process by which the spin echo pulse sequence rephases the dephased magnetization caused by magnetic field inhomogeneities is illustrated in Figure 2. Immediately following the application of the 90 degree pulse along the x axis, all of the transverse magnetization is aligned along the y axis. During time τ, the magnetization begins to dephase due to inhomogeneities in which some of the

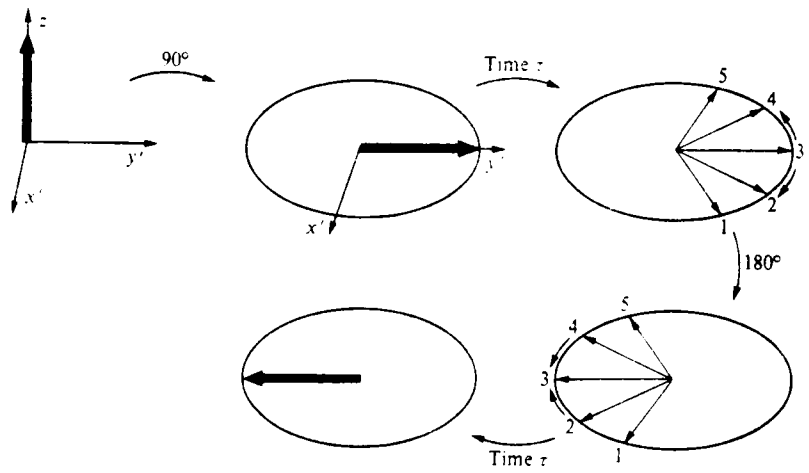

Figure 2. Magnetization behavior during a spin echo experiment.

magnetization vectors precess at a faster rate than others. Application of a 180 degree pulse along the x axis after time τ rotates the magnetization vectors around the x axis. Following the 180 degree pulse, the various components continue to precess at their original speeds until they come together to form an echo along the y axis after an additional time τ. The end result is the detection of a signal that has decayed due to natural T_2 processes only. For this reason, the spin echo sequence has become the most common sequence employed in MRI due to the time constraints imposed by the imaging process.[10]

5. Two-Dimensional NMR

Recently, there have been extensive treatments of the theory of two-dimensional NMR spectroscopy.[11-13] A basic understanding of the 2D-NMR experiment is essential in order to understand the imaging process because it also involves the collection of information along more than one dimension. The basic 2D-NMR pulse sequence consists of the preparation period, the evolution time (t_1) and the detection time (t_2).

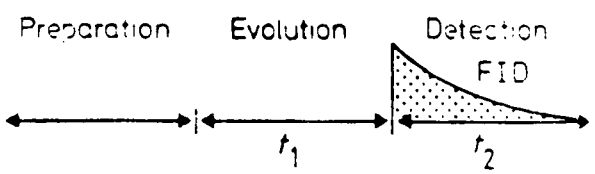

The preparation period simply involves the excitation of the spins with an RF pulse. The detection time is identical to that in one-dimensional NMR spectroscopy in which the FID is sampled at various time increments. The time t_2 provides, after Fourier transformation, the second frequency axis (f_2) of a 2D-NMR spectrum.

The uniqueness of 2D-NMR spectroscopy is that a second time variable, the evolution time, is introduced. The time t_1 is increased in a stepwise fashion (i.e. incremented) and for each t_1 increment a separate FID is detected in t_2 . Thus, a signal is obtained which is a function of two time variables, t_1 and t_2. A series of f_2 spectra is obtained upon Fourier transformation of each of the FIDs which differ from one another in the intensities and/or phases of the individual signals according to the different t_1 increments. A second Fourier transformation over t_1, perpendicular to the f_2 dimension, results in a spectrum which is a function of two frequencies, f_2 (horizontal) and f_1 (vertical). The concept of detecting a signal that contains two variables is also used in MRI.

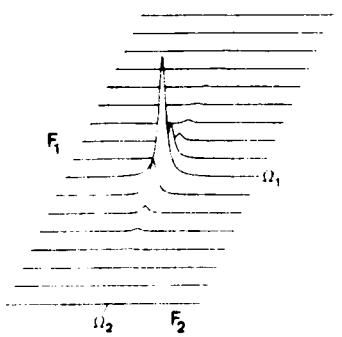

C. PRINCIPLES OF IMAGING

There are several thorough descriptions involving the theory of magnetic resonance imaging.[2,9,10,14,15] This section introduces the basic principles and various techniques of imaging. Most MR images are generated from the signal of the hydrogen in the water present in human tissues.[16,17] The human body is approximately 80% water and the signal from the water hydrogen is a simple, single peak. In addition, hydrogen has the highest relative sensitivity toward the NMR

phenomenon when compared to other nuclei.[18] There are other nuclei whose signals can be detected from human tissues; they can also be utilized for spectroscopy and/or image production as will be discussed later.

If the entire volume of a water sample is subjected to a very homogeneous magnetic field, all the protons will resonate at the same frequency and only one signal will be obtained. The resonance frequency of the water protons in all human tissue are identical regardless of the organ from which the signal is obtained. Therefore, there must be some means to differentiate or spatially resolve those signals that arise from various anatomical positions in order to generate images that yield useful diagnostic information.

1. Spatial Encoding - The Effect of Magnetic Field Gradients

Since the resonance frequency is dependent on the magnetic field strength, the spatial localization of an NMR signal can be achieved by the use of a magnetic field gradient; i.e. the magnetic field is altered along a selected direction. The idea of using linear magnetic field gradients in NMR is almost as old as NMR itself but the concept was not applied to imaging until much later by Lauterbur.[2,19] In an experiment using a linear field gradient, the entire volume of a sample (e.g. water) is subjected to the gradient (Δ B)and the resonance frequency of the individual nuclei within that sample depends on the location of the nuclei relative to the gradient. The magnitude of the individual resonance frequencies will depend upon the strength of the magnetic field at their individual gradient locations. The signal that is detected in the presence of the gradient extends over a range of frequencies and the signal intensity at an individual frequency depends upon the number of nuclei

positioned at the gradient location corresponding to that frequency. This concept is illustrated in Figure 3. If a linear gradient is applied in a horizontal direction along a rectangular water sample in which the proton density is the same throughout the sample, the resulting ^{1}H NMR signal will appear as shown in Figure 3a. However, if a gradient is oriented in a direction passing through the diameter of a cylindrical water sample in which the proton density is different throughout the sample, the resulting ^{1}H NMR signal will appear as shown in Figure 3b. Finally, if a gradient is oriented along the same direction through a cylindrical water sample containing a plastic strip having no protons, the resulting ^{1}H NMR signal will appear as shown in Figure 3c.

The steps for obtaining spatial localization of an NMR signal are illustrated in Figure 4. If three water samples are placed at different positions in a magnetic field gradient that is aligned along the horizontal axis, the signals obtained from each position have a frequency that is directly proportional to the strength of the field. The summed signal which contains the different frequencies can be Fourier transformed to give a plot of signal intensity versus frequency. The conversion from frequency to location is trivial for modern computerized equipment. Because the values of the individual magnetic fields along the axis are known, each frequency value can be assigned to a unique position. This type of one dimensional spectrum which determines the proton density along the direction of the gradient is called a "projection."

The concept of projections can be utilized to generate two-dimensional images of objects by a method termed "projection reconstruction." Projection reconstruction,

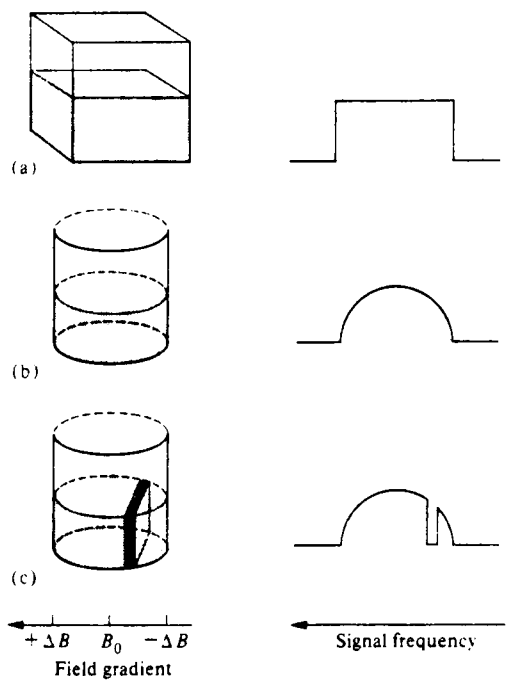

Figure 3. The effect of a magnetic field gradient on an NMR signal.

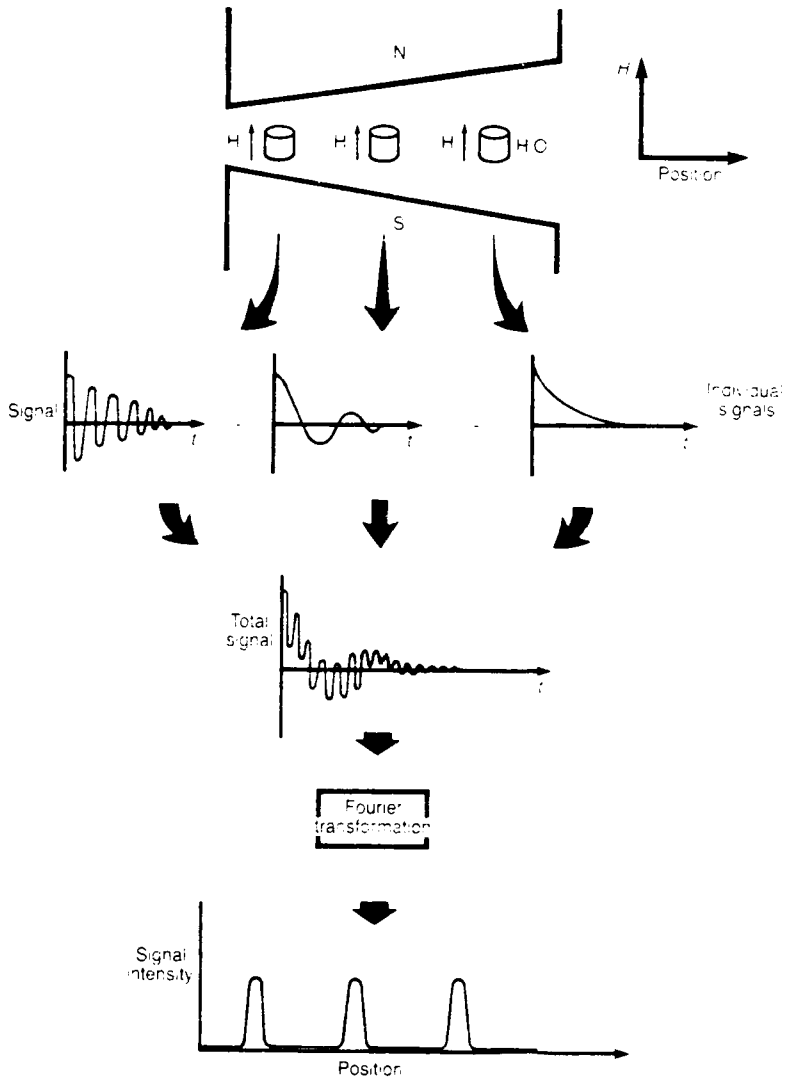

Figure 4. Steps for obtaining spatial information in NMR.

which has been widely used for image formation in x-ray computed tomography (CT), was the method utilized to generate the first two-dimensional MR images.[2,20] The technique involves the generation of a series of projections of the object to be imaged by rotating a gradient in small angular increments. The desired angle of the gradient, G_θ, can be achieved by suitably mixing two orthogonal gradients and is defined by the following equation,

$$G_\theta = G_x \cos\theta + G_y \sin\theta \qquad (7)$$

where G_x and G_y are the two orthogonal gradients. The resulting projections can be used to reconstruct an image of the object. The number of projections that must be used depends upon the spatial resolution that is required.[21] For example, in order to obtain a two-dimensional image containing n x n picture elements (pixels), n^2 pieces of information must be available for there to be sufficient information to fully define the image. This means that if the signal representing each one-dimensional projection consists of n data points, the field gradient must be applied in n different directions.

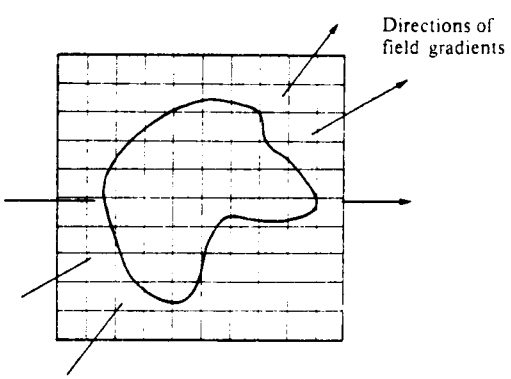

The simplest and most widely used reconstruction method is the "back projection" technique.[21,22] This technique is illustrated in Figure 5. The various

projections are back projected onto the image plane and superimposed to reconstruct an approximate image of the original objects. One problem with this technique is that various regions lying outside the object have also been assigned a non-zero spin density. This effect gives rise to what are termed "star artifacts" around regions of high density when a large number of projections are used. For this reason, the individual projections are usually "filtered" prior to back projection by convolution with a mathematical function in order to improve the image.

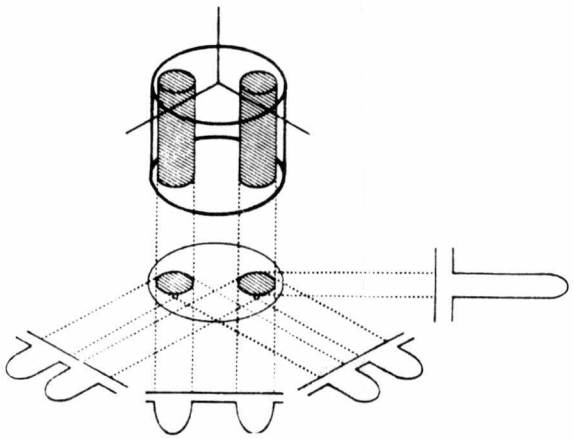

Figure 5. The principle of image reconstruction by backprojection.

There are several problems associated with the use of projection reconstruction to produce MR images. The method is sensitive to magnetic field inhomogeneities causing image distortion. Also, the technique does not permit the generation of nonquadratic (nonsquare) acquisition matrices. Although back projection was used initially in MRI, it has been largely abandoned with the development of two-dimensional Fourier transform (2D-FT) methods.[23]

2. Two-Dimensional MRI - Spin Warp Imaging

The major difference between the projection reconstruction and the 2D-FT method lies in the fact that the latter uses orthogonal gradients only. The simplest image is that obtained from a single slice in which two steps are required. First, only the nuclei in the slice of interest are excited, and then the information from that slice is encoded in two dimensions to obtain spatial localization. The intensity of the signal at any given location depends upon the concentration of the nuclei at that location and their T_1 and T_2 relaxation times, which will be discussed later.

By the combination of a frequency-selective RF pulse and a magnetic field gradient perpendicular to the imaging plane, it is possible to restrict the excitation to a selected portion of nuclei in the total spin system by which slice selection is achieved.[24] The bandwidth of the RF pulse (Δf) and the magnitude of the slice-select gradient (G_z for slice selection oriented along the z direction) determines the thickness of the slice. The basic principle of selective excitation is illustrated in Figure 6. Since γ for the proton is 4250 Hz/gauss, a gradient of 0.1 gauss/cm produces a variation of 425 Hz over a distance of 1 cm. The RF pulse can be adjusted to excite only a narrow band of frequencies by manipulation of the pulse width, PW. The PW of the excitation carrier frequency produces a modulation giving a band of frequencies defined by the following equation:

$$\Delta f = 1/PW \tag{8}$$

For a PW = 2 ms, the bandwidth (Δf) is 500 Hz; therefore, only nuclei in a slice of approximately 1.1 cm thick centered on the resonance point, $B_o \pm \Delta B$, will be excited by the soft RF pulse. If the gradient is turned off and the receiver turned on

at this point, a single signal will be observed from the nuclei in the excited region only. The location of the slice can be changed by applying a dc offset to the magnetic field gradient or by moving the RF carrier frequency. The slice thickness can be reduced by either increasing the strength of the gradient or decreasing the RF bandwidth. The orientation of the slice relative to the xyz coordinate system depends on whether the slice selection gradient is applied with the x, y or z gradient coil.

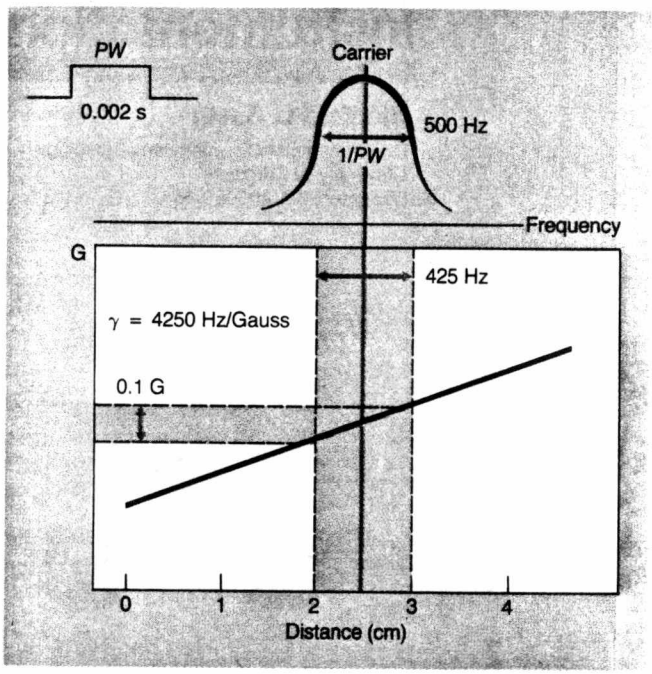

Figure 6. Basic principle of selective excitation.

After application of the slice select gradient (G_z for example), spatial encoding is performed to obtain spatial information within the slice.[25] This involves a phase encoding period followed by a readout period during which frequency encoding occurs. These two processes will be discussed in further detail.

Following slice selection, all the spins in the slice have been rotated to the xy plane. The slice selection gradient is then turned off and a second orthogonal gradient (G_y for example) is turned on for a fixed time period (t_y) during which phase encoding occurs. This process is illustrated in Figure 7. If a phase encoding gradient is applied along the vertical direction with increasing gradient strength toward the top of the figure, the various nuclei will precess at different frequencies depending on their position relative to the gradient. All the spins in row A have precessed through a given phase angle. The spins in row B have precessed through a smaller phase angle because they are in a weaker magnetic field. The spins in row C have precessed through an even smaller phase angle, and so on. If the gradient G_y is turned off at the end of the phase encoding period, all the spins will resonate at the same frequency but their phases will be different. The end result is that the various phase angles can be used to encode distance information along the y direction by the following equation,

$$\phi_y=\gamma G_y t_y y \tag{9}$$

where ϕ_y is the phase angle corresponding to a particular position along the y axis.

Following phase encoding, frequency encoding occurs to obtain the second dimension of spatial information. This process is illustrated in Figure 8. After the phase encoding gradient is turned off, a third gradient orthogonal to the previous two (G_x for example) is applied along the horizontal direction with increasing gradient strength toward the left of the figure for a fixed time period (t_x). During this time (i.e. the readout period), the receiver is turned on and a signal is acquired in which the spins in column 1 precess at one frequency, the spins in column 2 precess at a

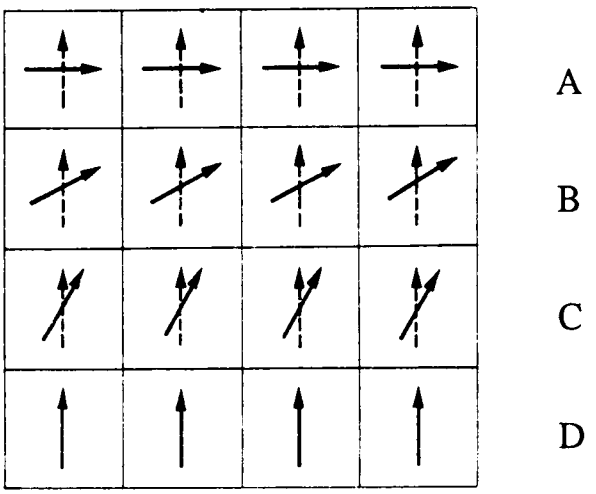

Figure 7. Principle of phase encoding.

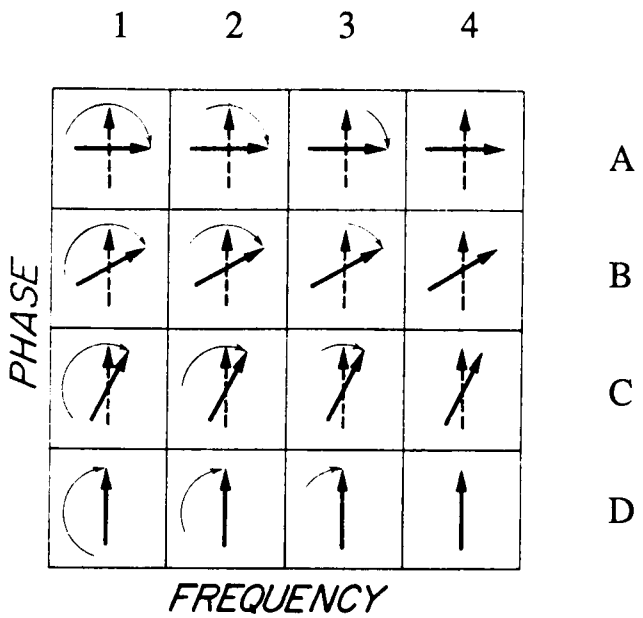

Figure 8. Two-dimensional matrix of pixels resulting from both phase and frequency encoding.

different frequency, the spins in column 3 precess at an even different frequency and so on. The magnitude of the frequency depends upon the strength of the magnetic field at the individual locations and is represented by the length of the thin curved line. The various frequencies can be used to encode distance information along the x direction by the following equation,

$$\omega_x = \gamma G_x x \tag{10}$$

where ω_x is the resonance frequency corresponding to a particular position along the x axis. The end result of the combined encoding processes is the generation of a two-dimensional matrix in which each element (pixel) has it's own individual set of ϕ_y and ω_x values.

The phase encoding period (t_y) is equivalent to the evolution time (t_1) in 2D NMR spectroscopy. However, in 2D-FT imaging the spins move at different frequencies during t_y due to the application of a linear gradient rather than from chemical shift differences that occur during t_1. Therefore, in imaging it is convenient to keep t_y fixed and increase the strength of the phase encoding gradient G_y rather than increasing t_1 by increments as is done in 2D-FT spectroscopy. As the strength of the phase encoding gradient is changed, the phase angles of the various signals along the phase encoding axis will change as a function of their different frequencies. For each increment of G_y, a separate signal which is a function of two gradients is detected during frequency encoding. This signal is doubly Fourier transformed to a signal that is a function of two frequencies which are related to spatial distances. Fourier transformation of *n* signals (obtained from *n* increments of the phase encoding gradient), each containing *n* data points, results in a two-dimensional matrix

with n^2 picture elements (pixels). The resulting image that is displayed contains intensity information at each pixel, where light regions indicate high signal intensity and dark regions indicate low signal intensity. The differences in signal intensities provide contrast to the image, as will be discussed later.

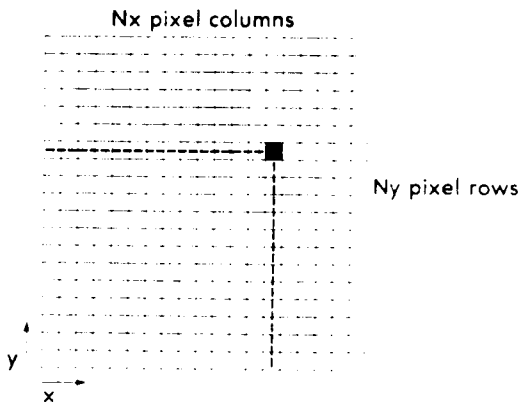

A pulse timing diagram for a typical 2D-FT spin warp imaging sequence is illustrated in Figure 9. The signal is detected as an echo due to the time constraints imposed by the process. The slice select gradient is turned on during application of the 90 and 180 degree pulse to generate selective excitation. The phase encoding gradient is turned on between the application of the 90 and 180 degree pulse and is incremented for each repetition of the sequence. The frequency encoding gradient is turned on during detection of the echo. The time-to-echo (TE) is the time that elapses between the application of the 90 degree pulse and the detection of the signal. The time-to-repeat (TR) is the time that elapses between repetition of the sequence. The values of TE and TR can be altered in order to obtain various levels of contrast in an image, as will be discussed later.

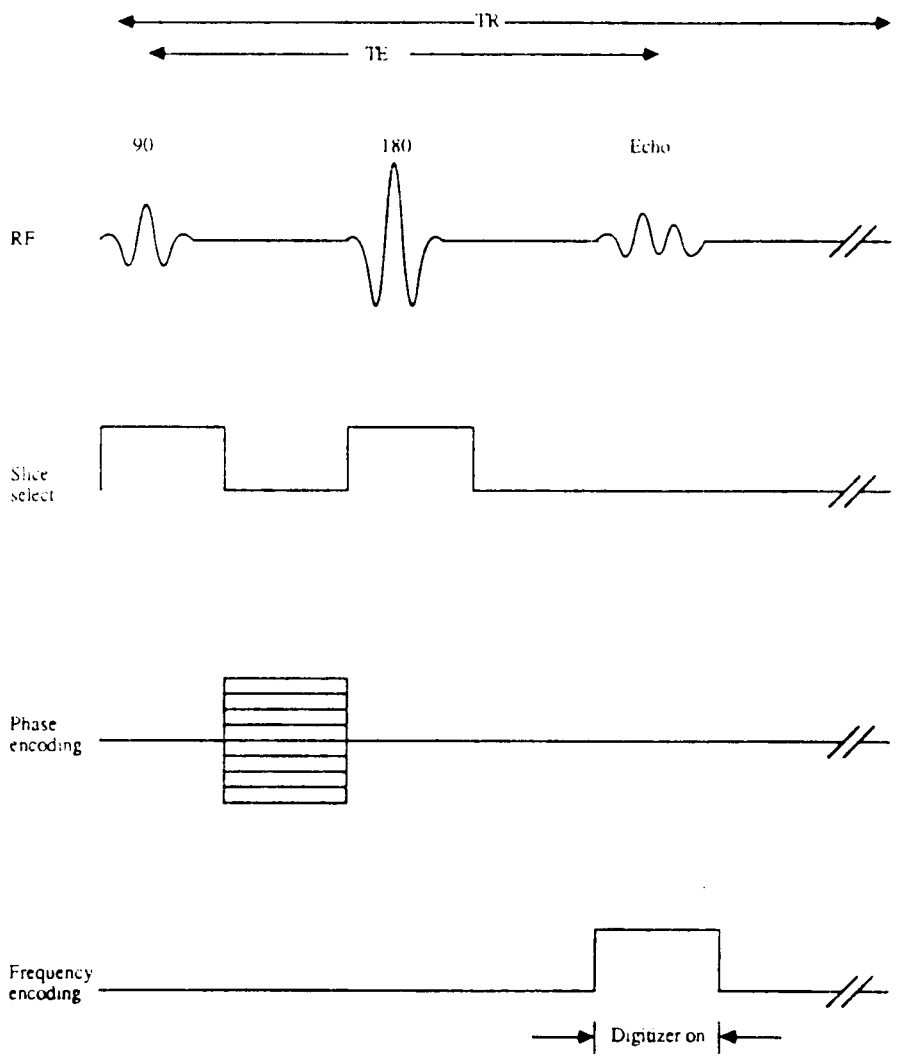

Figure 9. Spin echo imaging pulse sequence.

The total time required to obtain an image using the spin warp sequence is determined by the number of increments of the phase encoding gradient, the number of excitations per increment of the phase encoding gradient and the repetition time (TR). The number of increments of phase encoding is dictated by the resolution requirements and the number of excitations is dictated by the signal-to-noise (S/N) requirements. Although the TR can be varied, it is necessary to wait for a period of time to permit recovery of equilibrium magnetization (related to T_1 relaxation) before repeating the sequence. Therefore, TR values are typically between 0.5 and 2.0 seconds, whereas the imaging sequence illustrated in Figure 9 requires a few hundred milliseconds at most. As a result, it takes 2 - 10 minutes to acquire the raw data for a single slice image.

Since the actual data acquisition time is only a fraction of the repetition time, it is possible to use the time during which the spins in the first slice are recovering to obtain data from a different slice location that was left undisturbed by the first sequence.[26] The timing and sequence are identical in all respects except that the slice selection gradient is given a dc offset to select spins at a different location. This approach is known as multislice imaging and permits 2-32 slices to be obtained in the time previously required for a single slice (the number of slices obtainable is limited by TR). At present, multislice imaging is the most efficient method used for diagnostic purposes.[27]

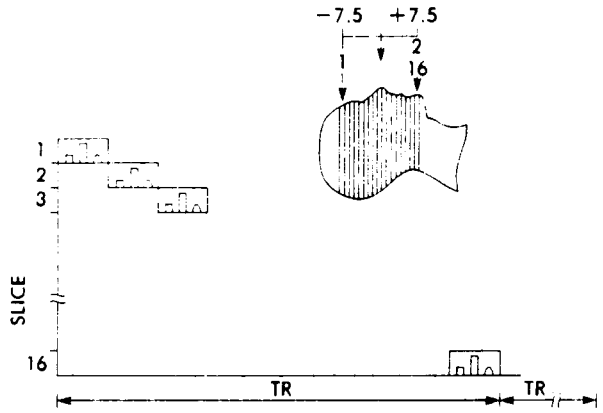

3. Other MR Imaging Methods

In addition to the conventional spin warp imaging technique, there are a multitude of other methods that have been developed for MRI.[9,27,28] In this section, several of these methods which pertain to the work presented later will be discussed.

One method, which is simply a modification of the spin warp technique, is known as "gradient echo" imaging. In lieu of generating an echo by means of a 180 degree pulse as is done in spin echo imaging, an echo can be generated by the use of gradient reversal.[29] This concept is illustrated in Figure 10. Following a 90 degree pulse, a gradient is turned on for a time τ to produce a sharply decaying FID. At some later time, the same gradient is turned back on with the same strength but reversed direction. When the gradient is reversed, spins initially in a stronger field are now in a weaker one, thus the spins will rephase to produce an echo peak after time τ. This modification to the spin warp imaging sequence is performed with the frequency encoding gradient. Therefore, gradient echo imaging is similar to spin echo imaging except for deletion of the 180 degree RF pulse. However, the energy absorption from the 90 degree pulse limits how rapidly the 180

degree pulse can be applied which limits the minimum obtainable TE in the spin echo pulse sequence. Since gradient echos do not require a 180 degree pulse, much shorter TE's can be obtained.[30] For this reason, fast imaging sequences usually rely on gradient echos. The ability to obtain short TE values is also advantageous in the signal detection of species having short T_2 relaxation times which will be discussed later.[31]

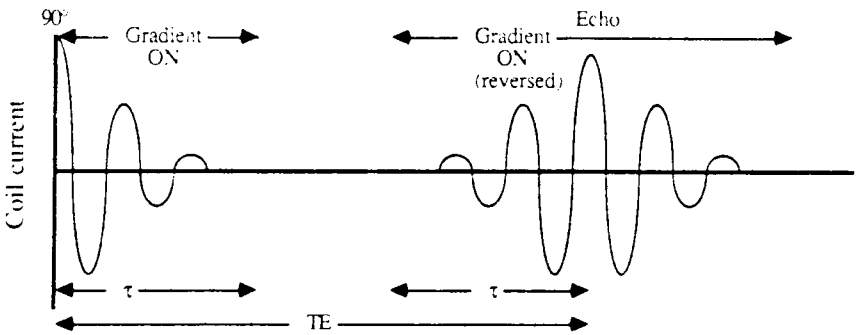

Figure 10. Gradient echo pulse sequence.

Three-dimensional MR imaging can be accomplished by a simple extension of the 2D-FT imaging method.[9,15] In this method, data are simultaneously acquired from the entire volume to be imaged. A hard RF pulse (i.e. narrow width) is applied in the absence of a slice select gradient to excite all the spins within the volume. Following the pulse, two phase encoding gradients (G_z and G_y for example) are applied to produce spatial encoding along the two corresponding axis. The two gradients can be applied consecutively or simultaneously. The third dimension of spatial information is acquired by the application of a frequency encoding gradient

orthogonal to the previous two (G_x for example) during acquisition of the signal. The two dimensions of phase encoding data are collected by an amplitude cycling of the gradients. In other words, the process is repeated with the same value of the z gradient but at incrementally different values of the y gradient. After a suitable number of G_y steps have been performed, an incrementally different value of G_z is applied and the set of G_y increments is run again. This process is repeated for every value of G_z and the final result is a 3D data set that can be Fourier transformed three times and converted to distance information. The resulting image is displayed as slices along one of the phase encoding axes. If 16 slices oriented along the z direction are required, 16 different values of G_z must be applied.

The volume imaging process requires a relatively long acquisition time because of the large number of imaging cycles required. Also, the image reconstruction process is rather long because of the additional data. For these reasons, 3D-FT imaging is commonly not used because in most cases the same information can be acquired more rapidly by the 2D multislice technique. The general advantage of 3D volume imaging compared to 2D slice imaging is the ability to create thinner contiguous slices, thereby increasing the signal-to-noise (S/N) ratio because signals are acquired from the entire volume rather than a single slice.

Due to the relationship between MR spectroscopy and imaging, "chemical shift" imaging can be accomplished. In this technique, one dimension of spatial localization is sacrificed in order to obtain chemical shift information [i.e. the difference in resonance frequency of different species (water vs fat for example)]. There have been several methods developed for the generation of chemical shift

images.[32,33] The simplest method involves the acquisition of the signal in the absence of a frequency encoding gradient, which allows for the recovery of high-resolution spectral information due to the precession of the individual spins at different frequencies depending on their chemical shifts. This requires the use of an extremely homogeneous magnetic field when the gradient is not being applied. If the frequency encoding gradient was eliminated from the 3D imaging sequence described above, triple Fourier transformation of the data would result in an image in which one of the dimensions gives chemical shift information and the other two give spatial information. Another alternative is to insert a variable evolution time (identical to t_1 in conventional 2D spectroscopy) in place of one of the phase encoding gradients resulting in individual precessions from chemical shift differences. After that time period, phase encoding and frequency encoding would provide spatial information along two dimensions. The process is repeated for incrementally different t_1 values. The principal application of chemical shift imaging to date has been the separation of the fat and water contributions in hydrogen imaging.[34,35]

4. Image Characteristics - Resolution and Contrast

The resolution in an image is determined by the minimum volume (voxel) that contains a sufficient number of nuclei to give a detectable signal (i.e. spatial resolution can be improved by reducing the voxel size). Since each voxel is represented in the image by a single pixel intensity, all the signals within the voxel are averaged together. The averaging is a blurring process in which the amount of blurr is determined by the size of the voxel. Blurring reduces the contrast and limits the ability to separate (resolve) structures located close together. The size of each

individual voxel is determined by the slice thickness, the field of view (FOV - dimensions of the area to be imaged) and the matrix size (determined by the number of phase encoding steps and the number of data points acquired in each echo). Resolution can be increased by decreasing the slice thickness, decreasing the FOV or increasing the matrix size.

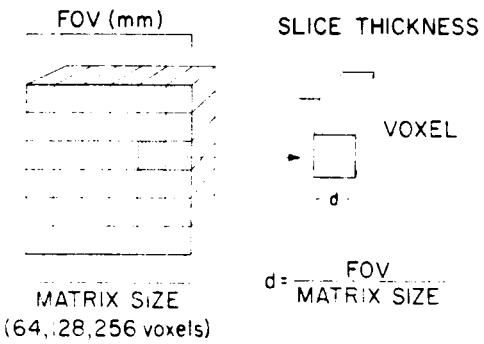

The maximum resolution obtainable is limited by the signal-to-noise (S/N) ratio. In order to obtain a high signal strength in relation to a specific noise level, there is a limit to the minimum voxel size that can be used. Although the S/N ratio can be increased by increasing the number of measurements (excitations) per phase encoding increment, this is impractical to a certain extent for clinical procedures because it increases the scan time. In fact, four times the number of excitations is required to increase the S/N by a factor of two. The selection of an imaging protocol that maximizes image quality involves a compromise between the signal-to -noise ratio and spatial resolution. Most imaging instruments produce images with 256 x 256 or 512 x 512 data matrices on slices a few millimeters to 1.5 cm thick. Currently, a resolution of less than 1 mm is attainable.[36]

Variations in the signal intensities from the various voxels give rise to image contrast. The factors that control the intensity of the signal from a given voxel are the concentration of the observed nuclei (proton density) and the relaxation times (T_1 and T_2) of the signal.[37] These factors are intrinsic to the nature of the tissue. The proton density of different tissues varies throughout the human body. In addition, tissues have different T_1 and T_2 values depending on their environment and physiological state. It has been well documented that the relaxation times of normal and diseased tissues are different.[38,39] The signal intensity is determined by the pulse sequence used and it's timing. By selecting proper combinations of TR and TE in the spin echo sequence, the image can display contrast related mainly to differences in the proton density, T_1 relaxation time or T_2 relaxation time of the tissue.

The value of TR can be used to control contrast related to tissue T_1 differences.[40] This concept is illustrated in Figure 11 which shows the spin-lattice relaxation curves for two different species. In conventional pulse FT spectroscopy a time $\geq 5T_1$ is required between the repetition of the pulse sequence to permit complete recovery of magnetization. If a sample contains species with different T_1 values and the repetition time is less than five times the longest T_1 value, the intensities of the lines in the spectrum are distorted. Those with short T_1 values are enhanced and those with longer T_1 values are diminished due to saturation of the signal. The TR in the spin echo pulse sequence produces the same effect in an image. A bright or high-intensity voxel corresponds to a species with a relatively short T_1 value that has recovered considerable magnetization during TR as compared

to a dark or low-intensity voxel corresponding to a species with a long T_1 value. To emphasize T_1 contrast, the TR is set to where the difference between the two curves is the largest. The unique feature of the image is that the chemical species observed in the different voxels is the same (H_2O) but their spin-lattice relaxation rates are different due to the nature of the tissue. Images obtained by this technique are called T_1 weighted images.

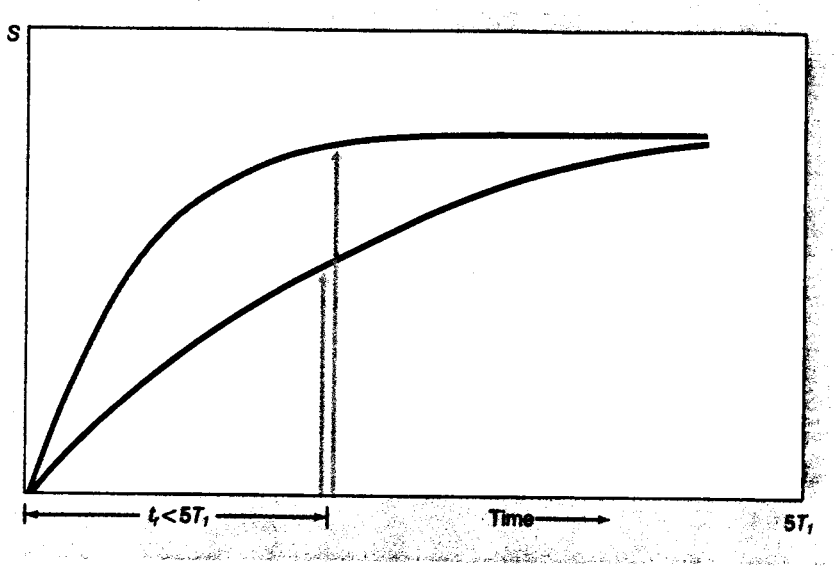

Figure 11. T_1 relaxation curves for two different species.

The value of TE can be used to control contrast related to tissue T_2 differences.[40] This concept is illustrated in Figure 12 which shows the spin-spin relaxation curves for two different species. The intensity of the signal detected depends upon the time period between the initial pulse and acquisition of the signal. When using long TE values, a voxel in which T_2 values are long will still give an appreciable signal resulting in a high intensity whereas a voxel in which T_2 values are

short will have a very weak signal resulting in a low intensity due to an appreciable loss of transverse magnetization before signal detection. To emphasize T_2 contrast, the TE is set to where the difference between the two curves is the largest. Images obtained in this manner are called T_2 weighted images.

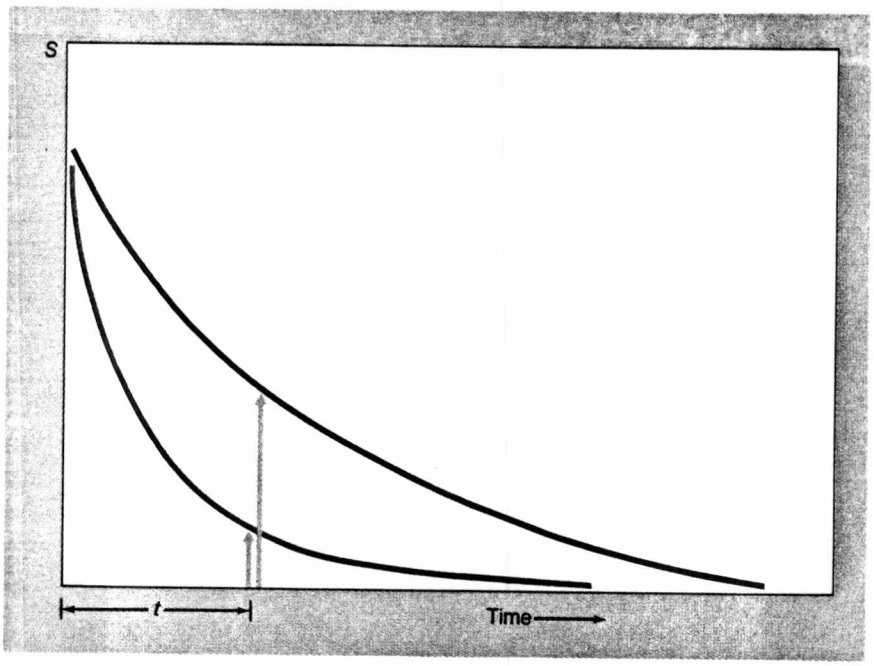

Figure 12. T_2 relaxation curves for two different species.

T_1 weighted images are achieved by the use of a short TR which maximizes the T_1 effects and the use of a short TE which minimizes the contribution of T_2 effects. T_2 weighted images are achieved by the use of a long TE which maximizes T_2 effects and the use of a long TR which minimizes the contribution of T_1 effects. The use of a sufficiently long TR and a short TE will produce images in which contrast or intensity depends primarily on concentration. The long TR minimizes the effects of T_1 and the short TE minimizes the effects of T_2 allowing the effects of

proton density to dominate. Images obtained in this manner are said to be spin density weighted.

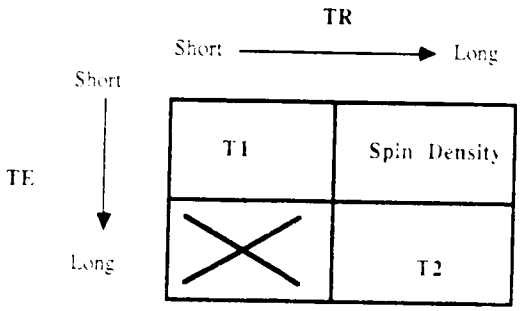

5. Instrumentation

Imaging equipment is divided into three groups: whole body medical imagers, small bore imagers (animal units) and conventional high-resolution NMR spectrometers equipped with imaging capabilities (NMR microscopes). This discussion will be limited to the whole body imaging units because the work presented in this manuscript was performed on this type of instrument. These units contain large magnets having approximately a 1 meter horizontal bore in which a human or other objects can be placed.

Magnets used for whole body imaging fall into one of three categories: resistive, superconducting and permanent. Resistive and permanent magnets have been built for whole body imaging with field strengths in the range of 0.15 to 0.4 T (1 Tesla = 10,000 gauss). Superconducting magnets are the most commonly employed because they can attain considerably higher magnetic field strengths resulting in increased sensitivity.[41,42] Superconducting magnetic field strengths for whole body imaging range from 0.5 T to 4.7 T. Some of the higher strength units have multinuclear capabilities (i.e. MR spectroscopy and imaging of elements other

than hydrogen can be performed). All superconducting magnets have their fields directed along the bore of the magnet and parallel to the long axis of the subject, as illustrated in Figure 13. The directions of the x and y axes are arbitrarily assigned. In medical terminology, slices directed along the z axis are transverse cuts, slices directed along the x axis are sagittal cuts and slices directed along the y axis are coronal cuts.

The magnetic field gradients are generated by current-carrying coils (gradient coils) that lie inside the magnet and produce a magnetic field with linear spatial variation as illustrated in Figure 14. The coils are oriented parallel to each other with currents flowing in opposite directions. The gradient fields can be aligned parallel or perpendicular to the static field B_o. The field gradients are constantly being turned on and off and may have different magnitudes throughout the pulse sequence. Typical values for gradients are on the order of 0.1 to 1 gauss/cm. Although the gradients are directed along the three principal axes, it is possible to obtain images along any oblique axis by suitable combinations of the gradients.[43]

Radiofrequency (RF) coils are used to excite the nuclei as well as receive their resulting signal. The two classes of coils in MRI are whole-volume coils, which excite and receive signal from a large sample of tissue, and local (surface) coils, which cover only a small region of tissue but with a much higher S/N ratio. The two most commonly used configurations for RF coils have been solenoidal and saddle-shaped, as illustrated in Figure 15. The solenoidal type (Figure 15a) has the static field perpendicular to the long axis of the coil and the saddle coil (Figure 15b) has the static field parallel to its long axis.

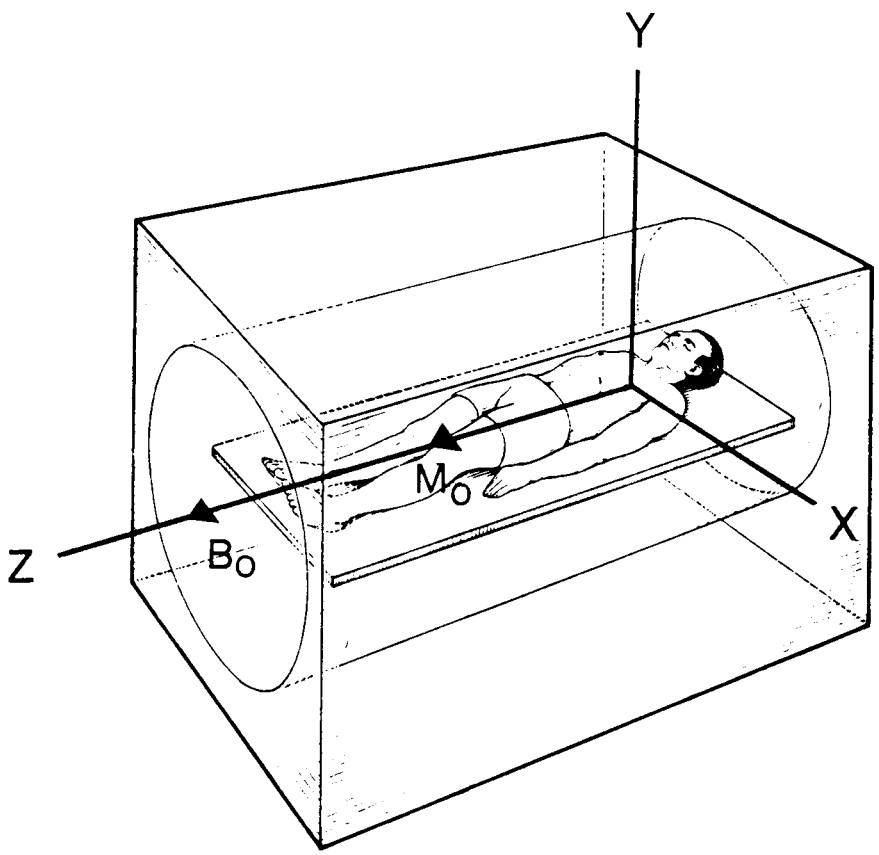

Figure 13. Orientation of x, y and z axis in a whole-body superconducting magnet.

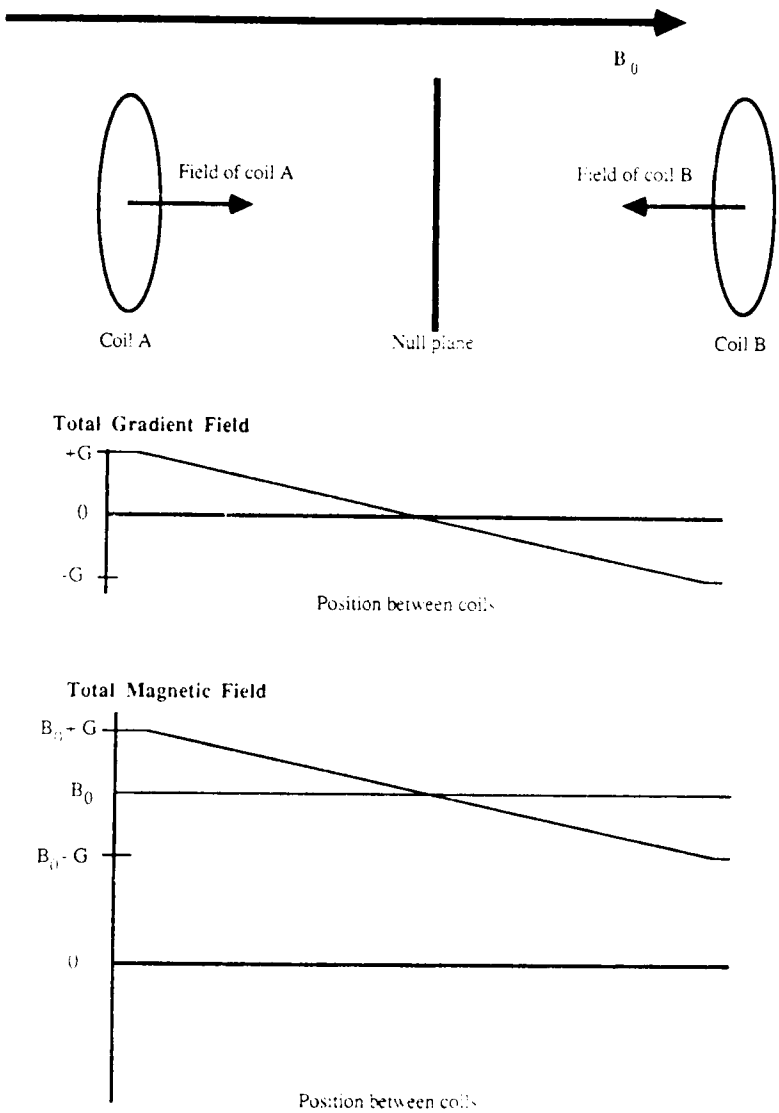

Figure 14. Production of a magnetic field gradient with the use of gradient coils.

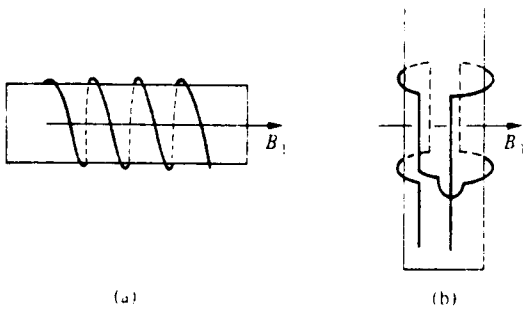

Figure 15. Most common radiofrequency coil designs.

Most of the other equipment used in whole body imaging units is quite similar to that used in conventional NMR spectrometers although the power requirements are substantially greater. Computer systems must handle large arrays of data so array processors and large disk systems are mandatory. Operator consoles usually have two screens, one for entering and displaying information and one for displaying images. The total cost for whole body imaging installation currently runs between $1 and $2.5 million.

PART I: THE DEVELOPMENT AND EVALUATION OF SEVERAL Gd-DTPA DERIVATIVES FOR USE AS MRI CONTRAST ENHANCEMENT AGENTS

CHAPTER II

INTRODUCTION TO MRI CONTRAST ENHANCEMENT AGENTS

A. INTRODUCTION

Early in the development of MRI there appeared to be little need for externally administered contrast agents because of the excellent soft tissue contrast. However, it later became apparent that the T_1 and T_2 parameters of different tissues often overlap, which results in poor contrast. For example, organs of the viscera, an area of interest in most imaging modalities, are all very similar in proton concentration. Unlike the brain and spinal cord in which there is considerable difference between proton density and relaxation times of the gray and white matter and cerebrospinal fluid, the tissues of the liver and spleen are quite uniform. This, in conjunction with the relative anatomical positioning of the organs of the viscera, makes tissue differentiation difficult. In addition, considerable intensity overlap between normal and pathologic tissue in a single organ can occur. Consequently intense interest has recently arisen in the development of pharmaceutical agents that will alleviate these problems.[44,45]

Contrast enhancement agents for MRI have been developed that alter the intrinsic parameters for imaging, namely the spin-lattice and spin-spin relaxation rates and, to a lesser extent, the proton density. There have been attempts to alter proton density by administration of exogenous agents (lipid solutions, olive oil, diuretics, ethanol) but no significant change in signal intensities can be induced by

such agents at safe dosages. Therefore, attention has focused on the utilization of paramagnetic species for contrast enhancement. Paramagnetic materials can markedly increase tissue relaxation with a resultant decrease in T_1 values causing an increased signal intensity and improved visual contrast in the T_1 weighted spin echo images most often used in clinical settings.[46] The theoretical basis behind relaxation enhancement and the various agents which have been developed to achieve this purpose are discussed in the following sections.

B. BACKGROUND

1. Magnetic Susceptibility and Relaxation Effects

Pharmacologic relaxation enhancement is based on positive magnetic susceptibility.[47] If a substance is placed in a magnetic field, induced magnetization in the substance is additive to that of the applied field. The ratio of induced magnetization to that of the applied field is termed the magnetic susceptibility of the substance, a measure of the extent to which the substance is susceptible to magnetization by an external field. Paramagnetic species are characterized by the predominant magnetic effects of unpaired electron spins because an unpaired electron has a magnetic moment approximately three orders of magnitude greater than that of a proton. Paramagnetic materials have positive susceptibilities and, therefore, positive induced magnetization; this induction reinforces the applied field and the density of lines of magnetic flux is increased, as illustrated in Figure 16.

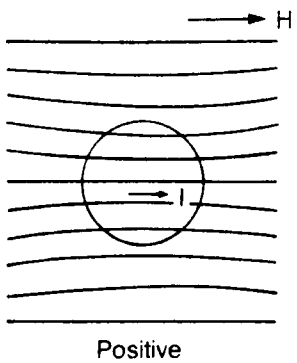

Figure 16. Principle of positive magnetic susceptibility.

Paramagnetic enhancement of nuclear relaxation was first reported in 1946 by Bloch and co-workers when they demonstrated that paramagnetic ions drastically reduced the spin-lattice relaxation times of the protons in water.[48] Positive susceptibility is necessary but not sufficient for effective relaxation enhancement. The magnitude of relaxation enhancement depends also on the proximity of the nuclear and electronic spins and on the correlation time of their interaction. This can be conceptualized as an interaction between the magnetic moment of a nucleus (proton for example) and the greater magnetic moment of a paramagnetic molecule in which the tumbling and flipping electron spin creates randomly fluctuating magnetic fields at nearby nuclei. These changing fields have frequency components that match the nuclear precessional frequency and result in stimulated transitions between spin states (equivalent to an RF pulse), thereby realigning bulk magnetization and shortening T_1. The net effect on T_1 relaxation involves many individual interactions between electrons and protons. Theoretical rules governing each individual electron-proton interaction have been thoroughly defined.[49] Similarly, the greater magnetic moment of the paramagnetic species creates more

widely varying local magnetic fields that augment loss of coherence (equivalent to increasing field nonuniformity), thereby shortening T_2.

The relationship between T_1 and the magnetic moment of a paramagnetic molecule is defined by the following equation,

$$1/T_1 = 12\pi^2\gamma^2\eta N_p\mu^2_{eff}/5kT \qquad (11)$$

where η is the viscosity of the solution, N_p is the concentration of the paramagnetic molecules, μ^2_{eff} is the effective mean square magnetic moment of the paramagnetic species, k is the Boltzman constant and T is temperature. This relationship is very important in the design of MRI contrast enhancement agents. In particular, the T_1 relaxation rate is inversely proportional to the square of the magnetic moment of the paramagnetic species and its concentration. Hence, the relaxation enhancement can be increased by increasing the concentration of the species or by utilizing a species with a larger magnetic moment. However, there is a maximum concentration that can be utilized for this purpose. Although a decrease in T_1 results in an increase in signal intensity, a decrease in T_2 produces the opposite effect. A very short T_2 produces such a rapid decay in the FID that it becomes unobservable. As a consequence, an optimal concentration of any agent exists which produces the maximal change in signal intensity and thus the maximal contrast. For optimal relaxation enhancement, molecules bearing nuclear spins should have access to as many sites of the paramagnetic material as possible and be able to move in very close minimizing distance effects. Due to its small size, the water molecule is a prime candidate for relaxation enhancement.

The nature of the electron-proton interactions is not a static process but depends upon the motion of the paramagnetic agent, i.e. variations in the orientation of the agent's magnetic moment. The interaction time of the nuclear and electronic spins is dominated by the fastest rate of paramagnetic tumbling motion (correlation time). It has been shown that as τ_c approaches the Larmor frequency, the frequency of fluctuating magnetic fields will most affect the relaxation rate.[49] Therefore, a possible approach to altering relaxation rates is to alter correlation times. Due to more optimal correlation of spin motions, nuclear T_1 relaxation in biological systems is more effective with relaxation agents of large molecular weight or asymmetric shape, i.e. relatively long rotational correlation times. For example, Reuben found that complexing paramagnetic ions to serum albumin enhances the relaxation rate of water relative to the relaxation rate in the presence of free paramagnetic ions as a result of the increase in correlation time of the enhancement agent.[50] Relaxation enhancement is also more effective with paramagnetic species that have long electron spin relaxation times. Electron spin relaxation can dominate the dipole-dipole correlation time of interacting spins if it is faster than paramagnetic tumbling motion. This can limit the improvement in relaxation effects produced by increasing molecular size. Maximum contrast enhancement due to paramagnetic species occurs on T1 weighted images.[51]

2. Various Paramagnetic Contrast Agents

A useful pharmaceutical contrast agent should be: 1) chemically stable and easily stored in a form suitable for clinical administration; 2) readily available and inexpensive; 3) well tolerated in diagnostic doses and free from adverse physiological

effects; 4) rapidly excreted; 5) chemically versatile so it can be modified to permit selective tissue targeting if necessary; and 6) highly paramagnetic, thereby altering tissue contrast at relatively low doses. With these criteria as a guide, the following paramagnetic species have been investigated for the use as contrast agents in MRI:

Metallic Ions
Transition metals series
Cr^{+3}
Mn^{+2}
Fe^{+2}, Fe^{+3}
Co^{+2}, Co^{+3}
Ni^{+2}
Cu^{+2}
Lanthanide series
Eu^{+2}
Gd^{+3}

Nitroxide stable free radicals

Molecular oxygen (O_2)

Molecular oxygen has two unpaired electrons and it's inhalation is a simple approach to altering the T_1 of blood. Molecular oxygen has been used in volunteers giving positive results but the decrease in relaxation time has been small.[52] It may be possible to use contrast enhanced images produced by O_2 inhalation as a means to monitor metabolic processes. However, oxygen is rapidly metabolized in-vivo resulting in a rapid loss of paramagnetic properties.[53]

Nitroxide stable free radicals (NSFR) are paramagnetic species having one unpaired electron localized in a nitrogen-oxygen bond. They have been developed and used as paramagnetic probes in biological studies for over 20 years.[54] These paramagnetic compounds are secondary amine N-oxides that generally have no

hydrogen atoms on the carbons adjacent to the nitroxide nitrogen. Incorporation of methyl groups at the alpha carbons renders the nitroxide stable toward disproportionation, a major decomposition pathway of radical centers. The two major classes of nitroxides tested for MRI are the five-membered ring pyrolidine nitroxides, 1, and the six-membered ring piperidine nitroxides, 2. These nitroxides may have additional functional groups (R) to alter solubility properties and provide a method for chemical modification.

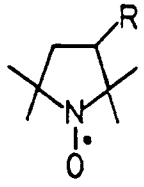

1

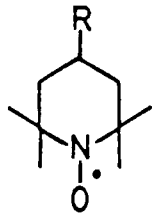

2

Nitroxides have prolonged stability at varying pH and temperature, reasonable availability and shelf life, chemical versatility for conjugation to biomolecules, long electron spin relaxation times and relatively low toxicity. Structure-relaxivity studies have shown that proton relaxation enhancement increases with increased nitroxide molecular weight, with piperidine nitroxides relative to pyrolidine nitroxides and with compounds containing two nitroxides per molecule.[55] Macromolecular derivatives such as protein and fatty acid-protein conjugates have been prepared and show up to ten-fold improved relaxivity. Experimentally, nitroxides have been used for contrast enhancement of the kidney, myocardium and central nervous system.[56-59] Nitroxide compounds have shown to be susceptible to reduction in-vivo, thus limiting

their use as MRI contrast agents.[60,61] The resulting N-hydroxylamine compounds are diamagnetic and no longer contribute to proton relaxation enhancement. To date, nitroxides have not been used clinically.[62]

The most important class of paramagnetic species used as MRI contrast agents are metal ions of the transition and lanthanide series. First row transition metal ions contain partially filled 3d electron orbitals. By virtue of Hund's rule (maximal spin angular momentum), the five degenerate 3d orbitals are filled such that each orbital must contain one unpaired electron before two electrons (spin paired) can occupy the same orbital. Since the magnitude of T_1 relaxation enhancement is partially dependent on the magnetic moment of the paramagnetic species, the metal ions most favored are Mn^{+2}, Cr^{+3} and Fe^{+3}, which have 5, 3 and 5 unpaired electrons, as illustrated in Table 1. At concentrations of 10^{-5} to 10^{-1} M, these metal ions have shown to reduce significantly proton T_1 relaxation values in-vitro.[63,64] For example, a 10 mM solution of $Fe(NO_3)_3$ reduces T_1 values from 3 sec to 10 msec. The metal ions of the lanthanide series have partially filled 4f electron orbitals. Proton T_1 relaxation measurements of several lanthanide ions (Gd^{+3}, Dy^{+3}, Ho^{+3} and Eu^{+3}) have shown Gd^{+3} to be the most effective at enhancing relaxation due to it's large magnetic moment (seven unpaired electrons) and long electron relaxation time, as illustrated in Tables 1 and 2.[65] The other lanthanides have very short electron spin relaxation times and are therefore poor spin relaxing agents.

A number of investigators in MRI have employed soluble free metal ions as contrast media.[66-70] Solutions of $MnCl_2$ and $GdCl_3$ have been found to decrease the T_1 of the liver, heart and kidney. $FeCl_3$ solutions have provided enhancement

Table 1: Outer Shell Electron Configuration and Magnetic Moment for Selected Paramagnetic Ions

Paramagnetic ion	Outer orbital electron distribution	Magnetic moment (Bohr magnetrons)
Cr^{+3}	$3d^3$	3.8
Mn^{+2}, Fe^{+3}	$3d^5$	5.9
Fe^{+2}	$3d^6$	5.1-5.5
Co^{+3}	$3d^6$	5.4
Co^{+2}	$3d^7$	4.1-5.2
Ni^{+2}	$3d^8$	2.8-4.0
Cu^{+2}	$3d^9$	1.7-2.2
Eu^{+2}	$4f^7$	7.9
Gd^{+3}	$4f^7$	7.9

Table 2: Electron spin relaxation times

Class	Ion	Electron relaxation time
Transition metals	Mn^{+2}	10^{-8} to 10^{-9}
	Cr^{+3}	10^{-9} to 10^{-10}
	Fe^{+3} (high spin)	10^{-9} to 10^{-10}
	Mn^{+3}	10^{-10} to 10^{-11}
	Fe^{+2} (high spin)	10^{-10} to 10^{-11}
	Cr^{+2}	10^{-11} to 10^{-12}
	Fe^{+3} (low spin)	10^{-11} to 10^{-12}
Lanthanide metals	Gd^{+3}	10^{-8} to 10^{-9}
	Eu^{+2}	10^{-12} to 10^{-13}
	Dy^{+3}	10^{-12} to 10^{-13}
	Ho^{+3}	10^{-12} to 10^{-13}
Nitroxides		10^{-7} to 10^{-8}

of the gastrointestinal tract. However, free metal ions remain too toxic to be considered as safe MRI contrast agents for human use.[71] Metal ions are typically metabolized by the liver and display slow biological clearance. In addition, subtoxic doses of metal ions often have adverse effects as well.[68,72] The toxicity can be lowered by rendering the ions insoluble.[73-76] For example, colloidal manganese sulfide has decreased the T_1 of the liver and lung in rats with decreased toxicity relative to free Mn^{+2} ions.[73] Insoluble forms of gadolinium were shown to be phagocytized by the reticuloendothelial system and produced contrast enhancement of the liver and spleen with reduced toxicity relative to free Gd^{+3} ions.[75,76] A potential problem with all these insoluble agents, however, is long-term retention by the reticuloendothelial system.

Chelating metal ions with organic ligands greatly reduces their toxicity. A major concern for the intravenous use of metal chelates as MRI contrast agents is the potential for in-vivo dissociation of the complexes to afford toxic free metal ions. Hence the preparation of metal complexes having high stability constants is essential. Stabilities of metal chelate complexes vary greatly and depend on the choice of both metal and chelating ligand.[77] To date, the polyaminocarboxylate ligands, ethylenediaminetetraacetic acid (EDTA), 3, and diethylenetriaminepentaacetic acid (DTPA), 4, have received the most attention due to their relatively high affinity for most metal ions. EDTA and DTPA, having six and eight chelating sites respectively, form strong water-soluble complexes which demonstrate remarkable in-vitro and in-vivo stability.

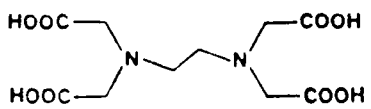

3

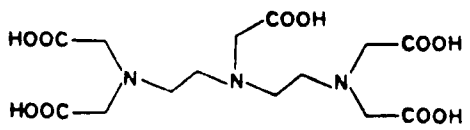

4

To assess metal complex efficiency for proton relaxation enhancement, in-vitro T_1 relaxation measurements have been determined for Cr-EDTA, Fe(II)-EDTA, Gd-EDTA, Mn-DTPA and Gd-DTPA.[78] The relaxation enhancement of these complexes varied according to the metal ion, the concentration and the ligand. The metal complexes were less effective at reducing T_1 than the corresponding free ions, but the loss in efficacy was smaller than one order of magnitude. The reduction in T_1 relaxation enhancement observed with the metal complexes, relative to free ions, is a direct result of chelation which reduces the number of coordination (hydration) sites through which the metal interacts with the tissue water.[79] Increased enhancement has been observed when the correlation time is slowed by macromolecular complexation of the aminocarboxylate complexes with albumin, immunoglobulins or polymers.[80,81]

In-vivo studies have shown that intravenously injected metal-polyaminocarboxylate complexes provide MRI contrast enhancement of various tissues.[82] The most promising metal complex to date is gadolinium-diethylenetriaminepentaacetic acid (Gd-DTPA), 5, which has been extensively investigated because of it's low toxicity and highly effective relaxation enhancement

properties.[83,84] Of all the paramagnetic elements tested, gadolinium was found to exert the strongest effect on the relaxation time of the protons in water.[85] Gd-DTPA has a formation constant of 10^{23} in a pH range of 3-10, resulting in a high degree of in-vivo stability.[86] This is almost six orders of magnitude greater than that for Gd-EDTA. Gadolinium has a coordination number of 8 or greater, in contrast to 6 for most transition metals; therefore it's chelation with DTPA leaves at least one site open for rapid exchange with water molecules.

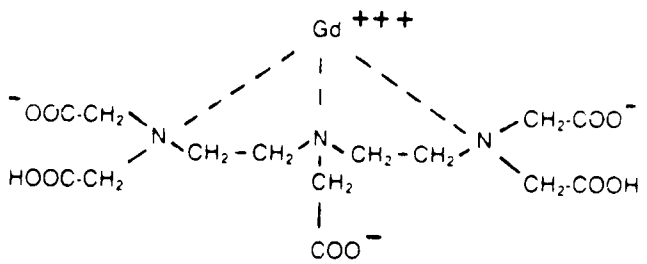

5

The basic pharmacology of Gd-DTPA has been extensively studied by Weinnman.[87] Following intravenous injection, the complex is distributed in the vascular and extracellular spaces thus producing relaxation enhancement in tissues having high interstitial fluid content. It is then concentrated within the kidney and excreted unchanged within the urine ($t_{1/2} \approx 20$ min). Gd-DTPA does not cross the normal blood-brain barrier but it is present in higher concentration in gray matter as compared to white matter, reflecting the different vascularity of these tissues. However, when there is a focal disruption of the blood-brain barrier which occurs in a variety of pathologic conditions including tumors and infections, the blood-brain

barrier becomes permeable and Gd-DTPA accumulates in an extravascular location. For this reason, the most common application of Gd-DTPA is in imaging tumors of the brain.[88-90] It has also provided contrast enhancement for disorders associated with the spinal cord, heart and kidney.[91-93] Gd-DTPA is currently being used clinically in Europe and the USA. Typically, dosages of 0.1-0.2 mmol/kg are used.

3. Targeting of MRI Contrast Agents

A number of research groups are attempting to develop tissue and organ specific paramagnetic contrast agents. Several different approaches are being studied which utilize methodology presently employed in other pharmaceutical fields. One current approach involves the development of paramagnetic immunoimaging agents; a variety of monoclonal antibodies are now available which are used to prepare tissue-specific paramagnetic agents. Recent advances in the development of bifunctional chelate compounds have made it possible to derivitize proteins with chelating agents which can subsequently bind metal ions.[94-96] The resulting paramagnetic immunoimaging agents have successfully demonstrated selective in-vivo contrast enhancement in animals.[97,98]

Porphyrins are also capable of chelating various transition metals. Imaging studies utilizing metalloporphyrins have produced in-vivo contrast enhancement; the manganese complex of protoporphyrin has produced enhanced relaxation of liver tissue.[99] Porphyrins tend to accumulate in tumor tissues providing a method for their contrast enhancement.[100]

A unique method which has potential for specific tissue targeting of paramagnetic contrast agents employs the use of the liposome. Liposomes are man-

made lipid vesicles consisting of single or multiple lipid lamellae and one or several aqueous compartments. The liposomal lamellae are composed of phospholipid bilayers similar to the structure of a cell membrane. Phospholipids are amphipathic compounds consisting of nonpolar hydrocarbon tails and polar ionic head groups.

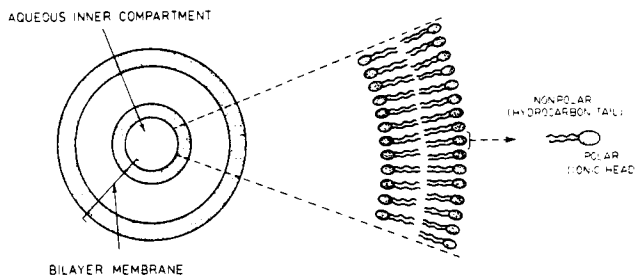

Since the introduction of the liposome concept by Bangham[101] as a model system to study cell membrane transport, the use of liposomes as a medium for the delivery of pharmaceutical agents has been extensively studied. Liposome distribution can be controlled by their size, lamellae composition and surface characteristics (polarity, charge, etc.). Liposomes are rapidly removed from the blood by either the reticuloendothelial system or hepatocytes resulting in accumulation in normal liver tissue.[102,103] Uptake occurs by either phagocytosis of large liposomes or direct uptake of small liposomes by hepatocytes. For this reason, liposomes have been utilized for the transmission of chemotherapeutic and antibiotic agents to the liver and spleen for the treatment of malignant and infectous diseases.[104,105] These agents can be incorporated in the liposome by one of two different methods; water-soluble agents can be entrapped in the central aqueous compartment or lipid-soluble agents can be held in the bilayer membrane by van der

Waals interactions.[106,107] Recently, liposomes have been utilized as a means to deliver several MRI contrast agents to selective sites in which the paramagnetic species were encapsulated in the liposomal aqueous core.[108-111] For example, Mn-DTPA was entrapped in multilamellar vesicles (MLV) smaller than 1.2 microns resulting in selective accumulation in the liver and spleen and significant relaxation enhancement of the two organs (31% and 62%, respectively).[108]

4. A Gadolinium-Labeled Liposome for Contrast Enhancement

The diagnostic value of MR imaging of the liver and spleen has not equaled that achieved in MR imaging of the central nervous system.[112,113] Although Gd-DTPA is an ideal agent for contrast enhancement of the brain and spine, it is of little value for imaging of the liver and spleen since the highly soluble complex does not accumulate in these organs.[114,115] Recently Kabalka and coworkers reported the development of a liposomal Gd-DTPA derivative in an effort to extend its utility for MR imaging of the liver and spleen.[116,117]

The new Gd-DTPA derivative was prepared by first incorporating gadolinium into a DTPA derivative containing lipophilic alkyl side chains. The DTPA derivative was prepared via the previously published procedure of Hnatowich.[118] A slight excess of the cyclic dianhydride of DTPA, 6, prepared by the method of Eckelman,[119] was allowed to react with stearylamine to give the stearylamide derivative of DTPA (DTPA-SA), 7, as illustrated in equation 12. From the results of elemental analysis, it was concluded that the stearylamide derivative exists as the stearylammonium salt.

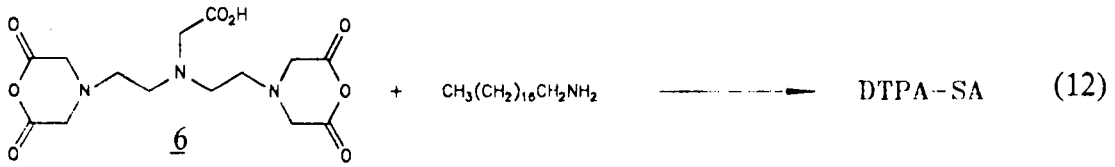

6

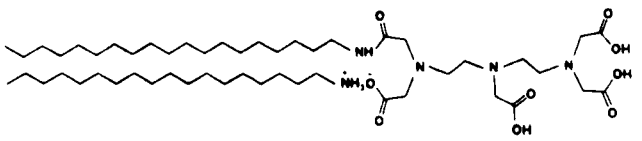

7

Incorporation of the paramagnetic species was performed by the reaction of DTPA-SA with $GdCl_3$ to give the gadolinium complex of the stearylamide derivative (Gd-DTPA-SA) 8. It was postulated that the attachment of two hydrophobic chains to DTPA should have little effect on it's ability to complex the Gd^{+3} ion; the formation constant presumably lies midway between that for Gd-DTPA and Gd-EDTA. Although little was known about the actual coordination number of the gadolinium in the complex, it was assumed that there were at least two available sites for rapid exchange with H_20 molecules. The Gd-DTPA-SA complex is a phospholipid analogue containing nonpolar hydrocarbon tails and a polar ionic head.

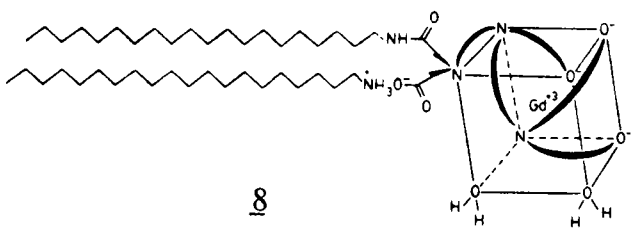

8

The resulting paramagnetic amphiphiles were utilized to construct a new class of gadolinium-labeled liposomes (GLL). The GLL agents were unique in that the paramagnetic amphiphile was incorporated into the lamellar membrane making it an integral part of the liposome. This contrasts with the more traditional approach in which the paramagnetic agents are simply encapsulated in the aqueous liposomal core. Following injection, these liposomes are weakened in the presence of serum albumin and lipoproteins resulting in leakage of the entrapped agent into the blood pool prior to delivery to the target site followed by rapid kidney excretion.[110,111] In addition, entrapment within the aqueous compartment of the liposome isolates the paramagnetic species from the surrounding tissue water.

The paramagnetic liposomes were prepared by mixing an appropriate amount of Gd-DTPA-SA, egg phosphatidylcholine and cholesterol.[120] In-vitro experiments performed on excised mouse liver tissue revealed that maximum T_1 relaxation enhancement was achieved when the ratio of the three lamellar constituents was 1:1:1 (33.3 mol% Gd-DTPA-SA), as illustrated in Figure 17. Formulations using more than 33.3 mol% Gd-DTPA-SA exhibited a tendency to aggregate, making them less effective. The T_1 relaxation rates were determined by the method of inversion recovery.[6,7] The resulting GLL agents containing 33.3 mol% of the paramagnetic amphiphile were small unilamellar vesicles (SUV) with an average diameter of 0.05 μm.

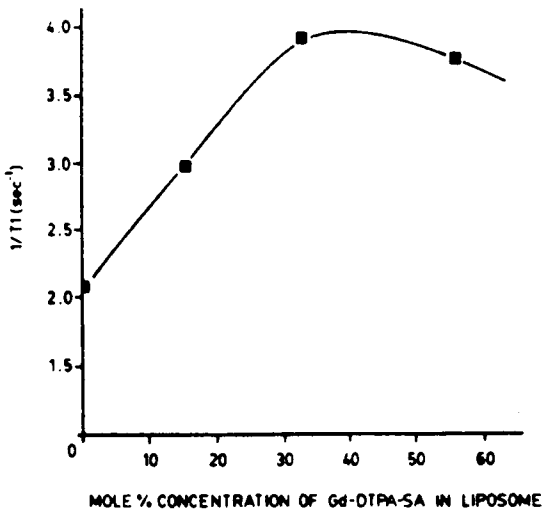

Figure 17. Effect of Gd-DTPA-SA on the T_1 of mouse liver.

The 33.3 mol% GLL was used to carry out a dose-response study on mice to determine the relaxation rates of various tissues with increasing amounts of lipid dose. The results showed that the T_1 relaxation rates decreased as the dose of the GLL increased as illustrated in Figure 18. For example, T_1 relaxation of the liver and spleen was enhanced by 110% and 66%, respectively, when 9 μmol of lipid was injected. This dose corresponds to a gadolinium concentration of 0.15 mmol/kg which is within the dose range used in current Gd-DTPA studies of the central nervous system in humans. Injection of liposomes at this level produced no apparent short- or long-term toxicity but toxicological assays have not been carried out. The leveling of the dose effect at 14 μmol of lipid was attributed to the saturation of the tissues with the liposomes.[97]

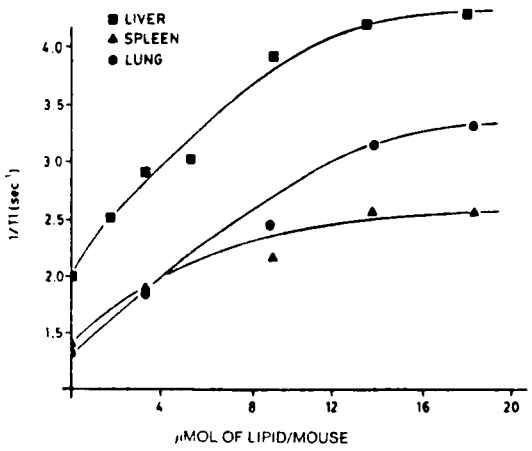

Figure 18. Dose-response study utilizing 33.3 mol% GLL.

A tracer study utilizing ^{153}Gd-DTPA-SA in the liposome preparation was performed to determine the biodistribution of the GLL agent. The results demonstrated that the agent was rapidly cleared from the blood and accumulated in the liver and spleen as illustrated in Figure 19. The material was retained in the liver and spleen for a period exceeding 11 days indicating remarkable in-vivo stability of both the liposomes and the Gd-DTPA-SA complex. This enhanced stability was supported by similar results in other experiments.[121] The results of the dose-response and biodistribution studies indicated that the gadolinium-labeled liposomes have the potential for use as selective MRI contrast enhancement agents for imaging of the liver and spleen.

C. STATEMENT OF THE PROBLEM

The GLL agent containing 33.3 mol% of the Gd-DTPA-SA complex developed by Kabalka and coworkers effectively enhances the T_1 relaxation of mouse

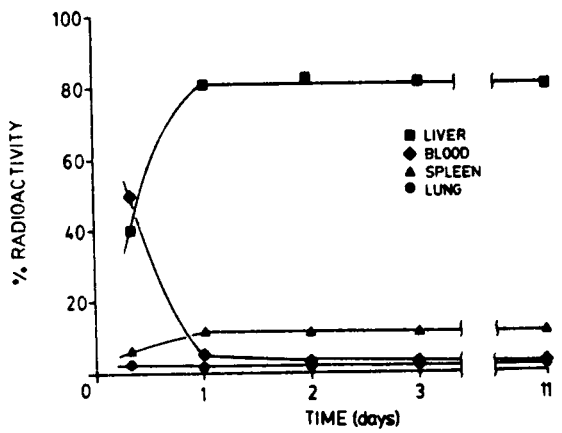

Figure 19. Biodistribution of ^{153}GLL in Balb/c mice.

liver and spleen tissue but it exhibited a very long retention time in those organs. In fact, one month after intravenous injection, 95% of the administered dose remained in-vivo with 81% residing in the liver.[121] The ideal MRI contrast enhancement agent would remain in the target tissue only long enough to perform the imaging studies and would be followed by rapid elimination from the human body.

The objectives of the research project presented in Part I were: 1) to develop new Gd-DTPA derivatives to be utilized as GLL agents which would retain the relaxation enhancement properties of the Gd-DTPA-SA complex but exhibit a shorter biological lifetime and 2) to evaluate the various GLL agents as MRI contrast enhancement agents for the liver and spleen. The development of new GLL agents utilized two approaches: first, the existing Gd-DTPA amide complex was modified by decreasing the length of the nonpolar alkyl chains in an effort to decrease the in-vivo stability of the resulting liposomes and, second, new Gd-DTPA derivatives were developed that would degrade more rapidly to lipid and Gd-DTPA residues resulting in rapid excretion of the paramagnetic species. The preparation, biological clearance rate and contrast enhancing ability of these new agents will be discussed.

CHAPTER III

RESULTS AND DISCUSSION

A. PREPARATION OF Gd-DTPA DERIVATIVES

1. Gd-DTPA Amide Derivatives

The first approach to the development of a GLL agent with a shorter in-vivo lifetime involved decreasing the length of the lipophilic tails. Since most phospholipids consist of hydrocarbon chains containing 16 carbons or more, [122] a decrease in the chain length could result in a decrease of the stability of the lamellar membrane resulting in a more rapid degradation of the liposome. Alternatively, an increase in the solubility of the Gd-DTPA amide complex in polar media due to the decrease in hydrophobicity might increase the metabolic rate of the paramagnetic agent, since higher polarity species are known to be more readily extracted from biological membranes by serum albumin than lower polarity species. Therefore, a series of Gd-DTPA amide derivatives were prepared in which the DTPA chelates contained hydrocarbon tails of decreasing chain length.

The various DTPA amide derivatives were prepared by the method employed by Hnatowich for the preparation of DTPA-SA.[118] DTPA dianhydride[119] was allowed to react with various amines using chloroform as the solvent to give the various DTPA amide derivatives, 9, as shown in equation 13. The amines utilized were cetyl amine (hexadecylamine), myristyl amine (tetradecylamine), lauryl amine (dodecylamine) and decylamine.

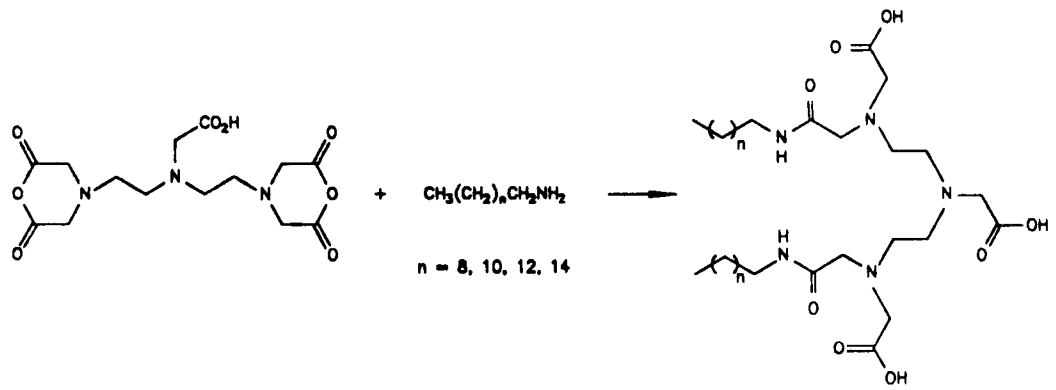

(13)

9

The resulting DTPA amide derivatives were characterized by elemental analysis, infrared (IR) spectroscopy and NMR spectroscopy (^{1}H and ^{13}C). The NMR data from the various DTPA amide ligands revealed that the species most likely exists as the diamide 9 rather than the ammonium salt previously reported.[119] Supporting evidence is obtained from the ^{13}C and ^{1}H spectra (Figures 20 and 21, respectively) of the DTPA decylamide derivative (DTPA-DA). For example, in the ^{13}C spectrum, three signals appear at 170-175 ppm in an approximate 2:2:1 ratio which correspond to the carbonyl carbons of the acid and amide functional groups. Although ^{13}C NMR is not a quantitative technique due to the nuclear Overhauser effect (NOE), the above ratio approximation is valid because none of the carbonyl carbons are directly bonded to hydrogen atoms. If the species existed as the previously reported ammonium salt, at least four or possibly five signals corresponding to carbonyl carbons would be expected. In addition, five signals appear at 53-60 ppm in an approximate 2:2:2:2:1 ratio corresponding to the five nonequivalent sets of isolated methylene carbons contained in the DTPA portion of the molecule. This is further evidence for the symmetrical diamide structure. Again

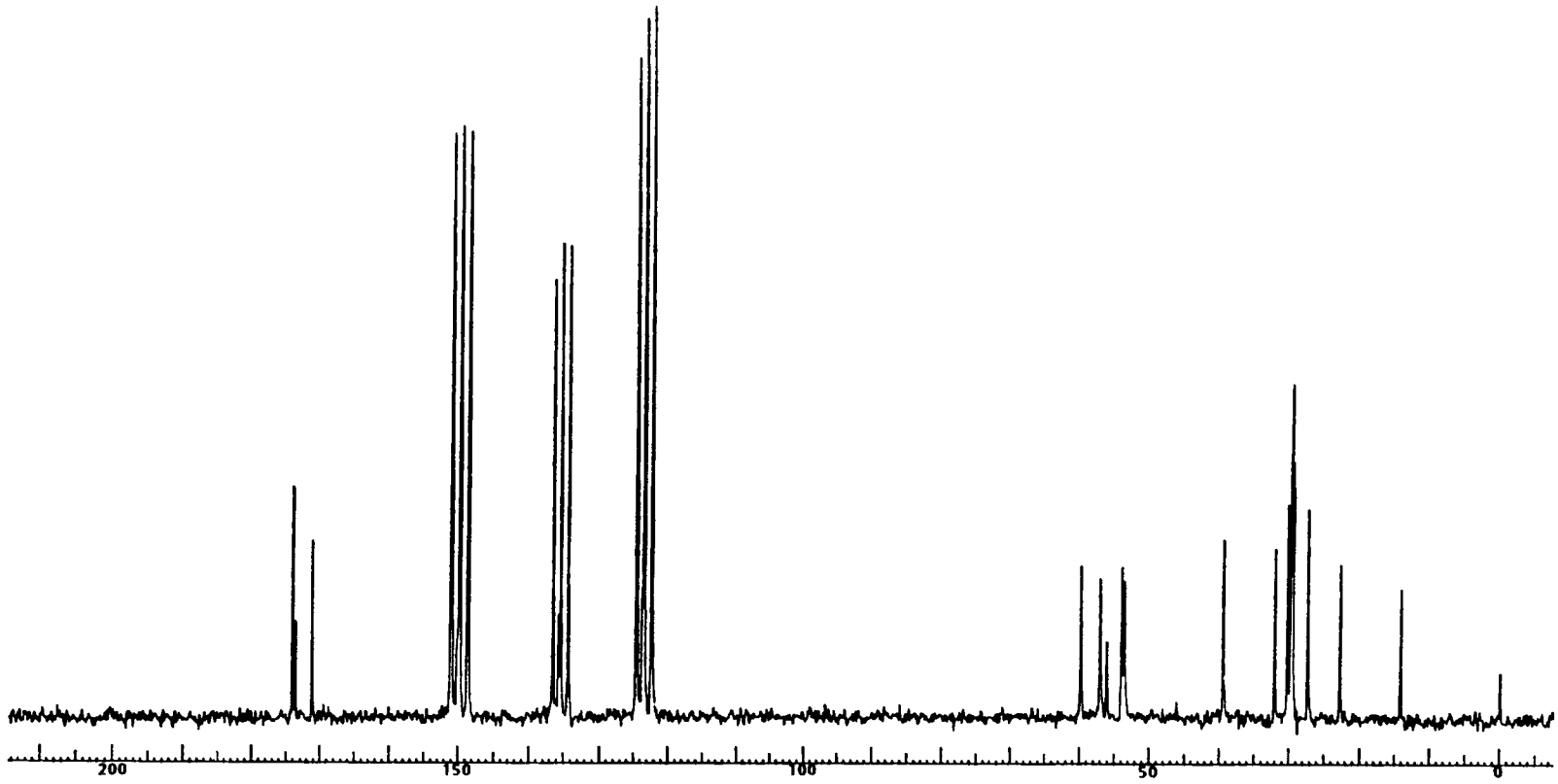

Figure 20. ^{13}C NMR spectrum of DTPA-DA in py-d_5.

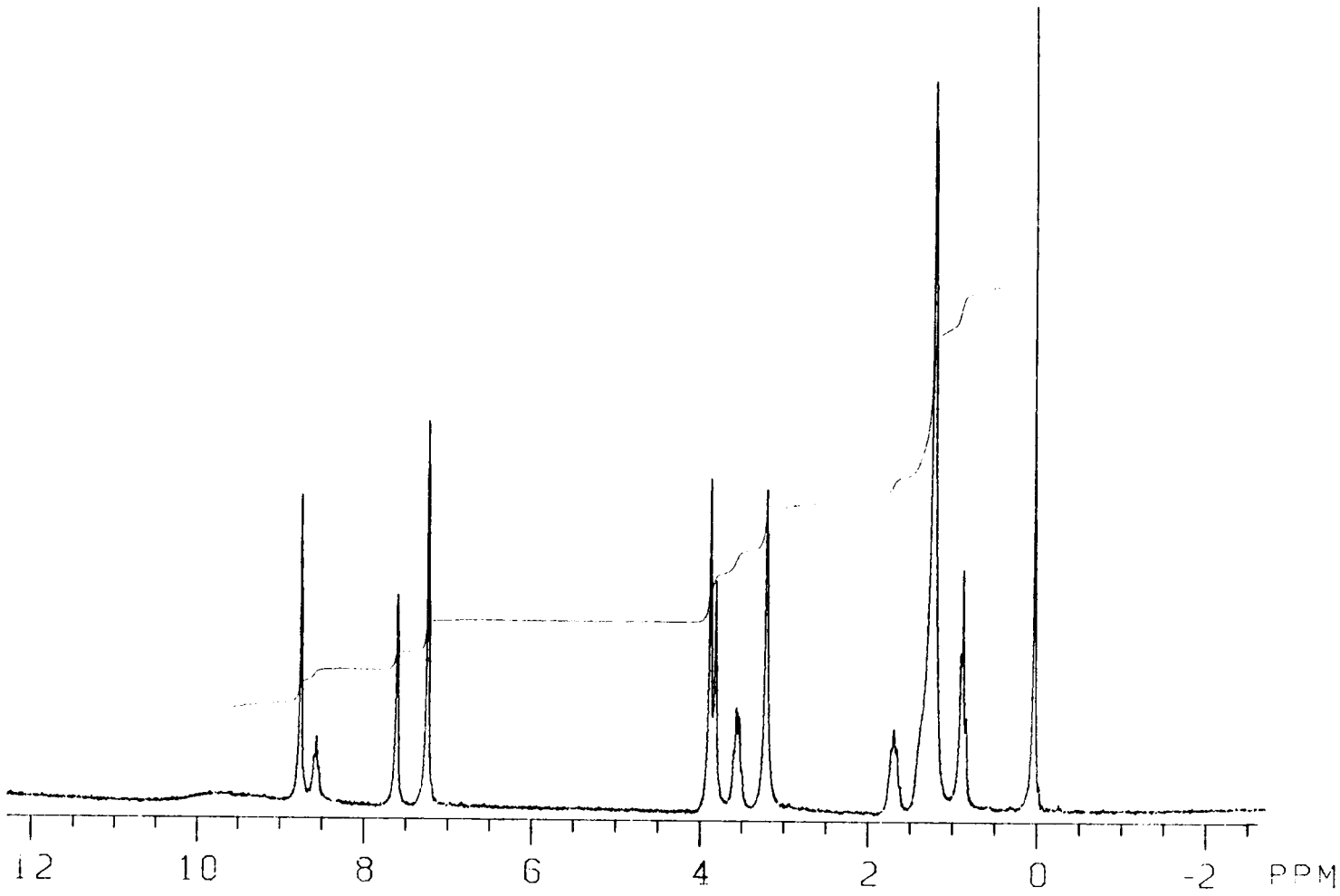

Figure 21. ^{1}H NMR spectrum of DTPA-DA in py-d_5.

the ratio approximation is valid since all the carbon atoms are directly bonded to the same number of hydrogen atoms. The proton spectrum (Figure 21) is also indicative of the DTPA diamide derivative; the integration reveals the presence of two amide protons (8.55 ppm). The IR data from the various diamides was in good agreement with the literature values reported for DTPA-SA.[119]

The various Gd-DTPA diamide complexes were prepared via the procedure employed for the preparation of Gd-DTPA-SA.[116] The appropriate DTPA diamide ligands were allowed to react with $GdCl_3$ in hot ethanol to give the resulting Gd-DTPA diamide complexes 10. The increased solubility of the complexes in polar media with decreasing alkyl chain length became evident in the work-up procedure, especially with the Gd-DTPA laurylamide (Gd-DTPA-LA) and Gd-DTPA decylamide (Gd-DTPA-DA) complexes. In the isolation of the longer chain amide complexes, the products precipitated from ethanol; however, the Gd-DTPA-LA (n=10) and Gd-DTPA-DA (n=8) complexes could not be precipitated even at very high concentrations, therefore, a different isolation procedure was developed which will be described later.

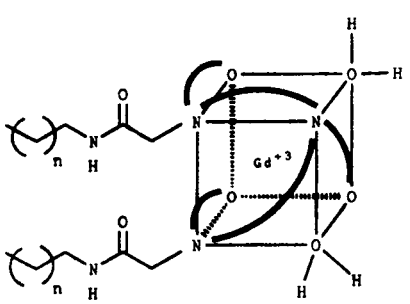

n = 8, 10, 12, 14

10

The various Gd-DTPA diamide complexes were characterized by melting point, elemental analysis and IR spectroscopy. ^{1}H and ^{13}C NMR spectroscopy could not be utilized for the characterization of the complexes due to the paramagnetic effect of the Gd^{+3} ion resulting in drastic line broadening and low sensitivity. A melting point (MP) determination was utilized as the initial test for complexation as indicated by a large increase in the melting point of the various complexes ($>300\,^{\circ}C$) as compared to the uncomplexed ligands. The elemental analysis revealed that the various complexes existed as the hydrated species, indicating available sites for coordination with H_2O molecules. The hydration number of the different complexes varied from 2 to 5. The variation in hydration numbers is probably due to the different drying conditions the various complexes were subjected to prior to analysis. The IR data from the various complexes are in good agreement with the values reported for Gd-DTPA-SA.[121] Gd-DTPA-DA, the shortest chain Gd-DTPA diamide complex, was used for the preparation of the GLL agents utilized in the biological studies.

2. A Gd-DTPA Ester Derivative

Another approach to develop a GLL agent with a shorter in-vivo lifetime involves replacing the amide linkage with a more reactive functional group. It was felt that the use of a more reactive linkage would result in a more facile degradation of the paramagnetic complex to lipid and Gd-DTPA residues by either hydrolysis or various enzymatic processes. As a result, the highly soluble Gd-DTPA complex would be rapidly excreted; hence, the new Gd-DTPA derivative would have a shorter biological lifetime than Gd-DTPA-SA. The most obvious choice of functional group

to achieve this purpose would be an ester linkage because they are easily synthesized and are more reactive toward nucleophiles than amides. For example, the hydrolysis of amides requires considerably more vigorous conditions than ester hydrolysis because the nitrogen substituent of the amide functionality imparts a very significant electron density to the carbonyl group resulting in decreased electrophilic character of the carbonyl carbon.[123] Therefore, a new Gd-DTPA derivative was developed in which gadolinium was incorporated into an amphiphilic ligand containing nonpolar hydrocarbon tails connected to the polar DTPA head via ester linkages.

Since ester linkages can easily be formed by the reaction of anhydrides with alcohols, this was the method employed for the preparation of the DTPA diester derivative, as illustrated in equation 14.[124] DTPA dianhydride was allowed to react with two equivalents of stearyl alcohol, prepared by the reduction of stearic acid with lithium aluminum hydride,[125] to give the distearylester derivative of DTPA (DTPA-SE), 11.

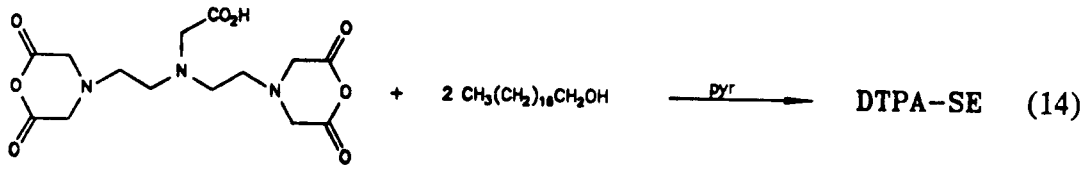

(14)

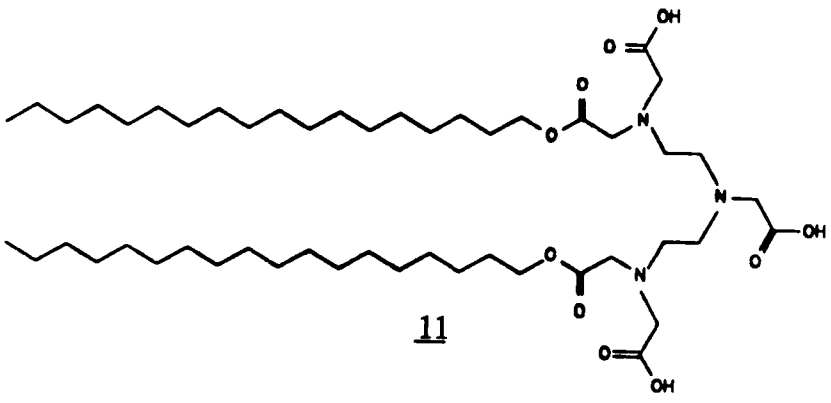

11

When the reaction was attempted initially using chloroform as the solvent, no reaction occurred. However, when using pyridine as the solvent, the desired ester product was formed. The alcoholysis of anhydrides has been known to be catalyzed by bases, such as pyridine.[126] This phenomenon, known as nucleophilic catalysis, is actually the result of two successive reaction processes. An example of this phenomenon is the pyridine catalyzed hydrolysis of acetic anhydride as illustrated in equation 15 and 16.[127]

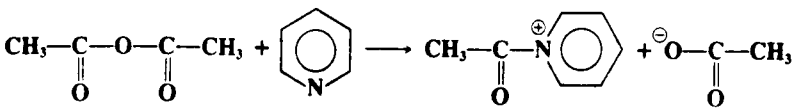

(15)

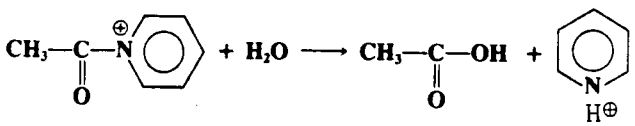

(16)

The resulting amphiphilic ligand, DTPA-SE, was characterized by elemental analysis, IR spectroscopy and NMR spectroscopy (^{1}H and ^{13}C). The elemental analysis revealed that the species exists as the diester derivative. In fact, attempts to obtain the monoester derivative by using an excess of the anhydride were unsuccessful. This same phenomenon was observed in the production of the DTPA amide derivatives. This result can be explained based upon kinetic factors; the monoanhydride resulting from attack of one equivalent of the nucleophile is much more reactive than the starting dianhydride. The ^{13}C and ^{1}H NMR spectra of DTPA-SE are presented in Figures 22 and 23, respectively. In the ^{13}C spectrum, two signals appear at 170-175 ppm corresponding to the carbonyl carbons of the acid and ester functionalities. The various signals at 53-57 ppm, corresponding to the

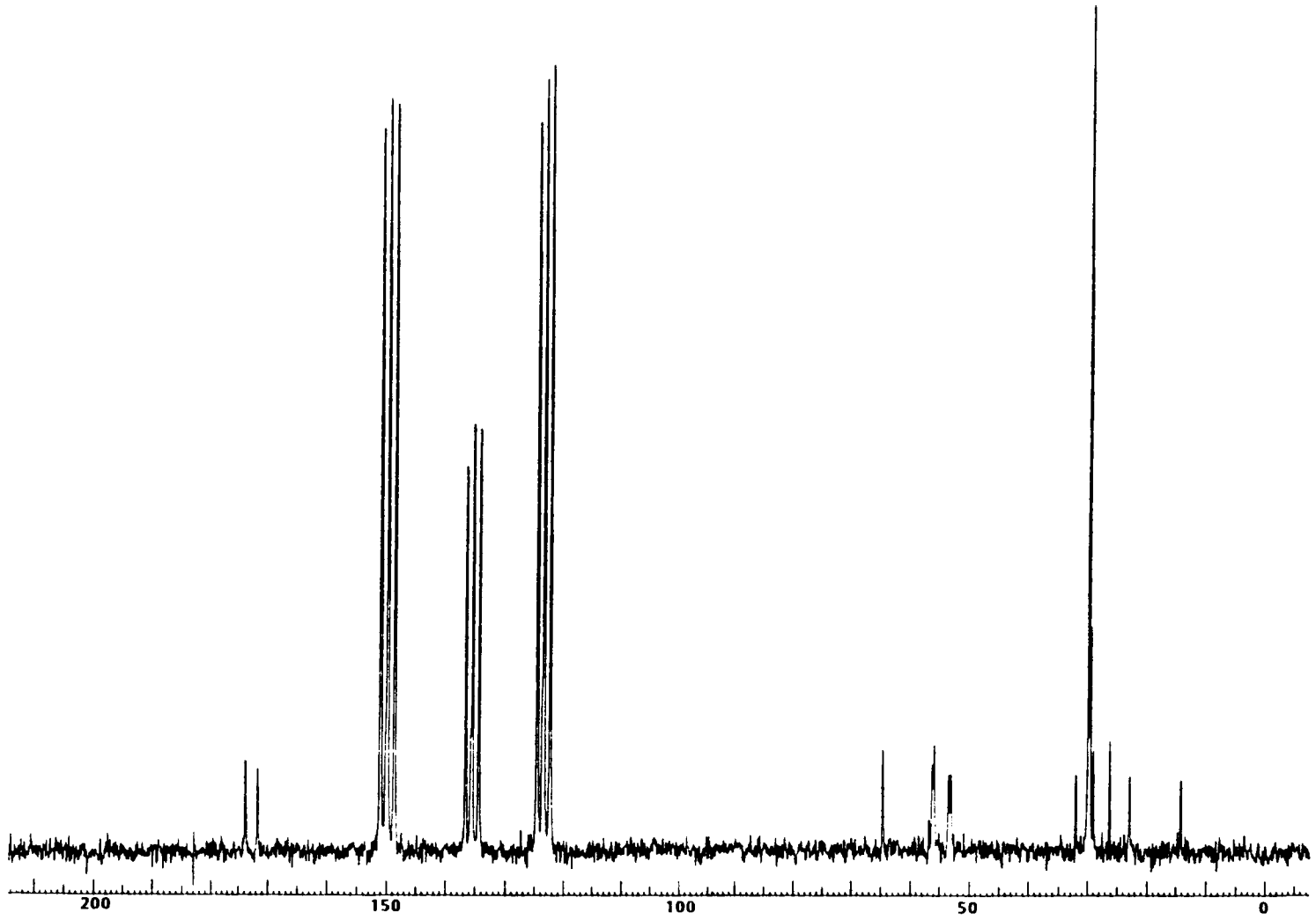

Figure 22. ^{13}C NMR spectrum of DTPA-SE in py-d_5.

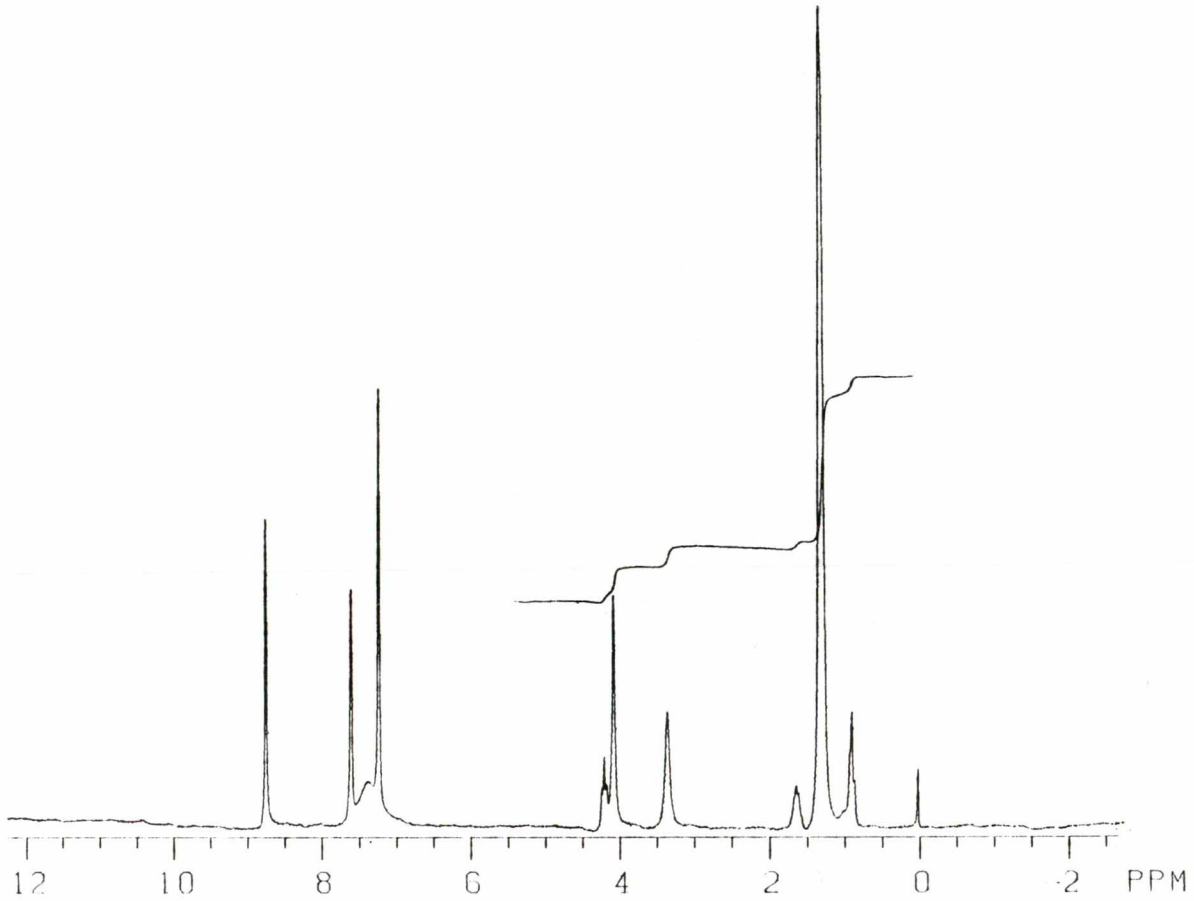

Figure 23. ^{1}H NMR spectrum of DTPA-SE in py-d_5.

nonequivalent isolated methylene carbons contained in the DTPA portion of the molecule, are not as resolved as they were in the ^{13}C spectrum of DTPA-DA (Figure 20). The integration and various chemical shift positions of the signals in the proton spectrum (Figure 23) are also indicative of the DTPA distearylester structure 11. The IR spectrum (refer to p 83) revealed the presence of the ester functional group.

The incorporation of gadolinium was achieved by the reaction of DTPA-SE with $GdCl_3$ to give the resulting Gd-DTPA distearylester complex (Gd-DTPA-SE), 12.[124] Due to the extreme solubility of DTPA-SE in pyridine, the latter was used as the solvent for the reaction. The complex was characterized by melting point, elemental analysis and IR spectroscopy. As expected, the MP of the complex (>300 °C) was substantially higher than that of the uncomplexed ligand (194-196 °C). Elemental analysis revealed that the species exists as the pentahydrate which would indicate a coordination number greater than the eight illustrated in structure 12. The Gd-DTPA-SE complex was incorporated into liposomes to be utilized in the biological studies.

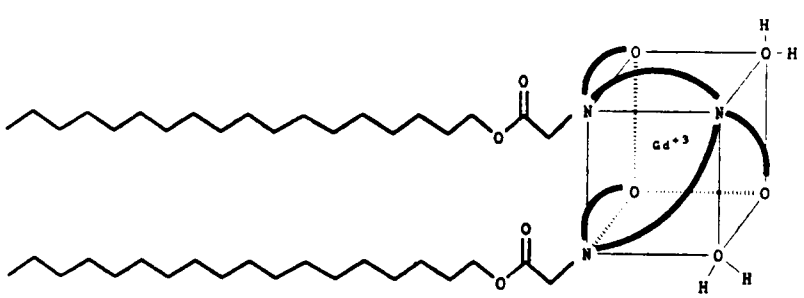

12

3. A Gd-DTPA Thiolester Derivative

Another linkage that could be utilized for the attachment of the hydrophobic alkyl tails to the hydrophilic DTPA is the thiolester functional group. Although thiolesters are not often used in laboratory syntheses, they are of great importance in syntheses that occur within living cells. One of the most important thiolesters is acetyl coenzyme A (acetyl CoA), 13. In certain biochemical reactions, acetyl CoA operates as an acylating agent; i.e. it transfers an acetyl group to another species by nucleophilic attack at the acyl carbon of the thiolester group. Thiolesters are known as high-energy compounds and are more reactive than their oxygen ester analogues.[128] Therefore, a Gd-DTPA derivative was developed in which gadolinium was incorporated into a DTPA amphiphile containing thiolester linkages.

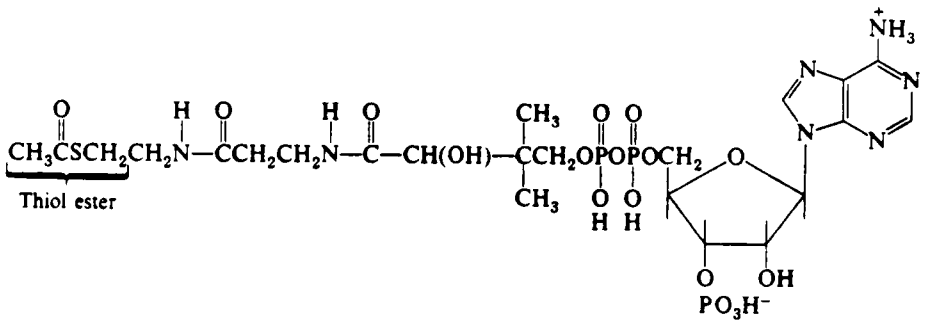

13

The reason that thiolesters are more reactive toward nucleophiles than ordinary esters is illustrated by the resonance structures shown in Figure 24. A resonance structure of the type shown in Figure 24b stabilizes an oxygen ester and

makes the carbonyl group less susceptible to nucleophilic attack. By contrast, thiolesters are not as effectively stabilized by the similar resonance structure shown in Figure 24d because this structure requires overlap between the 3p orbital of the sulfur atom and 2p orbital of the carbon atom. In addition, the carbon-sulfur bond of a thiolester is weaker than the carbon-oxygen bond of an oxygen ester, i.e. RS^- is a better leaving group than RO^-.

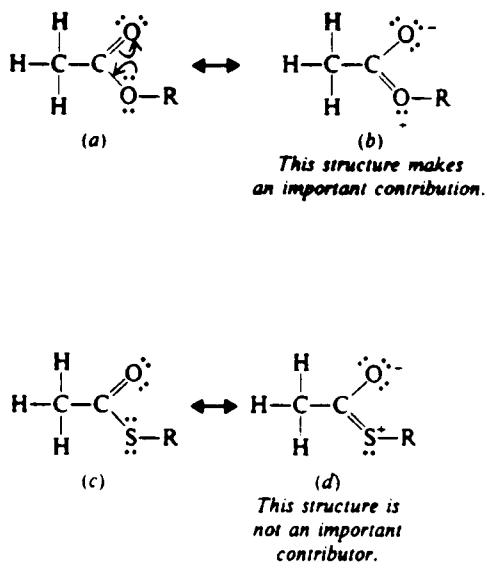

Figure 24. Resonance structure comparison of ester and thiolester functional groups.

One method for the synthesis of thiolester compounds involves the reaction of an anhydride with a thiol (R-SH) in the presence of a base.[129] This procedure was employed for the preparation of the DTPA thiolester derivative. Since sulfur is less electronegative than oxygen, the sulphur atoms in thiols carry relatively less negative charge and are less nucleophilic than the corresponding oxygen atoms in

alcohols. Therefore, thiols undergo acylation less readily than their oxygen analogues. As a result, these reactions reach an equilibrium which lies notably further towards the side of the starting materials.[130] However, the equilibrium can be shifted in the desired direction, resulting in an increased yield of the desired thiolester compound, by using a large excess of one of the starting materials. Therefore, DTPA dianhydride was allowed to react with eight equivalents (300% excess) of stearyl thiol using pyridine as the solvent to yield (>90%) the distearylthiolester derivative of DTPA (DTPA-ST), 14, as illustrated in equation 17. When the reaction was performed using only two equivalents of the starting thiol, a large amount of the starting materials were recovered with very little thiolester production.

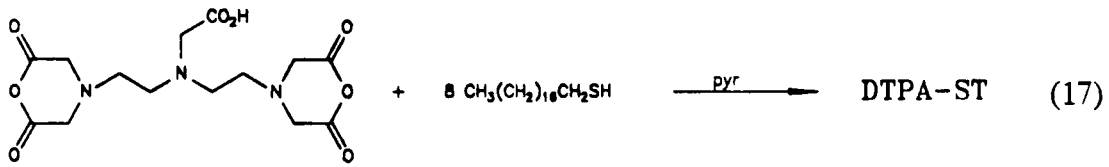

(17)

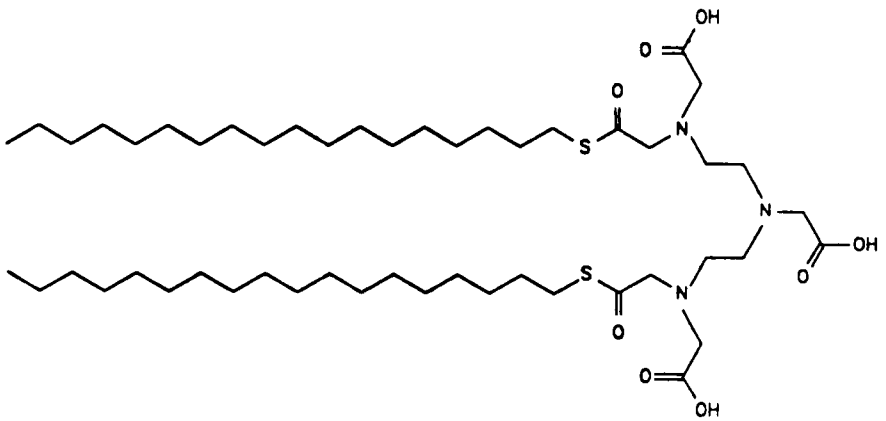

14

The thiolester derivative, DTPA-ST, was characterized by elemental analysis, IR spectroscopy and NMR spectroscopy (^{1}H and ^{13}C). The results of elemental analysis were in good agreement with the distearylthiolester structure. The ^{13}C and ^{1}H NMR spectra of DTPA-ST are shown in Figures 25 and 26, respectively. In the ^{13}C spectrum, three signals corresponding to the various carbonyl carbons occur in an approximate 2:2:1 ratio, however, one of the signals occurs extremely downfield at 201 ppm. This signal corresponds to the carbonyl carbon of the thiolester functional group and its position verifies the enhanced electropositive character of that carbon which makes it very susceptible to nucleophilic attack. As in the ^{13}C spectrum of DTPA-SE (Figure 22), the signals corresponding to the DTPA methylene carbons (53-57 ppm) are not resolved. The integration and various chemical shift positions of the signals in the proton spectrum (Figure 26) are also indicative of the DTPA distearylthiolester structure 14. In the IR spectrum of DTPA-ST, the absorption band of the thiolester carbonyl group occurred at a lower wavenumber as compared to that of the ester carbonyl group in DTPA-SE (1690 vs 1735 cm^{-1}). This same phenomenon has been observed in the comparison of other ester and thiolester compounds and it has been postulated that the presence of the heavier sulfur atom is responsible for the displacement.[129]

The incorporation of gadolinium was achieved by the reaction of DTPA-ST with $GdCl_3$ using pyridine as the solvent to give the resulting Gd-DTPA distearylthiolester complex (Gd-DTPA-ST), 15. The complex was characterized by melting point, elemental analysis and IR spectroscopy. As expected, the MP of the complex was larger than that of the uncomplexed ligand. Elemental analysis revealed

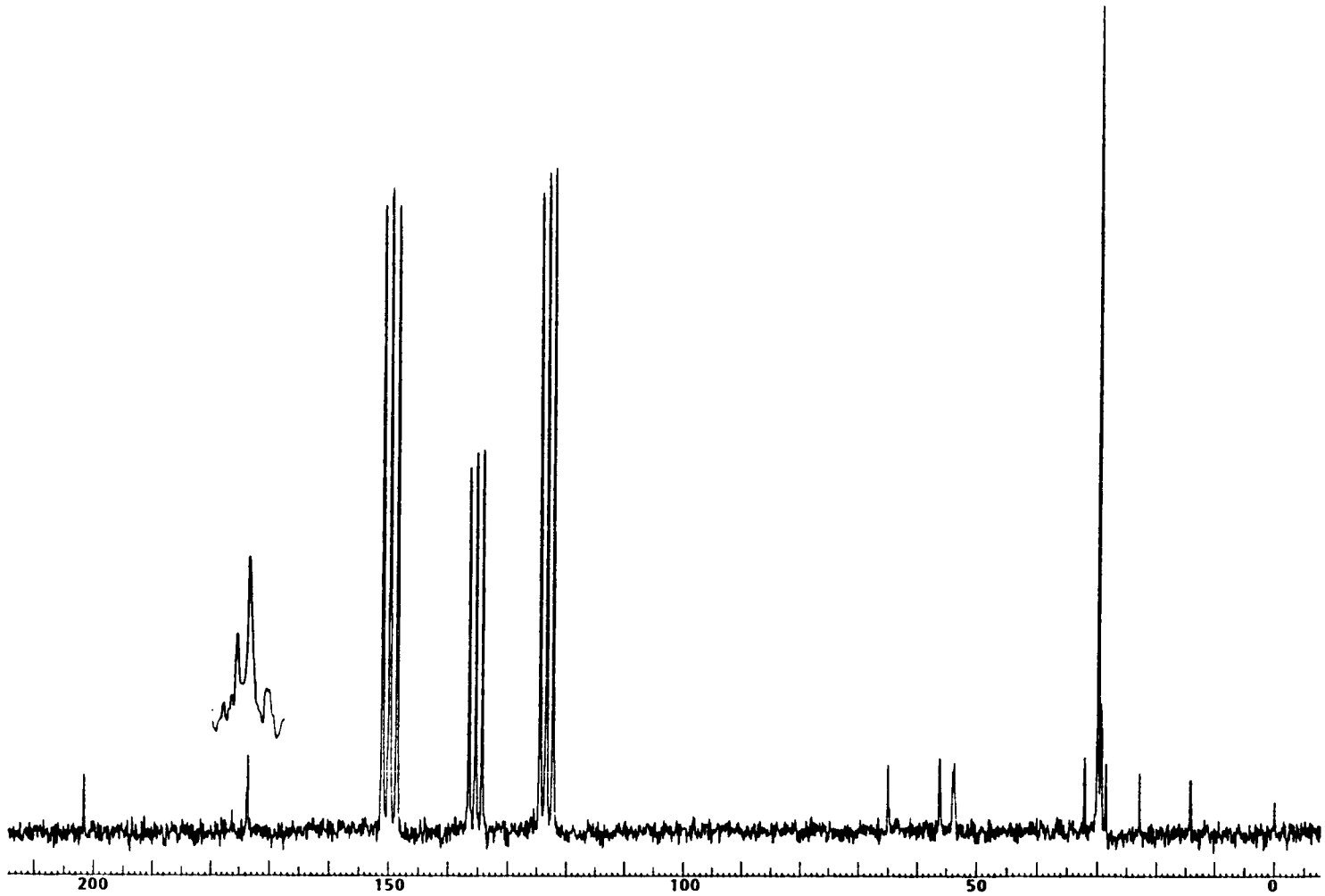

Figure 25. ^{13}C NMR spectrum of DTPA-ST in py-d_5.

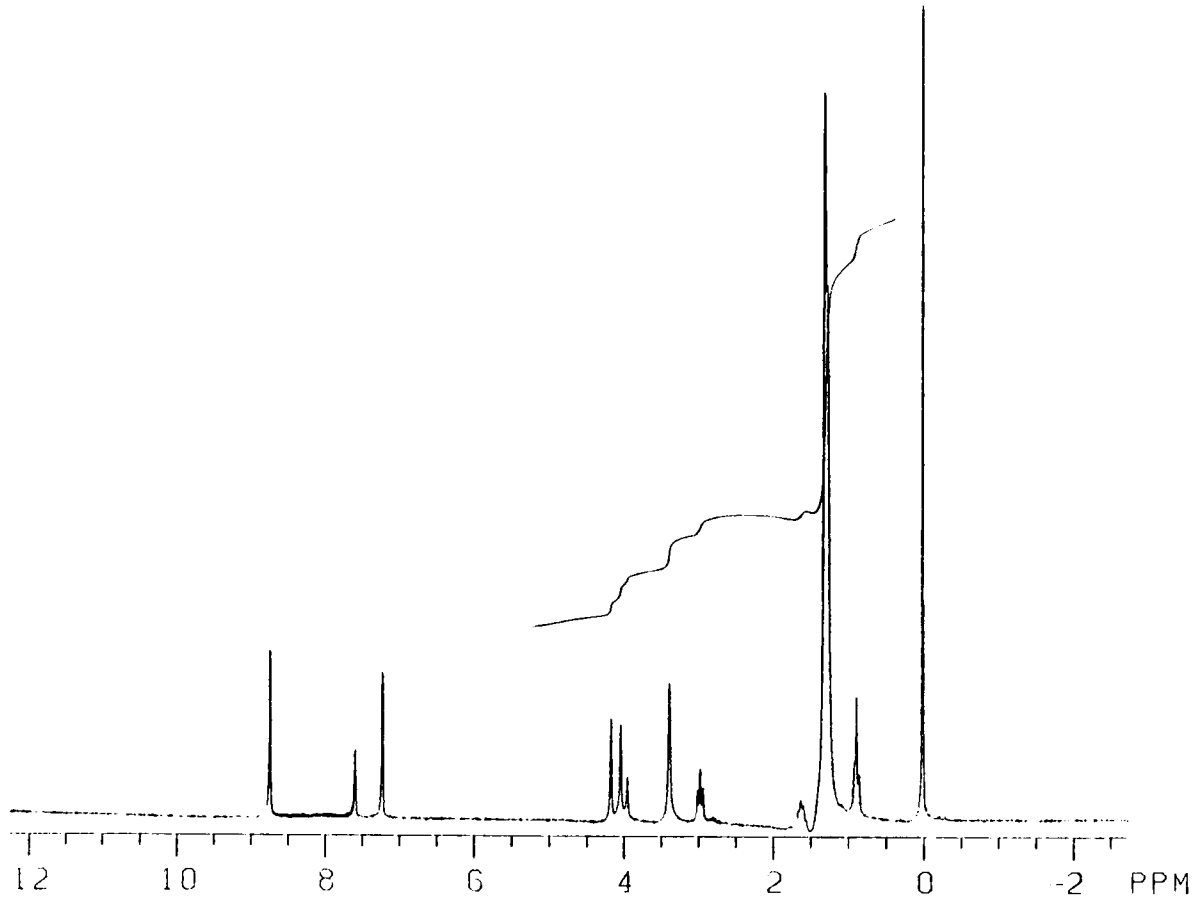

Figure 26. ^{1}H NMR spectrum of DTPA-ST in py-d_5.

that the species exists as the tetrahydrate. The Gd-DTPA-ST complex was used for the preparation of the GLL agents to be utilized in later biological studies.

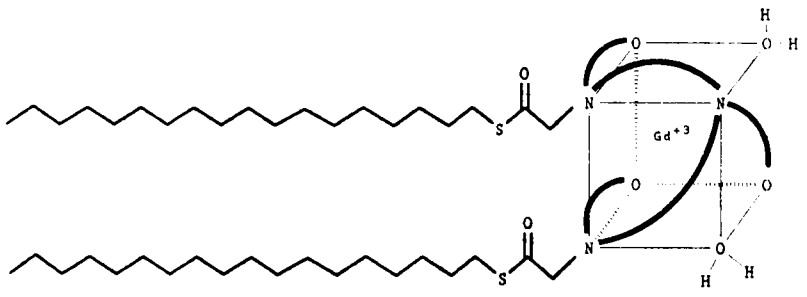

15

4. An IR Spectra Comparison of the Gd-DTPA Derivatives with the Uncomplexed DTPA Ligands

Since NMR spectroscopy could not be performed on the various Gd-DTPA derivatives due to paramagnetic effects, the only spectroscopic method utilized for their characterization was IR. In all the IR spectra obtained from the various complexes, an interesting phenomenon was observed involving a drastic change in the carbonyl region (1500-1800 cm^{-1}) as compared to the corresponding carbonyl region in the IR spectrum of the uncomplexed ligand. This effect is illustrated in the IR spectra of DTPA-SE and Gd-DTPA-SE as shown in Figures 27 and 28, respectively. This phenomenon has been observed in a multitude of coordination compounds[131] and can be explained in the following manner. To a good approximation, the vibration frequency of a bond is related to the masses of the vibrating atoms and the force constant of the vibrating bond by the following equation:

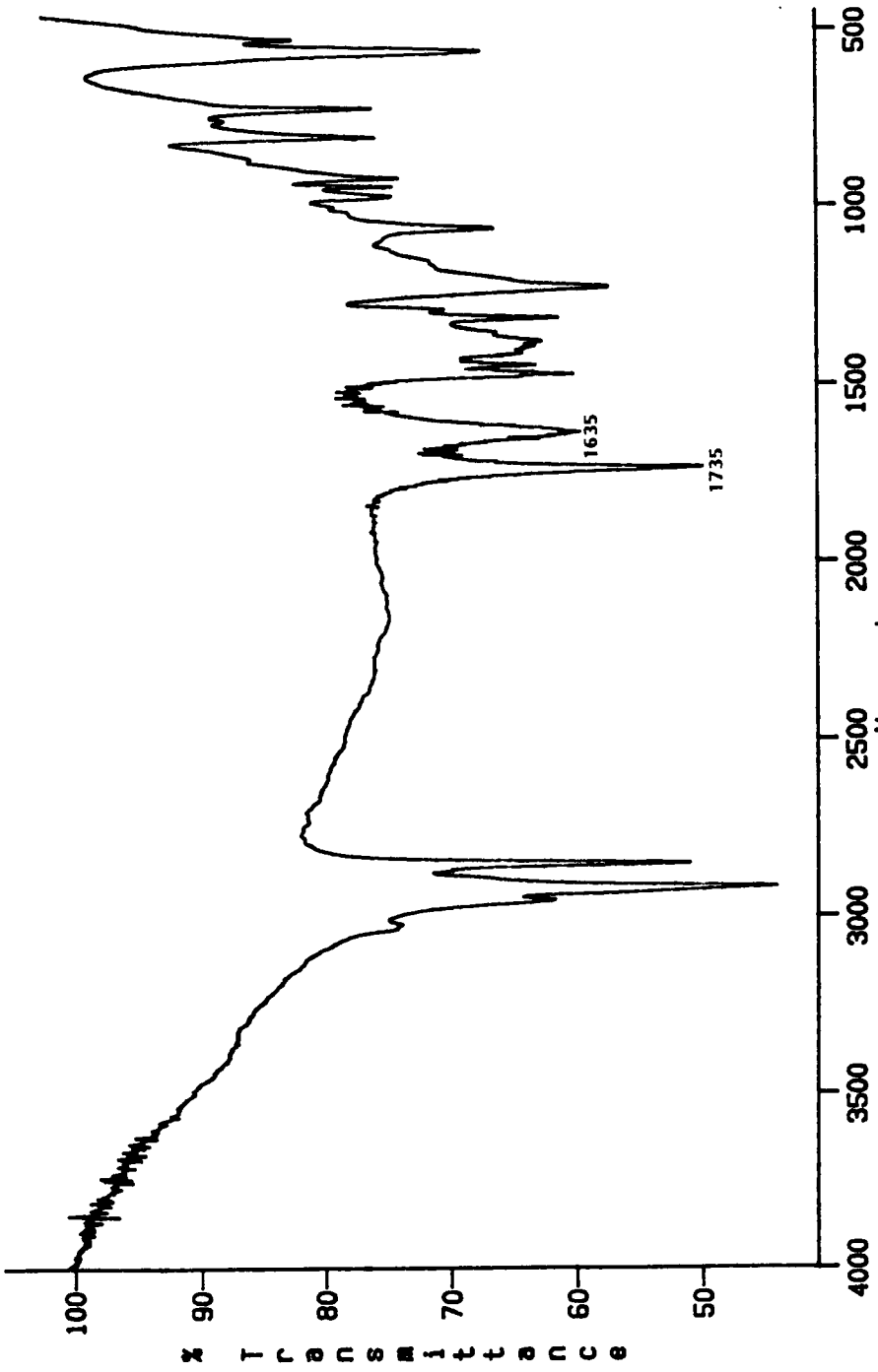

Figure 27. IR spectrum of DTPA-SE (KBr pellet).

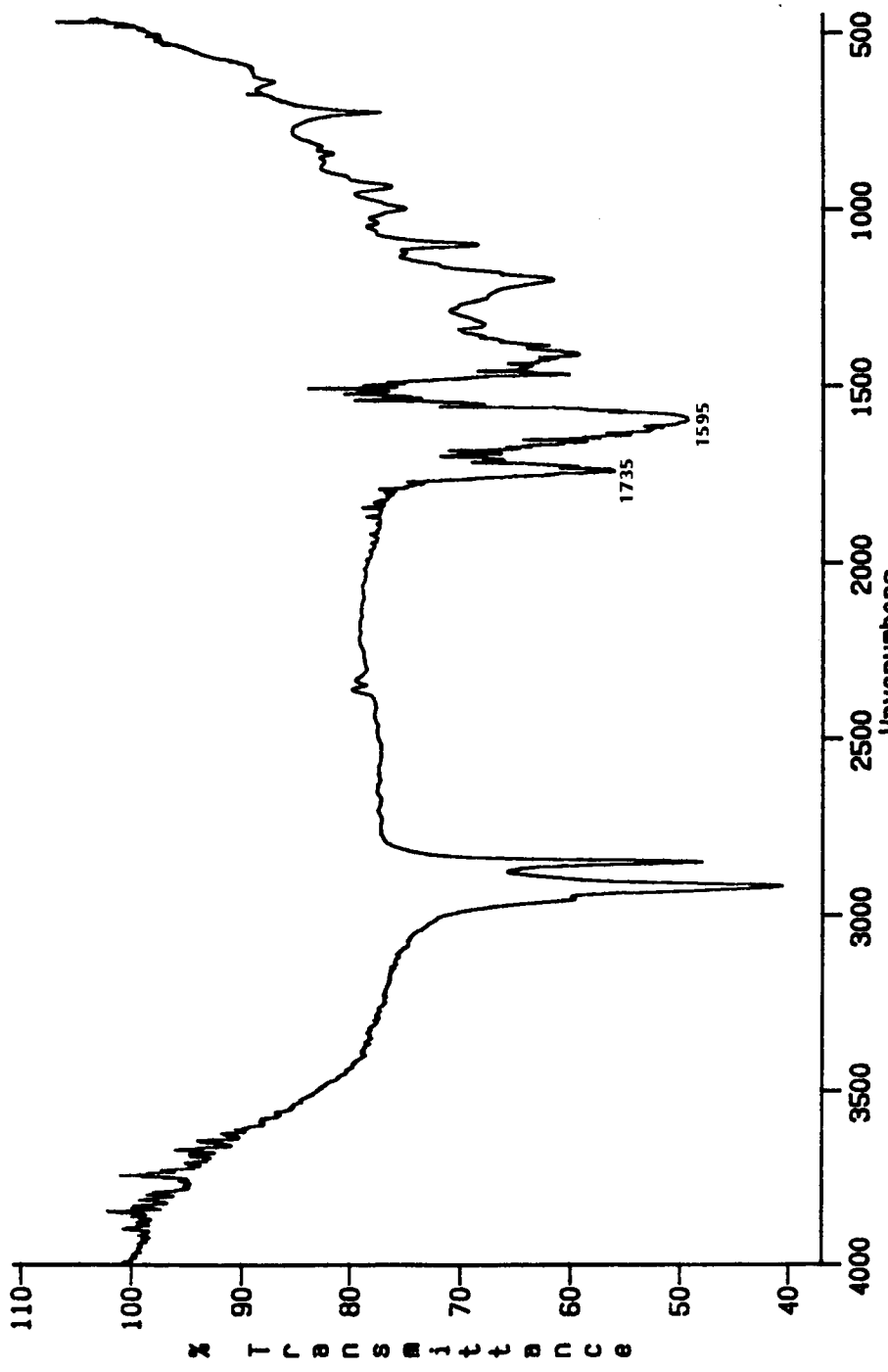

Figure 28. IR spectrum of Gd-DTPA-SE (KBr pellet).

$$\nu = [F(m_1 + m_2)/m_1m_2]^{1/2}/2\pi c \qquad (18)$$

where ν is the vibrational frequency in cm^{-1} (wavenumber), F is the force constant, m_1 is the mass of one atom, m_2 is the mass of the other atom and c is the velocity of light. As shown from the equation, the larger the force constant, the higher the vibrational bond frequency. Since the force constant is directly proportional to the bond order, the magnitude of the vibrational frequency is directly related to the bond order. For example, the absorption band for a carbon-carbon double bond occurs at a higher wavenumber than that for a carbon-carbon single bond.

In a study involving the complexation of various metals with EDTA, it was observed that the absorption band of the carbonyl bond in the unionized uncoordinated carboxylic acid group occurred at 1700-1750 cm^{-1} whereas the absorption band of the carbonyl bond in an ionized, coordinated carboxylate group occurred at 1590-1650 cm^{-1}.[132] This shift in the carbonyl absorption band to lower wavenumbers was attributed to a metal complexation interaction in which both oxygens of the carboxylate group are involved in the complexation and the bond order of the carbonyl group is decreased from 2 to 1.5.

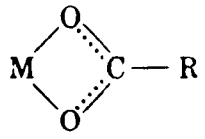

Based upon the above observations, the IR spectra obtained from the various Gd-DTPA derivatives, as compared to the uncomplexed ligands, can be interpreted. For example, in the IR spectrum of DTPA-SE (Figure 27), the major absorption

band in the carbonyl region occurs at 1735 cm^{-1} which corresponds to the carbonyl bonds of the two ester and two carboxylic acid groups that are connected to the two terminal amine nitrogens of DTPA. A smaller absorption band occurs at 1635 cm^{-1} which corresponds to an ionized carboxylate group, indicating that the species probably exists as a zwitterion. Since this absorption band also occurs in the IR spectrum of DTPA anhydride, as well as that of the free acid, it has been assigned to the carboxylic acid group attached to the central amine nitrogen of DTPA. In the IR spectrum of Gd-DTPA-SE (Figure 28), the major absorption band in the carbonyl region now occurs at 1595 cm^{-1} which corresponds to the three carboxylate groups complexed to the gadolinium ion. The shift of the absorption band to lower wavenumbers is presumably due to a decrease in the carbonyl bond order as a result of the metal complexation interaction previously illustrated. The smaller absorption band remaining at 1735 cm^{-1} corresponds to the carbonyl bond of the two ester groups which are probably not involved in the complexation. The strong absorption bands at 2920 and 2850 cm^{-1} observed in both spectra are due to the long saturated alkyl chains. Although the data obtained from IR does not describe the exact structure of the complex, it provides confirmation that complexation has occurred.

B. PREPARATION OF THE GADOLINIUM-LABELED LIPOSOMES

The GLL agents were prepared by the method employed for the preparation of the GLL agent containing 33 mol% Gd-DTPA-SA[116] in which an equimolar mixture of egg lecithin, cholesterol and an appropriate Gd-DTPA derivative was

used. The Gd-DTPA derivatives utilized were Gd-DTPA-SE, Gd-DTPA-ST and Gd-DTPA-DA. The resulting liposomes, in which the paramagnetic phospholipid analog is incorporated in the lamellar membrane, were SUV's having an average diameter of 0.05 μm (obtained by sonication for an appropriate time) as measured by negative-stain electron microscopy or by quasi-elastic (dynamic) light scattering. The various GLL agents obtained in this manner were used for the imaging studies. The radioactive liposomes, which were required for the biodistribution and elution profile studies, were prepared in the same manner but the appropriate ^{153}Gd-DTPA or ^{111}In-DTPA derivative was used.

C. BIODISTRIBUTION STUDIES OF THE GLL AGENTS

Following the successful preparation of the new Gd-DTPA derivatives, various biological tests were performed in order to compare their in-vivo characteristics with those of Gd-DTPA-SA. In order to determine the distribution and biological lifetime of the various new GLL agents, biodistribution studies were performed on normal female Balb/c mice using gadolinium-153 as the radiotracer element. In each study, a preparation containing 90 μmol lipid/ml which is equivalent to 0.15 mmol/kg of gadolinium was used. A standard dose of the liposome (intravenously injected) consisted of 150 μl per 30 g mouse. The results of the various biodistribution studies are shown in Figure 29.

The results from the biodistribution study utilizing the GLL agent containing 33 mol% ^{153}Gd-DTPA-SE (Figure 29a) indicate that the agent is cleared from the blood and accumulates in the liver and spleen. Eight hours after injection, 52% of

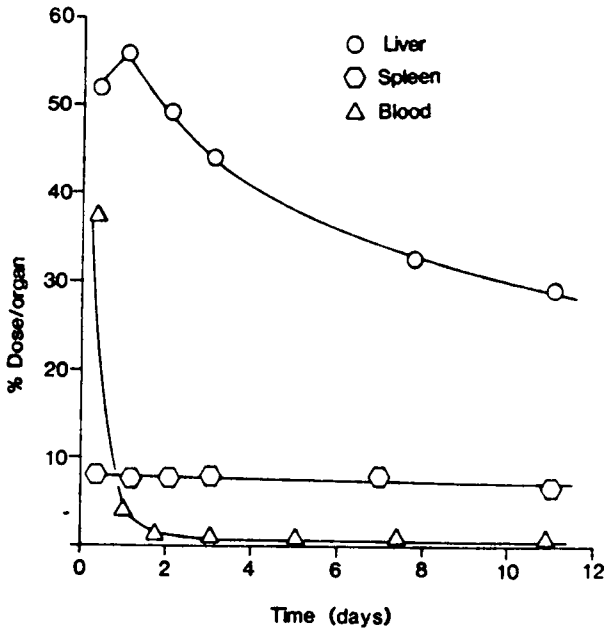

(a)

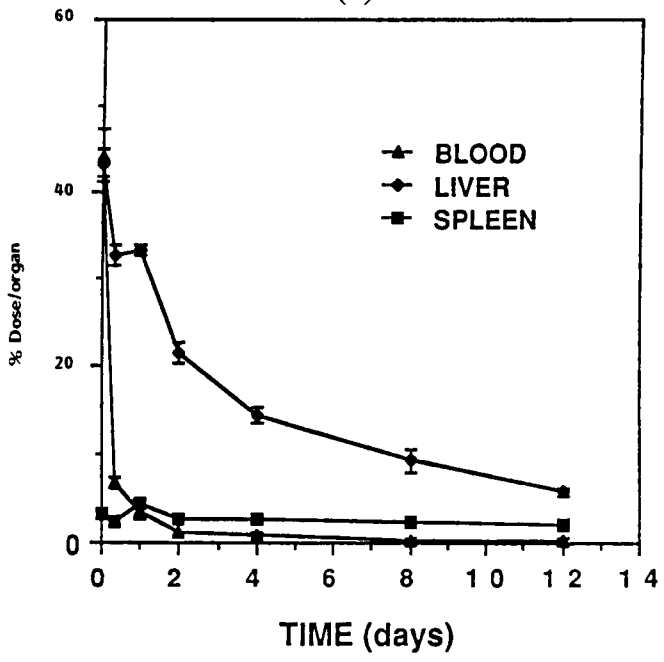

(b)

Figure 29. Biodistribution graphs of GLL agents containing (a) Gd-DTPA-SE, (b) Gd-DTPA-ST, (c) Gd-DTPA-DA and (d) In-DTPA-SA.

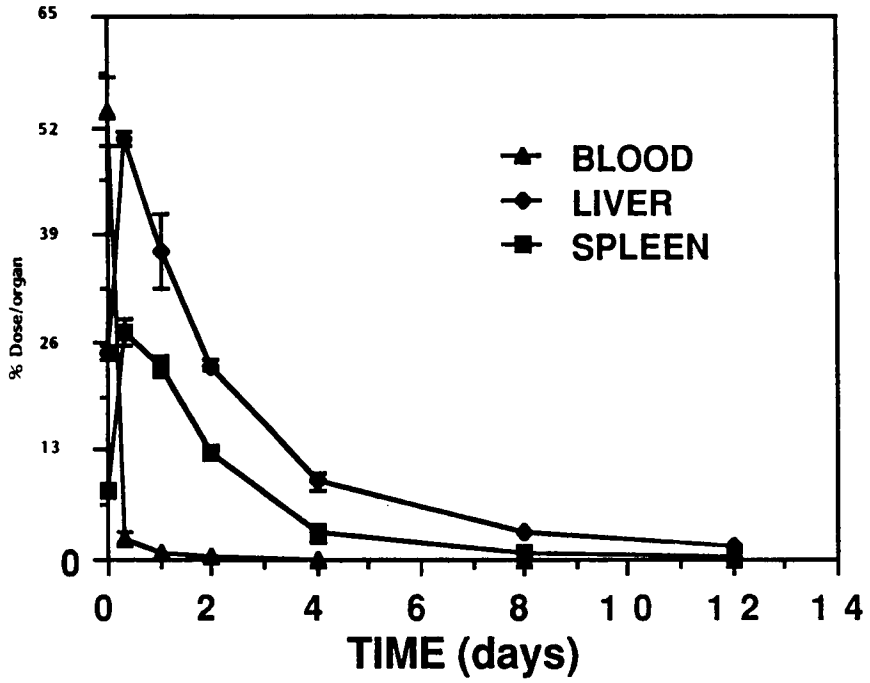

(c)

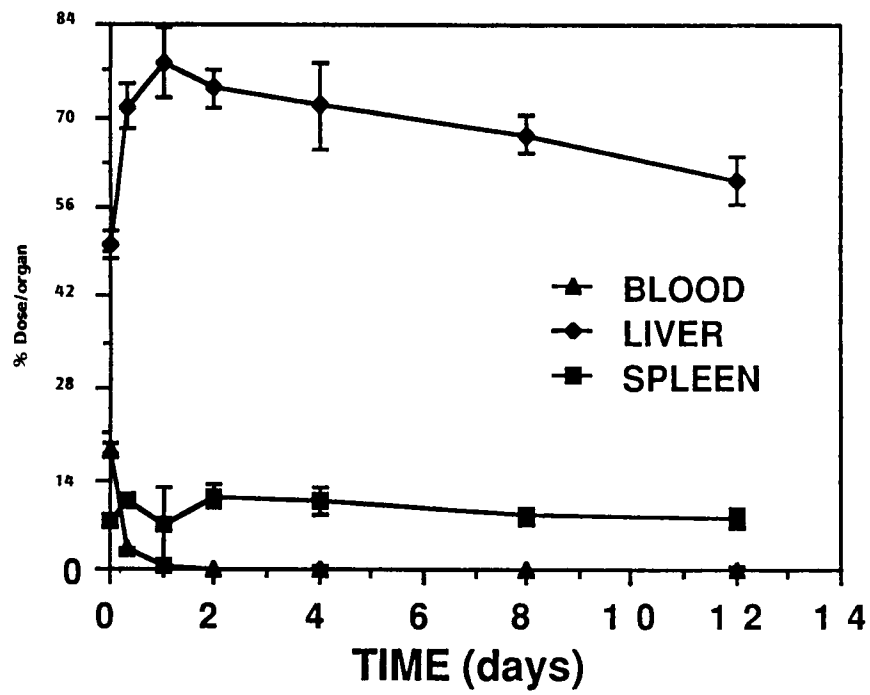

(d)

Figure 29 (continued)

the recovered dose was found in the liver, 38% was found in the blood and 8% was found in the spleen. However, 24 hours after injection, 56% of the dose was found in the liver, 8% was found in the spleen but only 5% was found in the blood. The results also show that the GLL agent containing ^{153}Gd-DTPA-SE is cleared from the liver more rapidly than the previous GLL agent containing ^{153}Gd-DTPA-SA, presumably as a consequence of the more labile nature of the ester linkages in the acidic environment of the liver. Eleven days after injection, all of the original liver accumulation of ^{153}Gd-DTPA-SA remained in the liver (Figure 19) whereas 50% of the ^{153}Gd-DTPA-SE accumulation had cleared from the liver in the same time period. Although this was an improvement in the clearance rate, it was far from ideal. Since the expected degradation product (Gd-DTPA) has a half-life of a few hours in the liver, the amphiphile is presumably being stored intact which is consistent with the increased clearance of the agent containing the chemically more labile ester linkage. The amount of the GLL agent containing ^{153}Gd-DTPA-SE found in the spleen remained constant with time which was identical to the result obtained with the GLL agent containing ^{153}Gd-DTPA-SA. There was only a nominal amount of radioactivity detected in the lung, heart and kidney at any given time point.

The results from the biodistribution study utilizing the GLL agent containing 33 mol% ^{153}Gd-DTPA-ST (Figure 29b) also indicate that the agent is cleared from the blood and accumulates in the liver and spleen. Fifteen minutes after injection, 43% of the recovered dose was found in the liver and 44% was found in the blood. However, eight hours after injection, 32% of the dose was found in the liver but only

7% was found in the blood. The results also show that after a period of two days, 50% of the GLL agent containing ^{153}Gd-DTPA-ST had cleared from the liver and only 14% of the original liver accumulation remained after a period of 12 days. This is a significantly more rapid clearance rate than that exhibited by the GLL agent containing ^{153}Gd-DTPA-SE ($t_{1/2}$ = 11 days) and is approaching acceptable levels. This result is consistent with the increased reactivity of the thiolester linkage as compared to that of an ester linkage. As with the previous GLL agents, the dose of the agent found in the spleen remained constant with time. Only a nominal amount of radioactivity was detected in the other organs tested at any given time point.

The results from the biodistribution study utilizing the GLL agent containing 33 mol% ^{153}Gd-DTPA-DA (Figure 29c) reveal the agent clears from the blood and accumulates in the liver and spleen. Fifteen minutes after injection, 54% of the recovered dose was found in the blood, 25% was found in the liver and 8% was found in the spleen. However, eight hours after injection, 51% of the dose was found in the liver, 27% was found in the spleen but less than 3% was found in the blood. The results also show that after a period of two days, 50% of the highest liver accumulation of the GLL agent containing ^{153}Gd-DTPA-DA had cleared from that organ and less than 2% remained after a period of 12 days which is comparable to the clearance rate achieved with the GLL agent containing ^{153}Gd-DTPA-ST. The most interesting result obtained from this study was the increased percent accumulation of the agent in the spleen as well as the rapid clearance of the agent from that organ, neither of which had been observed with any of the previous GLL agents. After a period of two days, 50% of the highest spleen accumulation (27%)

had cleared and the agent was virtually nonexistent in that organ after a period of twelve days. The increased selectivity of the GLL agent containing ^{153}Gd-DTPA-DA for the spleen and the clearance of the agent from that organ are possibly due to a change in the physical characteristics of the liposome resulting from the decreased hydrocarbon chain length of the Gd-DTPA derivative. Only a nominal amount of radioactivity was detected in the heart, lung and kidney at any given time point.

The biodistribution study previously performed by Kabalka and coworkers[116] utilizing the GLL agent containing ^{153}Gd-DTPA-SA was repeated. It was later discovered that the mice used in the initial experiment were infected with murine hepatitis virus; therefore, the data was somewhat questionable. In the repeat experiment, the liposomes contained 33 mol% Gd-DTPA-SA and a minute amount (<0.4 mol%) of ^{111}In-DTPA-SA was added to be utilized as the radiotracer. The results of the repeat experiment (Figure 29d) were similar to those obtained in the initial experiment (Figure 19) in which the agent clears from the blood and accumulates in the liver and spleen. However, whereas the agent remained in the liver indefinitely in the initial experiment, 22% of the highest liver accumulation had cleared from that organ after a period of 12 days. Although the increased clearance is possibly due to the utilization of healthy mice, a similar increase in the metabolism of In-DTPA complexes as compared to Gd-DTPA complexes was observed in the elution profile studies as will be discussed in the following section. The results of the repeat biodistribution study show that the clearance of the GLL agent containing Gd-DTPA-SA is still much slower than that of the various agents previously discussed.

The various biodistribution studies revealed that the in-vivo stability of the liposomal preparations can be altered by changing the chemical bonds which attach the hydrophobic alkyl chains to the hydrophilic Gd-DTPA complex or by decreasing the length of the alkyl chains. In addition, decreasing the alkyl chain length of the Gd-DTPA derivative possibly increases the selectivity of the resulting GLL agent for the spleen. The increased clearance rate of the GLL agents containing Gd-DTPA-SE or Gd-DTPA-ST as compared to the agent containing Gd-DTPA-SA is presumably due to the chemical instability of the paramagnetic amphiphiles. In contrast, while the Gd-DTPA-DA complex is chemically stable, the increased clearance rate of the GLL agent containing this species is presumably due to the biological instability of the amphiphile. For this reason, the Gd-DTPA-DA complex has the greatest commercial potential because it's chemical stability allows for liposomal formulation without degradation of the amphiphile. The Gd-DTPA derivatives containing labile linkages have the potential for degradation under certain conditions.

D. SERUM STABILITY STUDIES OF THE GLL AGENTS

Serum stability experiments were performed in an effort to monitor the fate of the various liposomal agents once they have entered the blood stream. The experiments were conducted prior to and after incubation of an agent containing one of the radioactive amphiphiles at 37 °C in normal human serum at various time points. The number and relative amounts of the various radioactive species resulting

from incubation were determined by gel-filtration chromatography [122,128] in which separation is achieved on the basis of size. In this procedure, a mixture is passed through a column containing very small porous beads of a highly hydrated polymer. Smaller species can penetrate into the pores in the beads and thus are retarded in their flow down the column but larger species cannot penetrate into the beads and pass down the column more rapidly. Species of intermediate size will pass down the column at intermediate rates depending on the degree of which they can penetrate into the beads.

The initial serum stability experiments were performed on the GLL agent containing ^{153}Gd-DTPA-ST because it appeared to have the shortest biological lifetime as compared to the long chain amide and ester derivatives as illustrated in the biodistribution studies. The results from these experiments are shown in Figure 30. The elution profile conducted prior to serum incubation (Figure 30a) resulted in a single peak which corresponds to the radioactive liposome indicating that the Gd-DTPA thiolester derivative remains intact during liposome preparation. The elution profiles conducted at 15 min. and 1 hour after incubation (Figures 30b and 30c, respectively) show the presence of two peaks; the first to elute corresponds to the liposome peak and the second corresponds to a radioactive species which possibly results from the extraction of the Gd-DTPA derivative by serum proteins. The elution profiles conducted at 5 hours and 24 hours after incubation (Figures 30d and 30e, respectively) show the presence of a third peak, in addition to the previous two, corresponding to a smaller radioactive species which could possibly be the

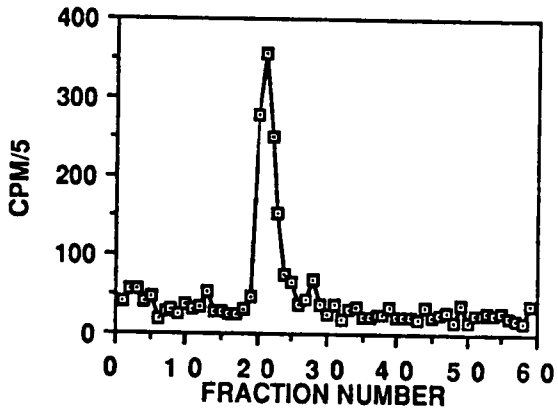

(a)

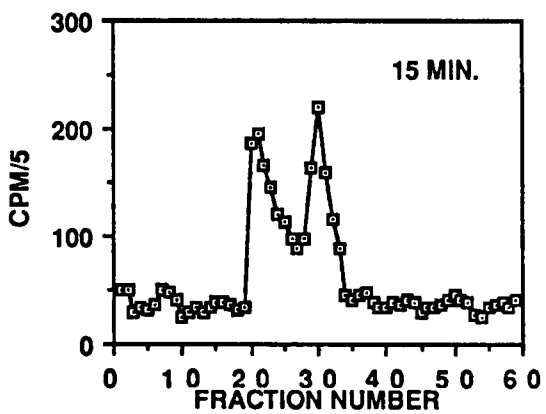

(b)

Figure 30. Elution profiles of a GLL agent containing Gd-DTPA-ST conducted (a) prior to serum incubation, (b) 15 minutes after serum incubation, (c) 1 hour after serum incubation, (d) 5 hours after serum incubation and (e) 24 hours after serum incubation.

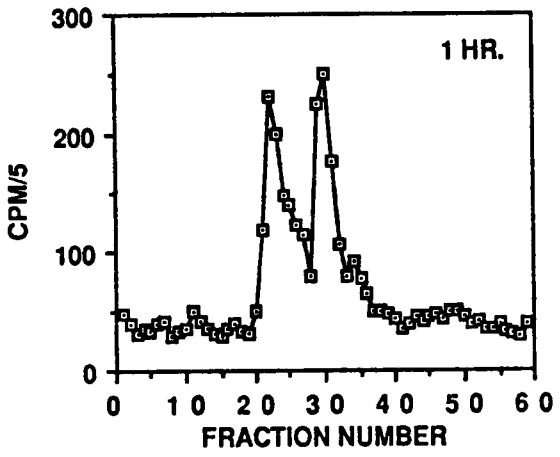

(c)

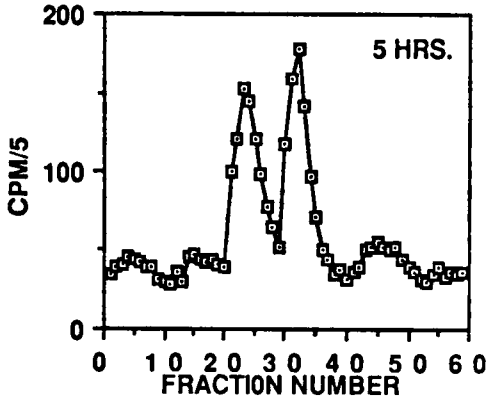

(d)

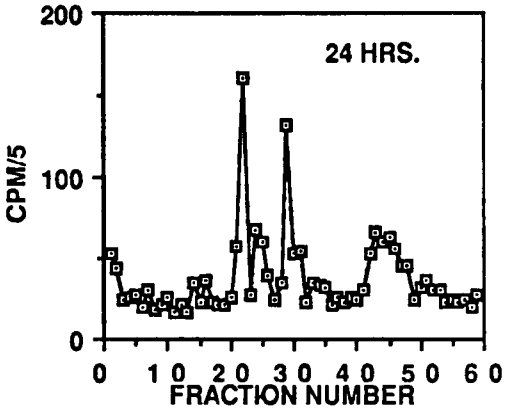

(e)

Figure 30 (continued)

^{153}Gd-DTPA hydrolysis product resulting from the interaction of the serum and ^{153}Gd-DTPA-ST.

Further serum stability experiments were conducted to compare the blood metabolism of the various liposomal agents containing either the long chain amide, ester or thiolester amphiphiles. In these experiments, the various DTPA chelates were complexed with indium-111 instead of gadolinium-153 because the former has a much shorter half-life (67 hours vs 242 days).[133] It was assumed that the substitution of indium for gadolinium was valid because In-DTPA has a formation constant of 10^{28} versus 10^{23} for Gd-DTPA.[134] The elution profiles conducted on the agent containing ^{111}In-DTPA-SA prior to and after incubation for 1 hour and 24 hours are presented in Figure 31. A single peak corresponding to the intact liposome was obtained at each time point. These results were in agreement with the remarkable liposome stability demonstrated in previous experiments. The elution profiles conducted on the agents containing either ^{111}In-DTPA-SE or ^{111}In-DTPA-ST are shown in Figures 32 and 33, respectively. In each case, the results were similar to those obtained in the initial serum stability study utilizing the GLL agent containing ^{153}Gd-DTPA-ST (Figure 30); one peak was obtained prior to incubation (Figures 32a and 33a), two peaks were obtained 1 hour after incubation (Figures 32b and 33b) and the third peak corresponding to the hydrolysis product was present 24 hours after incubation (Figures 32c and 33c). However, the rate of formation of the species corresponding to the third peak is greater with the liposomes containing ^{111}In-DTPA-SE or ^{111}In-DTPA-ST as compared to the agent containing ^{153}Gd-DTPA-ST (Figures 32c and 33c versus 30e). This observation supports the generation of the

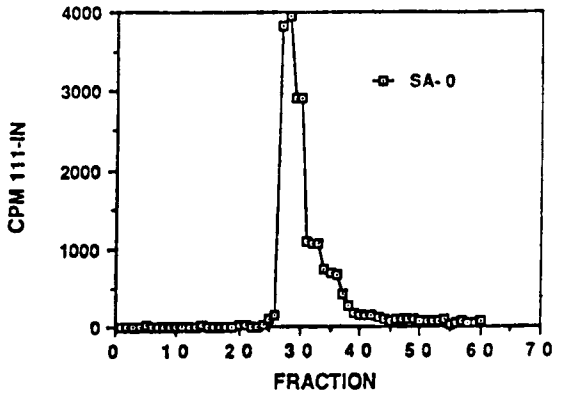

(a)

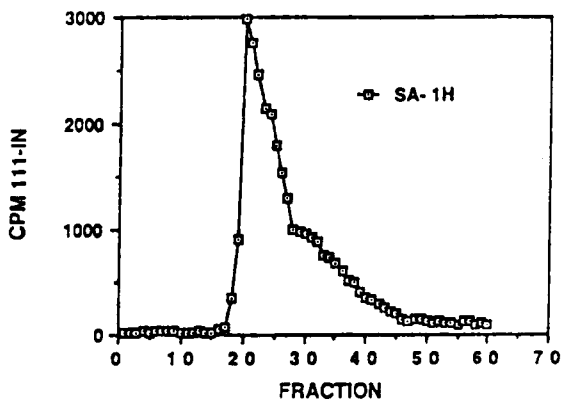

(b)

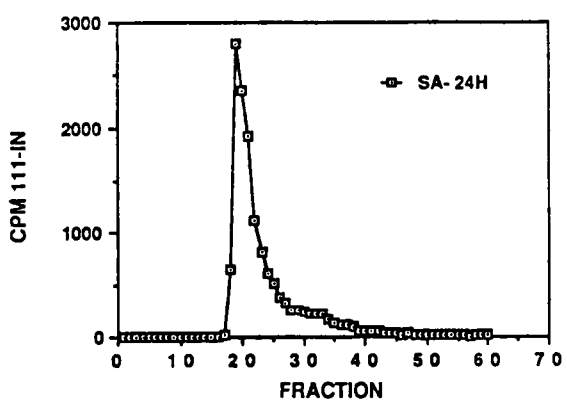

(c)

Figure 31. Elution profiles of a ILL agent containing In-DTPA-SA conducted (a) prior to serum incubation, (b) 1 hour after serum incubation and (c) 24 hours after serum incubation.

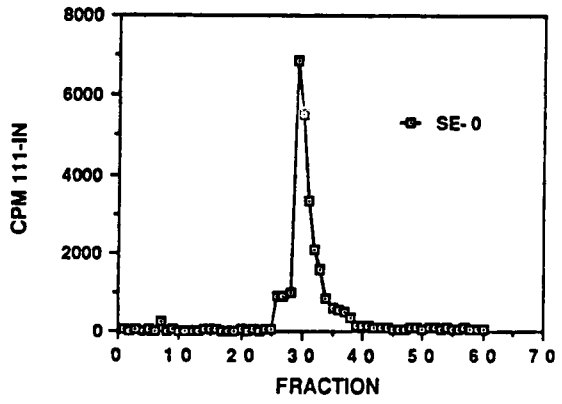

(a)

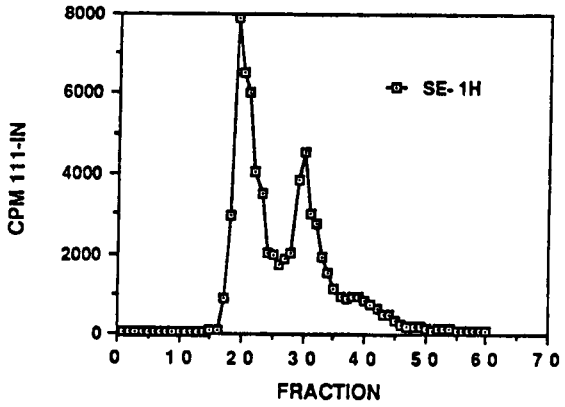

(b)

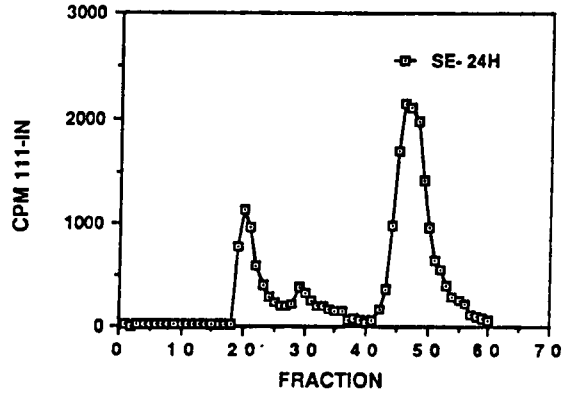

(c)

Figure 32. Elution profiles of a ILL agent containing In-DTPA-SE conducted (a) prior to serum incubation, (b) 1 hour after serum incubation and (c) 24 hours after serum incubation.

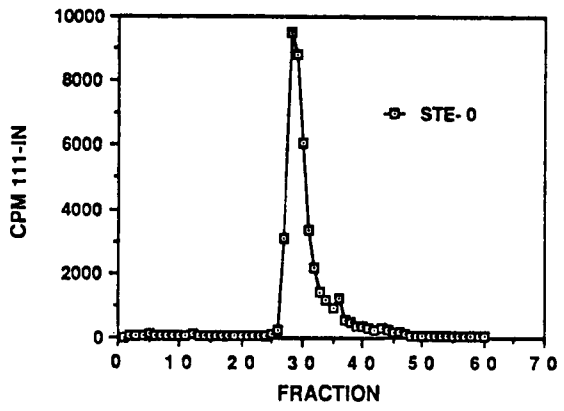

(a)

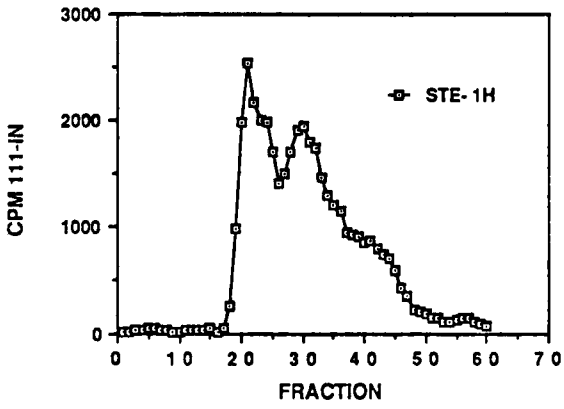

(b)

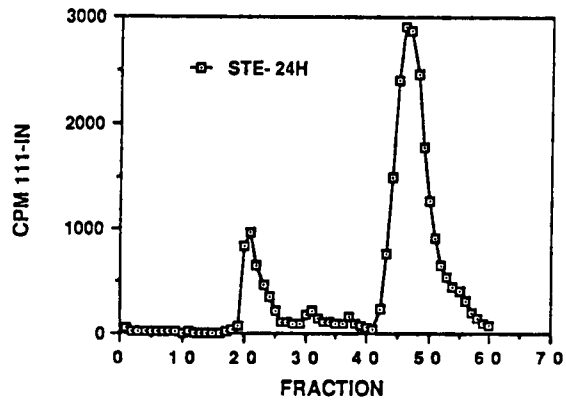

(c)

Figure 33. Elution profiles of a ILL agent containing In-DTPA-ST conducted (a) prior to serum incubation, (b) 1 hour after serum incubation and (c) 24 hours after serum incubation.

hydrolysis product because if the peak corresponded to a free metal ion resulting from uncomplexation, one would expect the opposite effect based on the formation constants.

The results of the various serum stability studies indicate that the liposomal agent containing the DTPA-SA amphiphile remains intact upon introduction to the blood stream. However, the liposomal agents containing either the DTPA-SE or DTPA-ST derivatives are metabolized upon introduction to the blood and the metabolism increases as time progresses. These results are in general agreement with the biodistribution data presented earlier.

E. IMAGING STUDIES USING VARIOUS GLL AGENTS

Magnetic resonance imaging studies were performed to determine if visual contrast enhancement of the liver could be obtained using the GLL agents. Coronal T_1-weighted spin echo images (i.e. short TR, short TE) were obtained on normal female Balb/c mice prior to and after injection of the various GLL agents. The resulting images are presented in Figure 34. Contrast enhancement values were calculated by relating the pixel intensity values, I, of the target organ (liver) to an unaffected organ (brain) according to the following equation:

$$\% \text{ Contrast Enhancement} = (RI_{post} - RI_{pre})/RI_{pre} \times 100 \qquad (19)$$

where RI_{post} is the relative intensity (I_{liver}/I_{brain}) following injection and RI_{pre} is the relative intensity (I_{liver}/I_{brain}) prior to injection.

The image presented in Figure 34a was obtained 30 minutes after injection of the GLL agents using a TR of 200 ms and a TE of 13 ms. In the experiment,

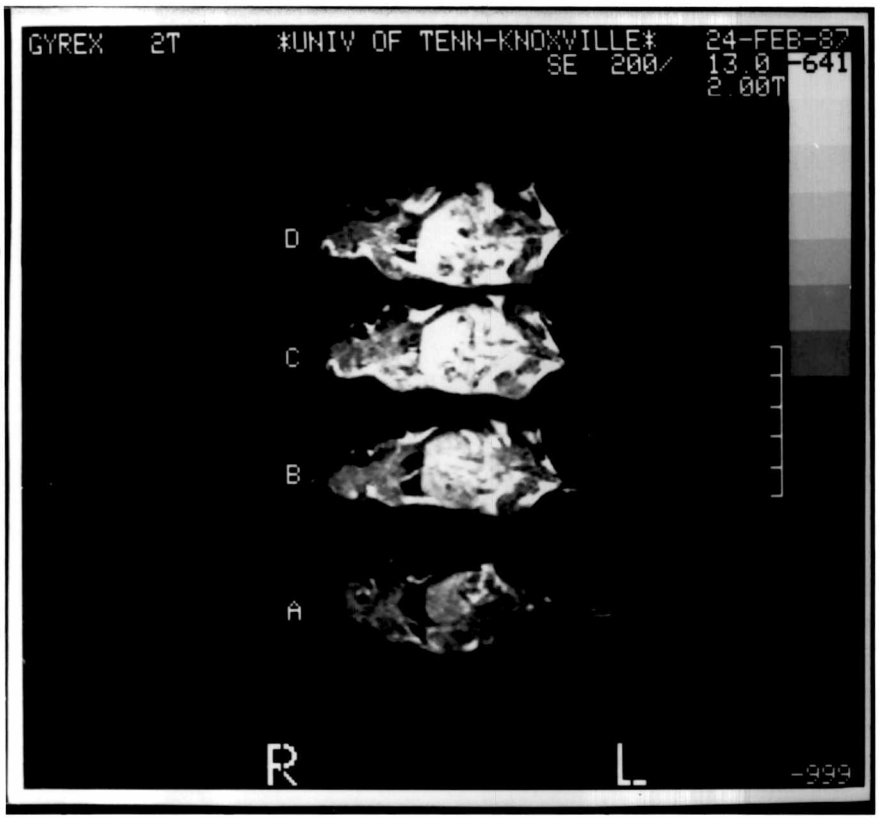

(a)

Figure 34. MRI contrast enhancement studies utilizing (a) Gd-DTPA-SA and Gd-DTPA-SE, (b) Gd-DTPA-SA, Gd-DTPA-SE and Gd-DTPA-ST and (c) Gd-DTPA-SA, Gd-DTPA-ST and Gd-DTPA-DA.

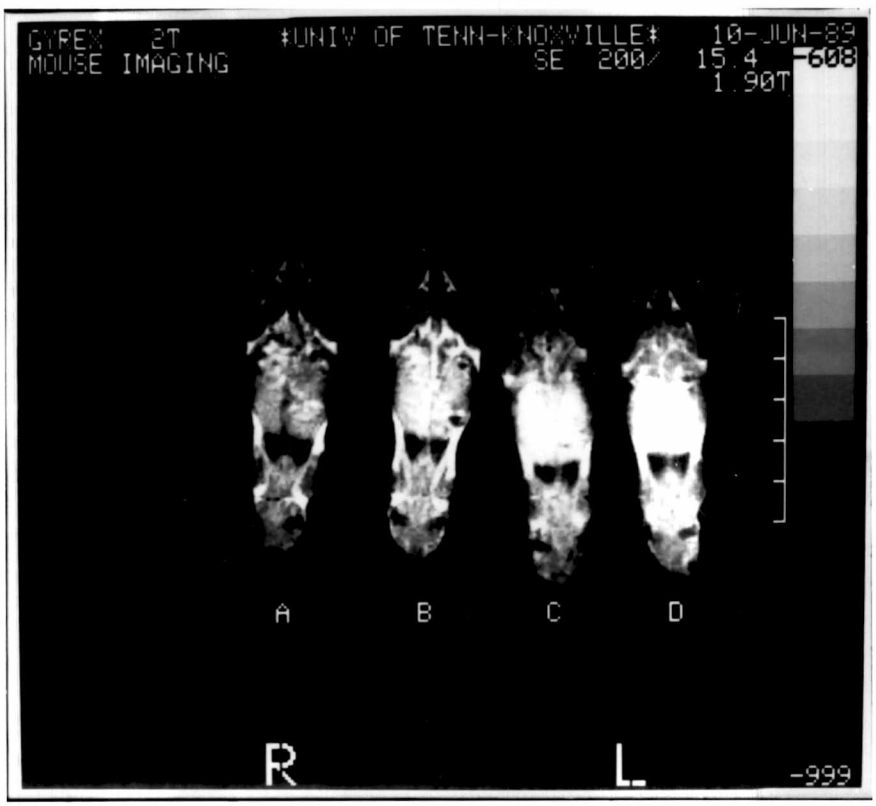

(b)

Figure 34 (continued)

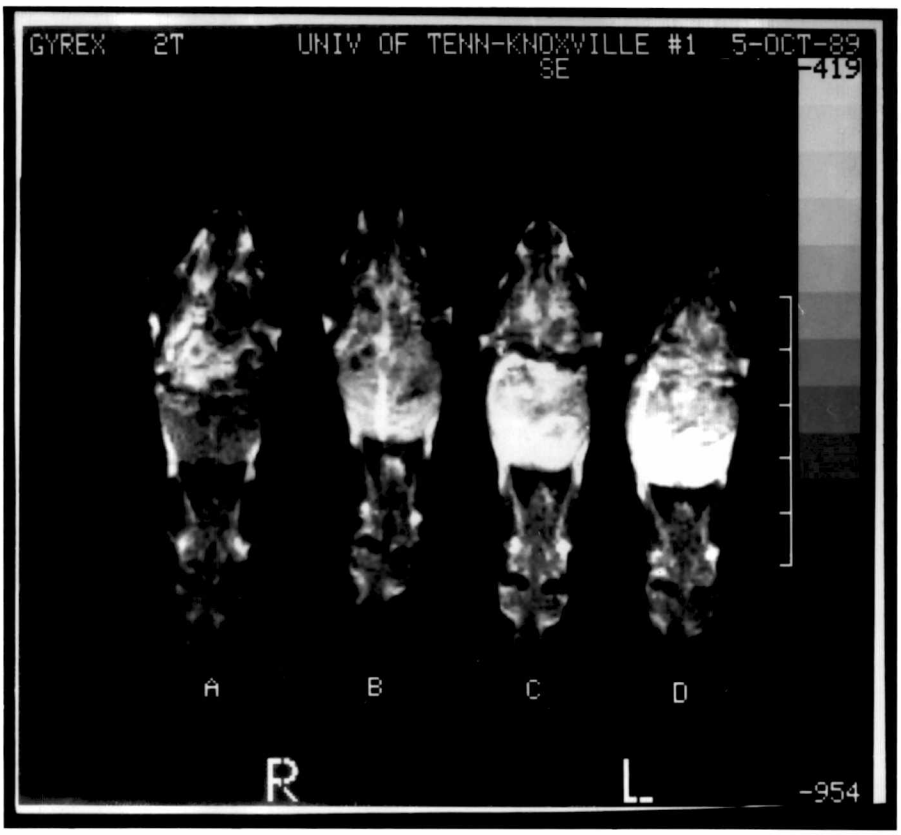

(c)

Figure 34 (continued)

mouse A served as a control and received a dose of a nonparamagnetic liposome which was comprised of a 50:50 mixture of egg lecithin and cholesterol, mouse B received the GLL agent containing Gd-DTPA-SA at a dose corresponding to a gadolinium concentration of 0.15 mmol/kg, mouse C received the GLL agent containing Gd-DTPA-SE at an equivalent dose and mouse D also received the GLL agent containing Gd-DTPA-SE but at a dose corresponding to 0.30 mmol gadolinium/kg. The results show that the GLL agents accumulate in the liver of normal Balb/c mice within minutes. The GLL agent containing the diamide amphiphile resulted in a 52% liver enhancement (mouse B), whereas an equivalent dose of the GLL agent containing the diester derivative was even more effective, producing a 146% enhancement (mouse C). Doubling the quantity of the liposome did not lead to further enhancement; the GLL agent containing Gd-DTPA-SE at an increased dose resulted in a 144% enhancement (mouse D). A similar leveling effect was noted in the earlier in-vitro studies.[116,117] The higher dosage could be leading to aggregation of the liposomal preparation or the optimum concentration of the gadolinium ion might have been surpassed.

An additional imaging experiment was performed to compare the contrast enhancement abilities of the GLL agent containing Gd-DTPA-ST with the previous GLL agents containing the long chain amide or ester derivatives. The image is shown in Figure 34b and was obtained 1 hour after injection of the various GLL agents at a dose corresponding to 0.15 mmol gadolinium/kg using a TR of 200 ms and a TE of 15 ms. In the experiment, mouse A received the nonparamagnetic liposome and served as a control, mouse B received the GLL agent containing Gd-

DTPA- SA, mouse C received the GLL agent containing Gd-DTPA-SE and mouse D received the GLL agent containing Gd-DTPA-ST. As in the initial imaging experiment, the various agents accumulate in the liver. The GLL agent containing the diamide derivative resulted in a 40% contrast enhancement (mouse B) and the GLL agent containing the diester species produced a 97% enhancement (mouse C). The decrease in percent enhancement of the two agents as compared to the initial experiment (Figure 34a) was due to the utilization of a longer TE (15 ms vs 13 ms). Because relaxation is an exponential process, the increase in time before acquisition of the signal results in an appreciable loss of detectable magnetization. The utilization of the GLL agent containing the dithiolester derivative resulted in a 99% enhancement (mouse D) which is comparable to that of the agent containing the diester analogue. This result demonstrates that the biological lifetime of the gadolinium-labeled liposomes can be reduced without loss of their contrast enhancement capabilities.

A final imaging experiment was performed to compare the contrast enhancement abilities of the GLL agent containing the short chain amide complex (Gd-DTPA-DA) with the previous GLL agents containing the long chain amide (identical linkage) or thiolester (similar clearance rate) derivatives. This image is shown in Figure 34c and was obtained one hour after injection of the various GLL agents at a dose corresponding to 0.15 mmol gadolinium/kg using TR of 200 ms and a TE of 15 ms. In the experiment, mouse A received the nonparamagnetic liposome and served as a control, mouse B received the GLL agent containing Gd-DTPA-SA, mouse C received the GLL agent containing Gd-DTPA-ST and mouse D received

the GLL agent containing Gd-DTPA-DA. As in the previous two imaging experiments, the various agents result in visual contrast enhancement in the liver region. As in the previous experiment, Gd-DTPA-SA and Gd-DTPA-ST resulted in a 45% (mouse B) and 93% (mouse C) liver contrast enhancement, respectively. The GLL agent containing Gd-DTPA-DA resulted in a 102% contrast enhancement (mouse D) which is comparable to that obtained with the distearylthiolester complex. This result further demonstrates that the in-vivo lifetime of the agents can be reduced with little or no effect on their contrast enhancement abilities.

F. CONCLUSION

Liposomes containing paramagnetic amphipathic agents incorporated in the lamellar membrane significantly enhance the MR signal intensity in T_1-weighted spin echo images. The reagents appear to be suitable for contrast enhancement of the liver, spleen, bone marrow and other organs rich in macrophage activity with no apparent toxic effects. The in-vivo stability of the paramagnetic species can be altered by altering the chemical bonds which attach the hydrophobic portion of the amphiphile to the hydrophilic Gd-DTPA complex or by altering the length of the hydrophobic tails. By careful construction of the paramagnetic amphiphile and the resulting paramagnetic liposome, it will be possible to select the target organ and alter the in-vivo lifetime of the new agents. The resulting enhancement of the T_1 will generate images of greater contrast in the targeted organs and possibly improve differentiation between normal and pathologic processes. The further development as well as toxicological assays of the GLL agents is in need of investigation.

CHAPTER IV

EXPERIMENTAL METHODS

A. GENERAL

When required, glassware was oven-dried prior to use. All melting point determinations were obtained using a Fisher-Johns melting point apparatus and are uncorrected. All infrared spectra were obtained on a Biorad FTS-7 FT-IR spectrometer and are reported in cm^{-1}. All ^{1}H and ^{13}C NMR spectra were performed on either a Joel FX90Q FT-NMR spectrometer or a Nicolet 200 MHz FT-NMR spectrometer and are reported in ppm using tetramethylsilane (TMS) as an internal reference ($\delta = 0.0$ ppm). All magnetic resonance images were performed using a 30 cm Helmholtz (saddle-shaped) coil tuned to 81 MHz for hydrogen and a Gyrex 1.9 T, 90 cm bore, whole-body MRI unit (Elscint Corp.). Elemental analysis were provided by Galbraith Laboratories, Knoxville, Tennessee. All commercially obtained chemicals, their manufacturers and methods of purification, when applicable, are listed in Table 3. Thin layer chromatographic analysis were performed on Analtech Silica Gel GF 250 μm TLC plates using UV detection or a 10% phosphomolybdic acid in ethanol solution as an indicator. Sizing of liposomes was performed using a Hitachi H-600 electron microscope (Rockville, MD) or a Coulter N45D sub-micron particle size analyzer (Hialeah, FL). All radioactivity measurements were made on a Beckman 5500B gamma counter. Normal female

Table 3: Sources and Purification Methods of Commercially Available Chemicals

Chemicals and Abbreviations	Source[a]	Purification Method[b]
Acetic Acid (AcOH)	F	
Acetic Anhydride	F	
Butanol (BuOH)	M	
Chloroform ($CHCl_3$)	M	1
Chloroform-d ($CDCl_3$)	A	
Cholesterol	S	
Decylamine	A	
Diethylenetriaminepentaacetic Acid (DTPA)	A	
Diethyl Ether	M	
Dimethoxyethane (DME)	A	
Dimethylformamide (DMF)	M	
Dimethylsulfoxide-d_6 (DMSO-d_6)	A	
Dodecylamine	A	
Egg Lecithin (Phosphatidylcholine)	Av	
Ethanol (EtOH)	W	
Gadolinium-153 Trichloride ($^{153}GdCl_3$)	O	
Gadolinium Trichloride Hexahydrate ($GdCl_3 \cdot 6H_2O$)	A	
Hexadecylamine	A	
Indium-111 Trichloride ($^{111}InCl_3$)	D	

Table 3: (continued)

Chemicals and Abbreviations	Source[a]	Purification Method[b]
Indium Trichloride ($InCl_3$)	A	
Lithium Aluminium Hydride (LAH)	A	
Octadecanethiol	A	
Potassium Bromide (KBr)	A	
Pyridine (py)	M	2
Pyridine-d_5 (py-d_5)	A	
Sodium Hydroxide (NaOH)	M	
Stearic Acid	E	
Sulfuric Acid (H_2SO_4)	F	
Tetradecylamine	A	

[a] Sources

A = Aldrich
Av = Avanti Polar Lipids, Inc.
D = Dupont Medical Products
E = Emery Industries
F = Fisher Scientific
M = Mallinckrodt
O = Oak Ridge National Laboratory
S = Sigma
W = Warner-Graham

[b] Purification Methods

1. Distilled from P_2O_5 and stored under N_2 atmosphere

2. Pre-dried over KOH, distilled from BaO_2 and stored over KOH under N_2 atmosphere.

Balb/c mice (≈30 g) were provided by Harlan Sprague Dawley Company, Indianapolis, Indiana.

B. SYNTHETIC PROCEDURES

1. Preparation of DTPA Dianhydride

DTPA dianhydride was prepared by the method of Eckelman and coworkers.[119] In a typical experiment, DTPA (19.7 g, 0.05 mol) was suspended in 50 ml of dry pyridine in a dry 250 ml round bottom flask equipped with a condenser and a large egg-shaped magnetic stir bar. Acetic anhydride (20.4 g, 0.20 mol) was added and the mixture was heated with stirring at 65 °C using an oil bath for 24 hours to yield a dark brown suspension. The insoluble product was collected by vacuum filtration, washed thoroughly with acetic anhydride followed by ether and dried in an oven at 50-60 °C for 24 hours to give 16.05 g (89.9%) of a fine, white powder. The product was stored in a vacuum desiccator until further use and showed no signs of hydrolysis after several months of storage. The melting point, IR spectrum and ^{1}H NMR spectrum were in good agreement with literature values; mp 175-185 °C (dec); ^{1}H NMR (90 MHz, DMSO-d_6): δ 3.8 (s, 8H, $NCH_2CO_2C{=}O$), 3.4 (s, 2H, $NC\underline{H}_2CO_2H$), 2.7 (s, 8H, NCH_2CH_2N); IR (KBr): 1820 and 1770 (anhydride C=O), 1635 (carboxylate C=O).

2. Preparation of Octadecanol

Octadecanol was prepared by the reduction of stearic acid via the procedure of Nystrom and Brown.[125] A dry 500 ml three-neck round bottom flask was equipped with a magnetic stir bar, rubber septum inlet, condenser, septum-sealed pressure-

equalizing addition funnel, mercury bubbler and heating mantle. The entire apparatus was flushed with nitrogen to maintain an inert atmosphere. A solution of lithium aluminum hydride (2.85 g, 0.075 mol) in 75 ml anhydrous diethyl ether was added to the flask via a double-ended needle (cannula). A solution of stearic acid (14.225 g, 0.05 mol) in 100 ml anhydrous ether was added dropwise through the addition funnel at a rate sufficient to produce a gentle reflux. Upon completion of the addition, the mixture was heated under reflux for 12 hours and then cooled to room temperature. The excess LAH was decomposed by cautiously adding 3 N NaOH dropwise until gas evolution ceased and then 10% H_2SO_4 was added until a clear two-phase solution resulted. The organic and aqueous layers were separated, the aqueous layer was extracted with two 50 ml portions of ether, the organic layers were combined and the solvent removed under reduced pressure to give crude stearyl alcohol. The product was purified by bulb-to-bulb (Kugelrohr) distillation (bp 195-200 °C/0.2 mmHg) to give 12.22 g (90.5%) of a white waxy solid. The melting point, NMR spectra (^{1}H and ^{13}C) and IR spectrum were in good agreement with previous literature values; mp 59 °C; ^{1}H NMR (90 MHz, $CDCl_3$): δ 3.59 (t, 2H, $C\underline{H_2}OH$), 2.05 (s, 1H, OH), 1.25 (s, 32H, aliphatic CH_2's), 0.88 (t, 3H, CH_3); ^{13}C NMR (90 MHz, $CDCl_3$): δ 62.8 (CH_2OH), 32.9, 32.1, 29.9, 26, 22.8 (aliphatic CH_2's), 14.2 (CH_3); IR (neat): 3250 (br, O-H), 2920 and 2850 (aliphatic CH_2's), 1060 (C-O).

3. Preparation of DTPA Didecylamide (DTPA-DA)

The various DTPA diamide derivatives were prepared via the method employed by Hnatowich and coworkers for the preparation of DTPA-SA.[118] A detailed procedure for the preparation of DTPA-DA is described. A solution of

decylamine (1.0 g, 6.4 mmol) in 100 ml anhydrous chloroform was added to a dry 250 ml three-neck round bottom flask equipped with a condenser, magnetic stir bar, heating mantle, two rubber septa and mercury bubbler while flushing with nitrogen to maintain an inert atmosphere. DTPA dianhydride (2.5 g, 7.0 mmol) was added to the flask under a purge of nitrogen and the mixture was heated under reflux for 24 hours. The insoluble material, which is a mixture of the diamide product and unreacted anhydride, was collected by gravity filtration, washed with $CHCl_3$ and left open to the air to dry. The solid (≈3.4 g) was suspended in 50 ml H_2O and heated under reflux for 30 minutes to hydrolyze the remaining DTPA dianhydride. The insoluble material was collected by a hot vacuum filtration, washed with hot H_2O and dried in a desiccator under vacuum to give 1.85 g (86%) of crude DTPA-DA. The crude product was purified by recrystallization from ethanol. The solid (1.85 g) was suspended in 100 ml EtOH and the mixture was heated to reflux. The resulting hot solution was gravity filtered to remove any insoluble material. The volume of the solution was decreased under reduced pressure until a solid precipitate was first observed. The mixture was reheated until a clear solution formed, allowed to cool to room temperature and then cooled at 0 °C in an ice/water bath to induce further precipitation. The resulting precipitate was collected by vacuum filtration, washed with cold EtOH and dried to give 1.65 g (77%) of a white fluffy solid; mp 174-176 °C; ^{1}H NMR (Figure 21, 200 MHz, py-d_5): δ 8.55 (br t, 2H, NHC=O), 3.86 (s, 8H, terminal $NCH_2C{=}O$), 3.80 (s, 2H, central $NCH_2C{=}O$), 3.53 (m, 4H, $C\underline{H}_2NHC{=}O$), 3.19 (s, 8H, NCH_2CH_2N), 1.68 (m, 4H, $C\underline{H}_2CH_2NHC{=}O$), 1.19 (s, 28H, aliphatic CH_2's), 0.86 (t, 6H, CH_3); ^{13}C NMR (Figure 20, 90 MHz, py-d_5): δ 174.2 (terminal

CO_2H), 173.8 (central CO_2H), 171.1 (NHC=O), 59.8 ($N\underline{C}H_2CONH$), 57.0 (terminal $N\underline{C}H_2CO_2H$), 56.1 (central $N\underline{C}H_2CO_2H$), 53.8 and 53.6 (CH_2N), 39.4 ($\underline{C}H_2NHC=O$), 32.1, 30.2, 29.9, 29.8, 29.7, 27.3, 22.8 (aliphatic CH_2's), 14.0 (CH_3); IR (KBr): 2920 and 2850 (aliphatic CH_2's), 1730 (acid C=O), 1660 (amide C=O), 1635 (carboxylate C=O), 1370 (C-N), 1210; Elemental analysis: Calculated for $C_{34}H_{65}N_5O_8$; %C=60.78, %H=9.75, %N=10.43. Found; %C=60.41, %H=9.77, %N=10.27.

4. Preparation of DTPA Dilaurylamide (DTPA-LA)

DTPA-LA was prepared via the procedure previously described for the preparation of DTPA-DA (refer to pp 112-114) using dodecylamine (1.0 g, 5.4 mmol) and DTPA dianhydride (2.12 g, 5.9 mmol). Recrystallization from ethanol yielded 1.55 g (79%) of a white fluffy solid; mp 182-184 °C; ^{1}H NMR (200 MHz, py-d_5): δ 8.55 (br t, 2H, NHC=O), 3.86 (s, 8H, terminal $NCH_2C=O$), 3.80 (s, 2H, central $NCH_2C=O$), 3.53 (m, 4H, $C\underline{H}_2NHC=O$), 3.19 (s, 8H, NCH_2CH_2N), 1.68 (m, 4H, $C\underline{H}_2CH_2NHC=O$), 1.19 (s, 36H, aliphatic CH_2's), 0.86 (t, 6H, CH_3); ^{13}C NMR (90 MHz, py-d_5): δ 174.2 (terminal CO_2H), 173.8 (central CO_2H), 171.1 (NHC=O), 59.8 ($N\underline{C}H_2CONH$), 57.0 (terminal $N\underline{C}H_2CO_2H$), 56.1 (central $N\underline{C}H_2CO_2H$), 53.8 and 53.6 (CH_2N), 39.4 $\underline{C}H_2NHC=O$), 32.1, 30.2, 29.9, 29.8, 29.7, 27.3, 22.8 (aliphatic CH_2's), 14.0 (CH_3); IR (KBr): 2920 and 2850 (aliphatic CH_2's), 1730 (acid C=O), 1660 (amide C=O), 1635 (carboxylate C=O), 1370 (C-N), 1210; Elemental analysis: Calculated for $C_{38}H_{73}N_5O_8$; %C=62.69, %H=10.11, %N=9.62. Found; %C=62.33, %H=10.18, %N=9.44.

5. Preparation of DTPA Dimyristylamide (DTPA-MA)

DTPA-MA was prepared via the procedure previously described for the preparation of DTPA-DA (refer to pp 112-114) using tetradecylamine (1.0 g, 4.7 mmol) and DTPA dianhydride (1.84 g, 5.2 mmol). Recrystallization from ethanol yielded 1.46 g (79%) of a white fluffy solid; mp 179-182 °C; ^{1}H NMR (200 MHz, py-d_5): δ 8.50 (br t, 2H, NHC=O), 3.84 (s, 10H, $NCH_2C=O$), 3.53 (m, 4H, $C\underline{H}_2NHC=O$), 3.20 (s,8H, NCH_2CH_2N), 1.68 (m, 4H, $C\underline{H}_2CH_2NHC=O$), 1.19 (s, 44H, aliphatic CH_2's), 0.86 (t, 6H, CH_3); ^{13}C NMR (90 MHz, py-d_5): δ 174.1 (terminal CO_2H), 173.9 (central CO_2H), 171.1 (NHC=O), 59.8 ($N\underline{C}H_2CONH$), 56.9 (terminal $N\underline{C}H_2CO_2H$), 56.2 (central $N\underline{C}H_2CO_2H$), 53.8 and 53.6 (CH_2N), 39.4 ($\underline{C}H_2NHC=O$), 32.0, 30.1, 29.9, 29.7, 27.3, 22.9 (aliphatic CH_2's), 14.0 (CH_3); IR (KBr): 2920 and 2850 (aliphatic CH_2's), 1730 (acid C=O), 1660 (amide C=O), 1635 (carboxylate C=O), 1370 (C-N), 1210; Elemental analysis: Calculated for $C_{42}H_{81}N_5O_8$; %C=64.35, %H=10.41, %N=8.93. Found; %C=64.05, %H=10.57, %N=9.12.

6. Preparation of DTPA Dicetylamide (DTPA-CA)

DTPA-CA was prepared via the procedure previously described for the preparation of DTPA-DA (refer to pp 112-114) using hexadecylamine (1.0 g, 4.2 mmol) and DTPA dianhydride (1.63 g, 4.6 mmol). Recrystallization from ethanol yielded 1.42 g (82%) of a white fluffy solid; mp 181-184 °C; ^{1}H NMR (200 MHz, py-d_5): δ 8.52 (br t, 2H, NHC=O), 3.84 (s, 10H, $NCH_2C=O$), 3.53 (m, 4H, $C\underline{H}_2NHC=O$), 3.19 (s, 8H, NCH_2CH_2N), 1.68 (m, 4H, $C\underline{H}_2CH_2NHC=O$), 1.19 (s, 52H, aliphatic CH_2's), 0.86 (t, 6H, CH_3); ^{13}C NMR (90 MHz, py-d_5): δ 174.1

(terminal CO_2H), 173.9 (central CO_2H), 171.1 (NHC=O), 59.8 ($N\underline{C}H_2CONH$), 56.9 (terminal $N\underline{C}H_2CO_2H$), 56.3 (central $N\underline{C}H_2CO_2H$), 53.8 and 53.6 (CH_2N), 39.4 ($\underline{C}H_2NHC=O$), 32.0, 30.2, 29.9, 29.7, 27.2, 22.9 (aliphatic CH_2's), 14.0 (CH_3); IR (KBr): 2920 and 2850 (aliphatic CH_2's), 1730 (acid C=O), 1660 (amide C=O), 1635 (carboxylate C=O), 1370 (C-N), 1210; Elemental analysis: Calculated for $C_{46}H_{89}N_5O_8$; %C=65.76, %H=10.68, %N=8.34. Found; %C=65.38, %H=10.75, %N=8.02.

7. Preparation of DTPA Distearylester (DTPA-SE)

A solution of octadecanol (2.2 g, 8.14 mmol) in 50 ml anhydrous pyridine was added to a dry 100 ml three-neck round bottom flask equipped with a condenser, magnetic stir bar, heating mantle, two rubber septa and mercury bubbler while flushing with nitrogen to maintain an inert atmosphere. DTPA dianhydride (1.32 g, 3.7 mmol) was added to the flask under a purge of nitrogen and the mixture was heated to reflux upon which an amber solution formed. The reaction was monitored using TLC by the disappearance of the anhydride spot (R_F=0.0, 4:2:1 BuOH/AcOH/H_2O) and the appearance of the diester spot (R_F=0.79, 4:2:1 BuOH/AcOH/H_2O). After refluxing for four hours, the solvent was removed under reduced pressure and the remaining solid was subjected to a vacuum of 1 mmHg to remove any residual pyridine. The crude solid was suspended in 50 ml EtOH and stirred vigorously to dissolve the excess octadecanol. The insoluble material was collected by vacuum filtration, washed with EtOH and dried to give 2.36 g (71%) of crude DTPA-SE. The product was purified by recrystallization from dimethylformamide. The solid (2.36 g) was dissolved in 75 ml DMF by heating on

a steam bath. The solution was cooled to room temperature and left standing for 12 hours. The resulting precipitate was collected by vacuum filtration, washed with DMF and dried under a vacuum of 1 mmHg to give 1.97 g (59%) of an off-white powder; mp 194-196 °C; ^{1}H NMR (Figure 23, 200 MHz, py-d_5): δ 4.19 (t, 4H, $CH_2OC=O$), 4.06 (s, 10H, $NCH_2C=O$), 3.34 (s, 8H, NCH_2CH_2N), 1.63 (m, 4H, $C\underline{H}_2CH_2OC=O$), 1.29 (s, 60H, aliphatic CH_2's), 0.88 (t, 6H, CH_3); ^{13}C NMR (Figure 22, 90 MHz, py-d_5): δ 174.0 (CO_2H), 171.8 (CO_2R), 64.6 (CH_2O), 56.3 and 56.0 ($N\underline{C}H_2C=O$), 53.5 and 53.1 (CH_2N), 32.2, 30.0, 29.5, 29.1, 26.4, 22.9 (aliphatic CH_2's), 14.2 (CH_3); IR (Figure 27, KBr): 2920 and 2850 (aliphatic CH_2's), 1735 (acid and ester C=O), 1635 (carboxylate C=O), 1228, 1061; Elemental analysis: Calculated for $C_{50}H_{95}N_3O_{10}$; %C=66.85, %H=10.66, %N=4.68. Found; %C=66.70, %H=10.55, %N=4.40.

8. Preparation of DTPA Distearylthiolester (DTPA-ST)

A solution of octadecanethiol (6.42 g, 22.4 mmol) in 50 ml anhydrous pyridine was added to a dry 100 ml three-neck round bottom flask equipped with a condenser, magnetic stir bar, heating mantle, two rubber septa and mercury bubbler while flushing with nitrogen. DTPA dianhydride (1.0 g, 2.8 mmol) was added to the flask under a purge of nitrogen and the mixture was heated to reflux upon which an amber solution formed. The reaction was monitored using TLC by the disappearance of the anhydride spot (R_F=0.0, 4:2:1 BuOH/AcOH/H_2O) and the appearance of the distearylthiolester spot (R_F=0.82, 4:2:1 BuOH/AcOH/H_2O). After refluxing for four hours, the solvent was removed under reduced pressure and the remaining solid was subjected to a vacuum of 1 mmHg to remove any residual pyridine. The crude solid

was suspended in 50 ml dry dimethoxyethane (monoglyme) and stirred vigorously to dissolve the large excess of octadecanethiol. The insoluble material was collected by vacuum filtration, washed with DME and dried to give 2.38 g (92%) of crude DTPA-ST. The product was purified by recrystallization. The solid (2.38 g) was dissolved in 100 ml DMF by heating in a steam bath. The solution was cooled to room temperature and left standing for eight hours. The resulting precipitate was collected by vacuum filtration, washed with DMF and dried under a vacuum of 1 mmHg to give 1.63 g (63%) of a white powder; mp 179-181 °C; ^{1}H NMR (Figure 26, 200 MHz, py-d_5): δ 4.16 (s, 4H, NCH_2COSR), 4.03 (s, 4H, terminal $NC\underline{H}_2CO_2H$), 3.94 (s, 2H, central $NC\underline{H}_2CO_2H$), 3.38 (s, 8H, NCH_2CH_2N), 2.96 (t, 4H, $CH_2SC=O$), 1.65 (m, 4H, $C\underline{H}_2CH_2SC=O$), 1.28 (s, 60H, aliphatic CH_2's), 0.88 (t, 6H, CH_3); ^{13}C NMR (Figure 25, 90 MHz, py-d_5): δ 201.5 ($RSC=O$), 173.9 (central CO_2H), 173.6 (terminal CO_2H), 65.0 (CH_2S), 56.2 ($N\underline{C}H_2C=O$), 53.9 and 53.5 (CH_2N), 32.0, 30.0, 29.8, 29.4, 28.6, 22.9 (aliphatic CH_2's), 14.2 (CH_3); IR (KBr): 2920 and 2850 (aliphatic CH_2's), 1730 (acid C=O), 1688 (thiolester C=O), 1635 (carboxylate C=O), 1468; Elemental analysis: Calculated for $C_{50}H_{95}N_3O_8S_2$; %C=64.55, %H=10.29, %N=4.52, %S=6.89. Found; %C=64.45, %H=10.58, %N=4.69, %S=7.21.

9. Preparation of Gd-DTPA Dicetylamide Complex (Gd-DTPA-CA)

The various Gd-DTPA diamide complexes were prepared via the method employed by Kabalka and coworkers for the preparation of Gd-DTPA-SA.[116] However, due to the change in solubility resulting from the decrease in alkyl chain length, the isolation procedure was modified for each of the complexes. A detailed

procedure for the preparation of Gd-DTPA-CA is described. DTPA-CA (0.10 g, 0.12 mmol) was suspended in 10 ml EtOH in a 25 ml round bottom flask equipped with a reflux condenser, magnetic stir bar and heating mantle. Upon heating to reflux, a clear solution resulted. A solution of $GdCl_3$ hexahydrate (0.048 g, 0.13 mmol) in 0.5 ml H_2O was added dropwise and the resulting solution was heated at reflux for 30 minutes. The solution was concentrated to ≈3 ml under reduced pressure and then cooled to 0 °C. The resulting precipitate was collected by vacuum filtration, washed thoroughly with H_2O and dried in a desiccator under vacuum to give 0.082 g (69%) of a fine white powder; mp >300 °C; IR (KBr): 2920 and 2850 (aliphatic CH_2's), 1600 (CO_2^-Gd); Elemental analysis: Calculated for $GdC_{46}H_{86}N_5O_8 \cdot 3H_2O$; %C=52.70, %H=8.85. Found; %C=52.50, %H=8.98.

10. Preparation of Gd-DTPA Dimyristylamide Complex (Gd-DTPA-MA)

Gd-DTPA-MA was prepared by the reaction procedure previously described for the preparation of Gd-DTPA-CA (refer to pp 118-119) using DTPA-MA (0.20 g, 0.25 mmol) and $GdCl_3$ hexahydrate (0.10 g, 0.27 mmol). The resulting complex was isolated in a manner identical to that for Gd-DTPA-CA to give 0.096 g (41%) of a fine white powder; mp >300 °C; IR(KBr): 2920 and 2850 (aliphatic CH_2's), 1600 (CO_2^-Gd); Elemental analysis: Calculated for $GdC_{42}H_{78}N_5O_8 \cdot 5H_2O$; %C=49.08, %H=8.62. Found; %C=49.33, %H=8.42.

11. Preparation of Gd-DTPA Dilaurylamide Complex (Gd-DTPA-LA)

Gd-DTPA-LA was prepared by the reaction procedure previously described for the preparation of Gd-DTPA-CA (refer to pp 118-119) using DTPA-LA (0.25 g,

0.34 mmol) and $GdCl_3$ hexahydrate (0.137 g, 0.37 mmol). Following the reaction, the volume of the solution was decreased to ≈2 ml under reduced pressure followed by addition of H_2O until formation of a white solid ceased (≈10 ml). After cooling to 0 °C, the solid was collected by vacuum filtration, washed with cold H_2O and dried in a desiccator under vacuum to give 0.23 g (77%) of a white flaky solid; mp >300 °C; IR(KBr): 2920 and 2850 (aliphatic CH_2's), 1600 (CO_2^-Gd); Elemental analysis: Calculated for $GdC_{38}H_{70}N_5O_8 \cdot 2H_2O$; %C=49.71, %H=8.12. Found; %C=49.47, %H=8.01.

12. Preparation of Gd-DTPA Didecylamide Complex (Gd-DTPA-DA)

Gd-DTPA-DA was prepared by the reaction procedure previously described for the preparation of Gd-DTPA-CA (refer to pp 118-119) using DTPA-DA (0.20 g, 0.30 mmol) and $GdCl_3$ hexahydrate (0.123 g, 0.33 mmol). Following the reaction, all of the solvent was removed under reduced pressure and the remaining solid residue was subjected to a vacuum of 1 mmHg to remove any residual EtOH. The solid was stirred in 5 ml cold H_2O to dissolve the excess $GdCl_3$. The insoluble material was collected by vacuum filtration, washed with cold H_2O and dried in a desiccator under vacuum to give 0.18 g (73%) of a white flaky solid; mp >300 °C; IR (KBr): 2920 and 2850 (aliphatic CH_2's), 1600 (CO_2^-Gd); Elemental analysis: Calculated for $GdC_{34}H_{62}N_5O_8 \cdot 2H_2O$; %C=47.36, %H=7.72. Found; %C=47.06, %H=7.65. The preparation of ^{153}Gd-DTPA-DA was carried out in an identical manner except that a trace amount of $^{153}GdCl_3$ was present in the $GdCl_3$ solution; however, the solvent was removed under reduced pressure by the use of a vacuum pump connected to a

cold finger containing an acetone/dry ice bath as opposed to a rotary evaporator used in the cold experiment.

13. Preparation of Gd-DTPA Distearylester Complex (Gd-DTPA-SE)

A solution of DTPA-SE (0.20 g, 0.22 mmol) in 15 ml pyridine was added to a 25 ml round bottom flask equipped with a magnetic stir bar. A solution of $GdCl_3$ hexahydrate (0.09 g, 0.24 mmol) in 0.5 ml H_2O was added dropwise and the resulting solution was stirred at 25 °C for 30 minutes. The solvent was removed under reduced pressure and the remaining solid residue was subjected to a vacuum of 1 mmHg to remove any residual pyridine. The solid was stirred in 10 ml H_2O to dissolve the excess $GdCl_3$. The insoluble material was collected by vacuum filtration, washed with H_2O and dried in a desiccator under vacuum to give 0.19 g (83%) of a fine off-white powder; mp >300 °C; IR (Figure 28, KBr): 2920 and 2850 (aliphatic CH_2's), 1735 (ester C=O), 1595 (CO_2^-Gd); Elemental analysis: Calculated for $GdC_{50}H_{92}N_3O_{10}\cdot 5H_2O$; %C=52.43, %H=9.24, %N=3.66. Found; %C=52.14, %H=8.98, %N=3.68. The preparation of ^{153}Gd-DTPA-SE was carried out in an identical manner except that a trace amount of $^{153}GdCl_3$ was present in the $GdCl_3$ solution; however, the solvent was removed under reduced pressure by the use of a vacuum pump connected to a cold finger containing an acetone/dry ice bath as opposed to a rotary evaporator used in the cold experiment.

14. Preparation of Gd-DTPA Distearylthiolester Complex (Gd-DTPA-ST)

A solution of DTPA-ST (0.100 g, 0.108 mmol) in 15 ml pyridine was added to a 25 ml round bottom flask equipped with a magnetic stir bar. A solution of

$GdCl_3$ hexahydrate (0.045 g, 0.12 mmol) in 0.5 ml H_2O was added dropwise and the resulting solution was stirred at 25 °C for 30 minutes. The solvent was removed under reduced pressure and the remaining solid residue was subjected to a vacuum of 1 mmHg to remove any residual pyridine. The solid was stirred in 5 ml H_2O to dissolve the excess $GdCl_3$. The insoluble material was collected by vacuum filtration, washed with H_2O and dried in a desiccator under vacuum to give 0.09 g (77%) of a fine white powder; mp >300 °C; IR(KBr): 2920 and 2850 (aliphatic CH_2's), 1690 (thiolester C=O), 1595 (CO_2^-Gd); Elemental analysis: Calculated for $GdC_{50}H_{92}N_3O_8S_2 \cdot 4H_2O$; %C=51.92, %H=8.71, %N=3.63. Found; %C=52.16, %H=8.81; %N=3.40. The preparation of ^{153}Gd-DTPA-ST was carried out in an identical manner except that a trace amount of $^{153}GdCl_3$ was present in the $GdCl_3$ solution; however, the solvent was removed under reduced pressure by the use of a vacuum pump connected to a cold finger containing an acetone/dry ice bath as opposed to a rotary evaporator used in the cold experiment.

C. BIOLOGICAL PROCEDURES

1. Preparation of the Gadolinium-Labeled Liposomes (GLL)

The various GLL agents were prepared via the procedure developed by Kabalka and coworkers for the preparation of the liposomal agent containing 33.3 mol% Gd-DTPA-SA[116] in which an equimolar mixture of egg lecithin, cholesterol and the appropriate Gd-DTPA derivative were used. In a typical experiment, 30 μmol of the appropriate Gd-DTPA derivative was dissolved in a solution of 30 μmol egg lecithin and 30 μmol cholesterol in chloroform. The solvent was removed under

a stream of nitrogen followed by vacuum desiccation for 1 hour. The dried mixture was suspended in 1.0 ml phosphate buffered saline (PBS), pH 7.5, to give a total lipid concentration of 90 μmol/ml. The suspension was sonicated in a bath sonicator for an appropriate time (≈2 hours) to produce small unilamellar vesicles (SUV) having an average diameter of 0.05 μm as verified by negative-stain electron microscopy or by quasi-elastic (dynamic) light scattering. The various radioactive liposomes were prepared via the same procedure by the addition of the appropriate ^{153}Gd-DTPA derivative.

2. Preparation of the Indium(111) - Labeled Liposomes (^{111}ILL)

The various ^{111}ILL agents, which were utilized for the serum stability studies involving complexation of the various DTPA derivatives with indium instead of gadolinium, were prepared via the procedure described above, however, the various ^{111}In-DTPA derivatives were generated in-situ instead of being added as the isolated complex. Typically, an aqueous $InCl_3$ solution containing a trace amount of $^{111}InCl_3$ was added dropwise to a solution of the appropriate DTPA derivative in the appropriate solvent (pyridine for DTPA-SE and DTPA-ST, ethanol for DTPA-SA). In each case, a slight excess of the DTPA derivative was used to avoid the prescence of any uncomplexed metal ion. The solvent was removed under a stream of nitrogen followed by vacuum desiccation. The resulting complex was dissolved in a chloroform solution containing an equimolar amount of egg lecithin and cholesterol. At this point, the previously described procedure was followed.

3. Biodistribution Studies

In the biodistribution studies, normal female Balb/c mice (≈30 g) received 13.5 μmol (150 μl) of the appropriate gadolinium (153)-labeled liposomes (^{153}GLL) via tail vein injection. The mice were sacrificed by cervical dislocation at various time points (15 minutes, 8 hours, 1 day, 2 days, 4 days, 8 days, 12 days). The liver, spleen, blood, lungs, heart and kidney were removed and placed in a gamma counter to measure the percent of radioactivity on a per organ basis. At least three animals were used per time point and the data were averaged. A time course of the biodistribution of the liposomes per organ was then constructed.

4. Serum Stability Studies

In the serum stability studies, gel-filtration of the ^{153}GLL or ^{111}ILL agents was performed using Bio-Gel A 0.5 M (Bio-Rad, Richmond, CA). An equal amount (200 μl) of the appropriate liposomal agent and normal human serum were mixed and incubated at 37 °C at various time intervals (15 minutes, 1 hour, 5 hours, 24 hours). An aliquot (200 μl) of the serum-liposome mixture was placed on the Bio-Gel column (7 ml) and eluted with PBS (pH 7.5). Three drop fractions were collected and each fraction was placed in a gamma counter to measure the amount of radioactivity. A plot of activity versus fraction number was constructed. An elution profile of the various radioactive liposomal agents was also performed prior to mixing and incubation in the serum to determine the stability of the paramagnetic amphiphile under the liposomal preparation conditions.

5. Magnetic Resonance Imaging Studies

In the MRI studies, female Balb/c mice were anesthetized with an intraperitoneal injection of Ketamin prior to intravenous injection of the appropriate amount of the appropriate GLL agent. The mice were restrained on a wooden board in a prone position and placed in the receiver coil. Coronal images (3-4 mm slice thickness) were obtained on each mouse prior to and within one hour after injection of the various GLL agents under T_1-weighted conditions (short TR, short TE).

PART II: THE APPLICATION OF BORON-11 SPECTROSCOPY AND IMAGING FOR THE DETECTION AND LOCALIZATION OF A BNCT AGENT IN-VIVO

CHAPTER V

MULTINUCLEAR MR SPECTROSCOPY AND IMAGING IN-VIVO

A. INTRODUCTION

Multinuclear magnetic resonance (i.e. NMR of elements other than hydrogen) has become a valuable tool for scientists of various disciplines due to advancements in instrumentation and Fourier transform techniques. A prime example is the application of ^{13}C NMR spectroscopy to structure determination in organic chemistry. ^{31}P NMR spectroscopy has emerged in biochemistry as a tool to study the metabolism of living cells and extracted tissues. More recently, there has been intense interest in the development of in-vivo multinuclear magnetic resonance imaging (MRI) and spectroscopy (MRS). MRI and MRS hold promise for future clinical evaluation of various disorders by utilizing elements other than hydrogen. Several magnetically active isotopes have potential in clinical practice; they are listed, along with their NMR properties, in Table 4. In the following section, isotopes which have been used in in-vivo MRI and MRS will be discussed.

B. BACKGROUND

1. Phosphorus-31 (^{31}P)

With the exception of the proton, phosphorus is the most promising isotope for in-vivo NMR studies. This isotope is very similar to the proton in that it has a

Table 4: NMR Properties of Various Nuclei

Isotope	Spin Number	Frequency at 2.0 T	Relative Sensitivity
^{1}H	1/2	85.155	1.00
^{31}P	1/2	34.472	0.0663
^{23}Na	3/2	22.500	0.0925
^{13}C	1/2	21.410	1.76×10^{-4}
^{19}F	1/2	80.100	0.8328
^{11}B	3/2	27.320	0.133
^{10}B	3	9.150	3.89×10^{-3}

spin number of 1/2 and is 100% abundant.[18] However, there are certain drawbacks associated with ^{31}P when compared to hydrogen. First, its inherent sensitivity toward NMR is more than one order of magnitude lower than that of the proton (Table 4). Second, while protons are present at tissue concentrations of about 55 M, ^{31}P typically exists in tissues at concentrations on the order of 10 mM.[135] However, with the utilization of increased scan times as well as modified pulse sequences and improved receiver coils, acceptable results can be obtained.

During the past decade, magnetic resonance spectroscopy (MRS) has been developed to noninvasively measure various metabolites in living tissue.[136-138] ^{31}P MRS has been utilized to measure the various phosphates involved with energy metabolism. It has been repeatedly demonstrated that ^{31}P MRS rapidly detects metabolic changes produced by tissue anoxia or ischemia in experimental models of stroke and myocardial infarction. The ^{31}P NMR spectra of animal tumors are often abnormal and cancer treatment frequently produces metabolic changes that precede alterations of tumor size. Early clinical results have shown that ischemia, malignancy and cancer treatment also produce metabolic alterations in human tissues. The metabolic information derived from MRS is obtained because the resonance frequency of the different populations of nuclei is affected by their molecular environment. The success of ^{31}P MRS in-vivo is due to the broad chemical shift range of the various phosphate metabolites ($\approx$30 ppm).[135] These experiments are typically conducted with the utilization of surface coils in order to provide localization as well as improved sensitivity.[139-142]

In order to interpret the metabolic information obtained from ^{31}P MRS, one must understand the metabolic process that is involved. The major pathways of energy metabolism that occur in all cells of the body are depicted in Figure 35.[136,143] There are two major pathways by which the oxidation of foods yields adenosine triphosphate (ATP): glycolysis and the citric acid cycle. In the absence of oxygen, glucose is oxidized into lactic acid leading to the generation of ATP via the glycolysis pathway. In the presence of oxygen, the citric acid cycle generates ATP by the process of oxidative phosphorylation. Once produced, ATP is used for biological work driven by the breakdown of its high energy phosphate bonds via hydrolysis to produce adenosine diphosphate (ADP) and inorganic phosphate (Pi). In the presence of oxygen, ADP and Pi are resynthesized to form ATP. The enzyme creatine kinase (CK) generates the storage form of high-energy phosphate bonds, phosphocreatine (PCr). When sufficient oxygen and fuels are available to facilitate ATP synthesis, abundant amounts of PCr are produced. If ATP synthesis is inhibited by hypoxia, ischemia or cell damage, PCr serves to maintain ATP levels so that cellular work can continue. However, if PCr stores are depleted and ATP is not resynthesized, ATP concentrations will fall to a point at which biological work can no longer occur.

The various metabolites which are detected using ^{31}P MRS of intact tissues are illustrated in the spectrum shown in Figure 36 which was obtained from intact frog gastrocnemius muscle.[144] On the right are the peaks for the three phosphates of ATP; α, β and γ. The α- and β-phosphates of ADP overlap with the α- and γ-phosphates of ATP; however, because ADP concentrations are kept so low in healthy

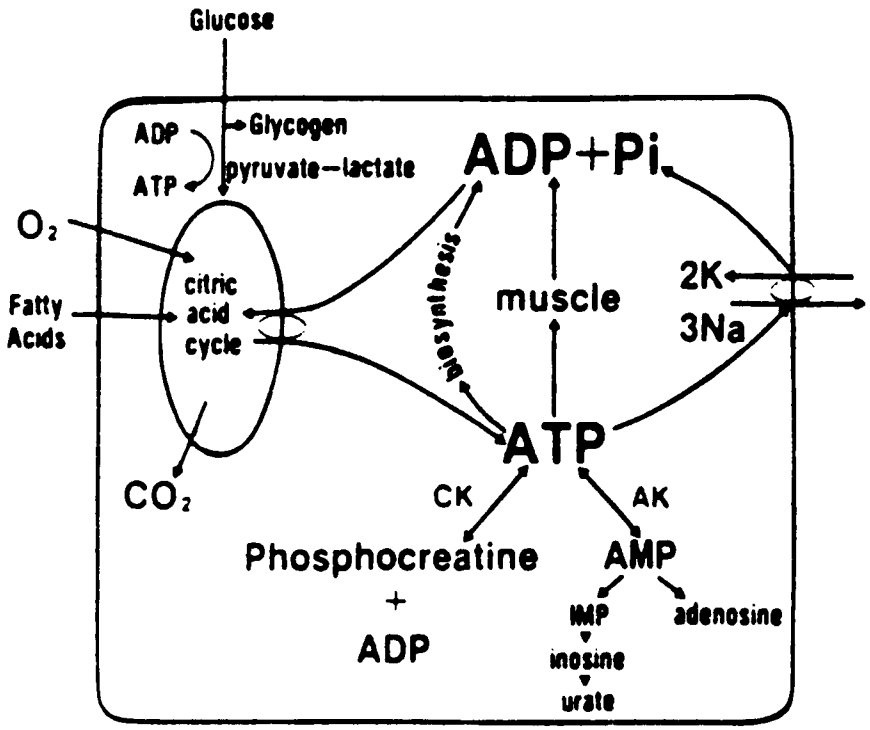

Figure 35. Major pathways of energy metabolism.

tissue, it is not detectable. The β peak of ATP is frequently used to assess ATP concentration because no other peaks overlap with it. The peak for PCr is to the left of γ-ATP. To the left of PCr is the Pi peak which represents the sum of monobasic and dibasic inorganic phosphate, which are in rapid exchange. The chemical shift of the peak represents a weighted mean of the two species. Changes in pH alter the balance between the species, thus producing a change in the chemical shift of the Pi peak. Acidosis shifts the peak to the right, whereas alkalosis causes a shift toward the left. Changes in the chemical shift of Pi, usually referenced to PCr, can be used to noninvasively estimate intracellular pH. A comparison with pH measured by other techniques demonstrates that ^{31}P MRS is a valid approach to determine pH.[145]

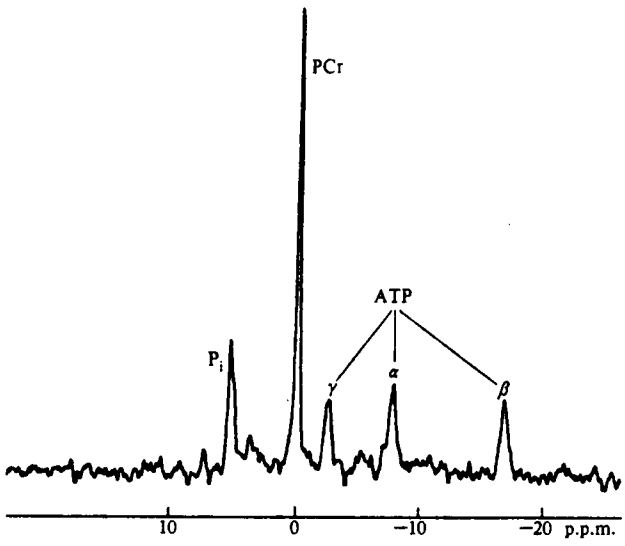

Figure 36. ^{31}P spectrum of frog gastrocnemius muscle.

Under conditions where insufficient oxygen is provided to the cell (anoxia, ischemia), the breakdown of ATP for cell work exceeds the production of ATP by

oxidative phosphorylation. This produces a rise of ADP, which stimulates glycolysis and accelerates lactate formation. If CK and PCr are present, PCr hydrolysis will maintain ATP concentrations. However, when PCr is exhausted, ATP will begin to fall. Hydrolysis of PCr and ATP will produce increased concentrations of Pi. In summary, anoxia, ischemia or tissue damage will produce breakdown of high-energy phosphates (PCr and ATP), a rise in Pi and an increase in lactic acid production leading to a decrease in pH. Restoration of tissue oxygen leads to a reversal of these processes. Lactate concentrations fall and pH returns to normal. ATP and PCr concentrations rise while inorganic phosphate falls. These events can be monitored noninvasively with ^{31}P MRS, as illustrated in the spectra shown in Figure 37, which were obtained from the leg of an anesthetized rat.[142] Figure 37a shows a spectrum obtained from muscle below the knee under normal conditions. Figure 37b shows a spectrum obtained from the same location after a tight tourniquet had been placed around the leg just above the knee. There are dramatic differences between the two spectra; in the spectrum for ischemic muscle there is no PCr, reduced amounts of ATP and a large concentration of Pi. Furthermore, the shift of the Pi peak towards the right indicates that the pH has decreased. Figure 37c shows a spectrum obtained from the same area following removal of the tourniquet. The similarity in this spectrum with the one shown in Figure 37a indicates that the muscle has recovered from ischemia. Similar studies conducted on human limbs have proven to be of considerable value in investigating the biochemistry of healthy and diseased human muscle.[146-149]

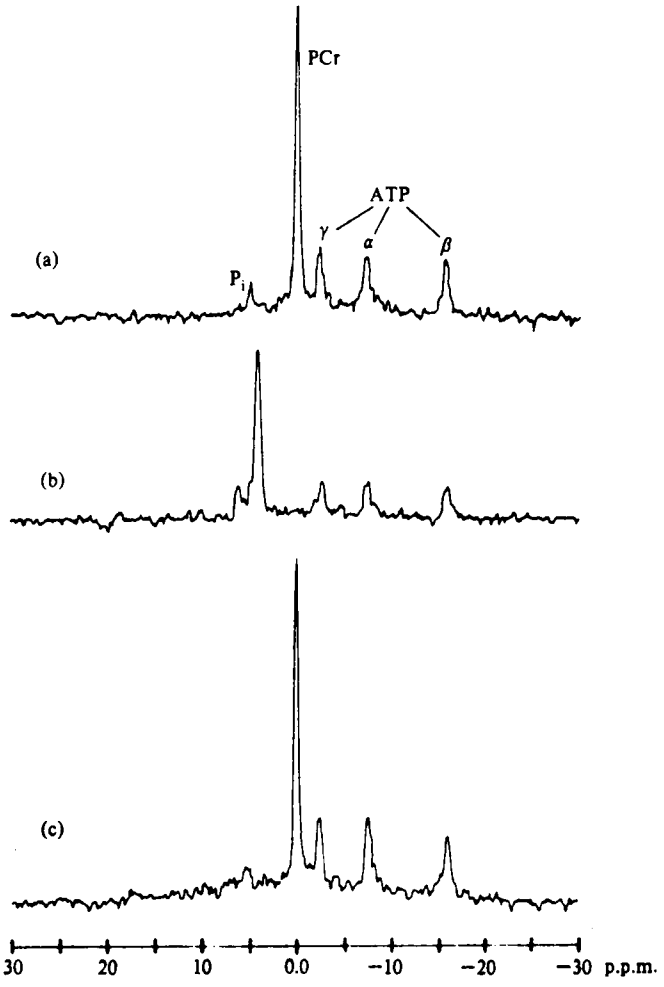

Figure 37. ^{31}P spectra obtained from leg muscle (a) under normal conditions, (b) under ischemic conditions and (c) following recovery from ischemia.

In addition to muscle, numerous studies have been conducted utilizing ^{31}P MRS to investigate high energy phosphate metabolism in various organs and tissues.[136,143,150] Initial experiments revealed that ^{31}P MRS signals could be obtained from perfused animal hearts.[151-154] The resulting spectra were similar to those obtained from muscle except that the PCr is decreased compared to Pi and ATP because the heart is rapidly contracting, resulting in a lower steady-state PCr/ATP ratio than resting skeletal muscle. Hypoxia or total cardiac ischemia produced depletion of PCr and ATP accompanied by tissue acidosis.[155,156] More recently, ^{31}P NMR spectra have been obtained from animal hearts in-vivo in experiments using open chested animals,[157] implanted receiver coils,[158] catheter coils placed in cardiac ventricles[159] and surface coils placed on intact animal chests.[160] Similar experiments have not been performed on human subjects. However, metabolic disturbances produced by various models of human heart disease[161,162] and the effects of therapeutic modalities[163,164] have been investigated. ^{31}P MRS has been utilized for the non-invasive investigation of brain metabolism.[165-167] Spectra obtained from the brain exhibit a PCr/ATP ratio considerably lower than that of resting muscle which suggests the continued electric activity of the brain produces a lower steady-state PCr/ATP ratio. Experiments involving induced anoxia and ischemia caused a fall of PCr, a rise of Pi and tissue acidosis.[168,169] Most brain studies have been performed utilizing surface coils. ^{31}P NMR techniques have been used to study metabolism in various other organs such as the liver[170,171] and kidney.[172,173] The technique has also been utilized as a non-invasive method in the study of cancer.[174-176] The spectra obtained from animal tumors are variable depending on the type

and size of tumor and often appear different from those obtained from normal organs. A potential clinical application has been demonstrated by reports that cancer therapy produces metabolic alterations of tumors before anatomical regression of the tumor can be measured.[177,178] These observations in animals have provided a strong impetus for the further development of ^{31}P MRS so that similar measurements may be performed on patients.

In addition to spectroscopy, phosphorous-31 has been utilized for magnetic resonance imaging. Due to the large chemical shift range of the high-energy phosphates, this isotope is a prime candidate for chemical shift imaging. A number of factors make in-vivo ^{31}P MRI challenging. The T_2 relaxation times of the phosphorous peaks are quite short (5-20 ms), placing demands on the rapidity in which data are collected following excitation. In addition, the lower concentrations as well as decreased sensitivity of ^{31}P as compared to the proton cause the overall signal obtained from naturally occurring ^{31}P to be reduced by greater than 10,000 times compared to protons. To combat these problems, high field strength magnets are required (> 1.5 T), large voxels (poor spatial resolution) must be used to increase the signal and pulse sequences must be modified to compensate for the short relaxation times. Using these strategies, ^{31}P chemical shift images with imaging times of 4 hours have been acquired from both normal and infarcted cat brains as well as human legs.[179] These studies imaged the large PCr peaks in normal tissue and demonstrated changes under ischemic conditions. Although still quite primitive, these results represent a significant achievement. For studies of this kind to be clinically useful, imaging times will need to be reduced considerably.

2. Sodium-23 (^{23}Na)

The cellular composition of sodium and its concentration gradient across the cell membrane play an important role in various physiological processes. Under normal conditions, sodium is eight to ten times more concentrated in the extracellular space than within the cell. The sodium pump in the cell membrane maintains this gradient. Excess accumulation of sodium inside the cell is implicated in various diseases including cancer,[180] diabetes[181] and hypertension.[182] As illustrated in previous studies, the non-invasive nature of MRS and MRI is ideally suited for the study of these processes.[183-185]

Sodium-23 is similar to phosphorous in that it is 100% naturally abundant,[18] has a NMR sensitivity approximately one order of magnitude less than the proton (Table 4) and is present in the human body at much lower concentrations than the proton (45 mM).[135] ^{23}Na differs from ^{1}H and ^{31}P in one important respect. It has a nuclear spin of I=3/2 and, therefore, possesses a nuclear quadrupole moment.[18] The quadrupole moment interacts with electric field gradients produced by the asymmetric distribution of dipoles surrounding the nuclei resulting in a net quadrupole interaction.[186] In the presence of a magnetic field, a nucleus with a spin number of 3/2 has four energy levels, as illustrated in the quantum mechanical description shown in Figure 38. Each energy level differs from the others only in their spin quantum number, m, and transitions are allowed between two energy levels only if they differ in their m values by unity. Therefore, only three transitions are expected and since the energy separation between adjacent levels is the same,

the three occur at the same frequency resulting in a single NMR line as illustrated in Figure 38a.

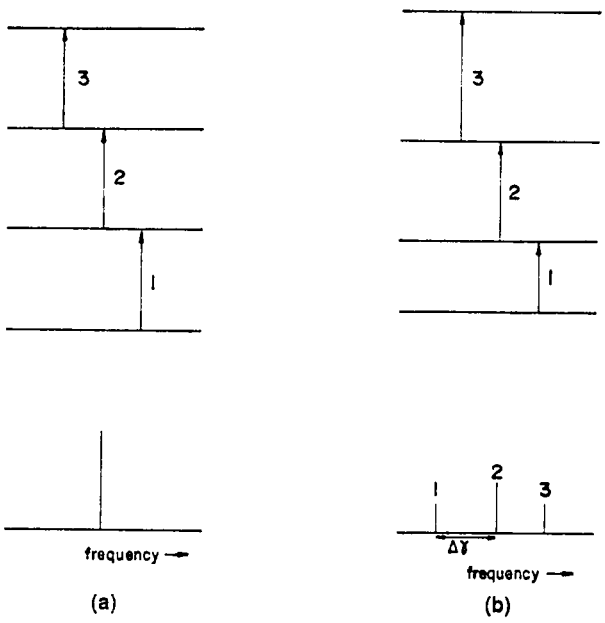

Figure 38. Energy levels of an I=3/2 nucleus in a magnetic field (a) without quadrupole coupling and (b) with quadrupole coupling.

However, in the presence of a quadrupole interaction, the energy levels are modified. The quadrupole interaction depends upon the symmetry of the dipoles around the nucleus and the orientation of the symmetry axis relative to the external magnetic field. If an axial symmetry is assumed with its axis oriented at an angle, θ, relative to B_o, the energies of the four levels are given by the following equation:

$$E(m) = E(m,o) + (1/16)e^2qQ(4m^2-5)(3\cos^2\theta-1) \qquad (20)$$

where E(m,o) is the Zeeman energy for level m, eq is the elective field gradient, eQ is the quadrupole moment and e is the charge. The energy level diagram in which the molecular axis is parallel to B_o ($\theta = 0$) is shown in Figure 38b which illustrates the

three transitions occur at three different frequencies resulting in observation of three separate NMR peaks. Equation 20 shows that the frequency of the center peak (2), which results from the transition from m=1/2 to m=-1/2, is not affected by quadrupole interactions. However, transitions 1 and 3, whose energies are determined by the strength of the quadrupole interaction, are displaced on either side of the center peak by $\Delta\gamma = \pm(1/2)e^2qQ$. Quantum mechanical calculations show that the center peak accounts for 40% of the total intensity while each of the outer lines contains 30%.[187]

As illustrated in equation 20, the transition energies due to quadrupole interaction depend on the orientation of the molecular symmetry axis relative to the external magnetic field. While the position of the center peak is independent of molecular orientation, the positions of the outer peaks relative to the center peak vary with orientation. The positions of the outer peaks are distributed over a frequency range and since the area under the outer peaks is constant, this causes a reduction in their peak heights. Heterogeneity in the molecular environment produces a variation in the quadrupole interaction, which further broadens the outer peaks. The combination of these two effects broadens the outer peaks beyond detection so that only 40% of the total sodium concentration contributes to the observed NMR signal. This phenomenon is known as heterogenous line broadening.

In addition, molecular motions cause fluctuations in the electric field gradient which affects the relaxation times of the transitions associated with the outer peaks. In fact, the relaxation times are so shortened as to broaden the lines beyond detection, resulting in a loss of 60% of the total signal intensity. This phenomenon

is known as homogenous line broadening. In the initial ^{23}Na NMR experiments conducted on various animal tissues, it was observed that the detected signal accounted for only about 30-40% of the total sodium content in these tissues.[188-190] This observation was later attributed to quadrupole interactions in which the observed signal from the center transition accounts for 40% of the expected intensity and the remaining 60% from the outer transitions is lost due to line broadening. The broadening probably arises from homogenous and heterogeneous mechanisms. The relaxation behavior of I=3/2 systems is discussed in great detail by Hubbard[191] and Bull[192] but, in summary, both the T_1 and T_2 relaxation rates of the nuclei are very short as compared to those in I=1/2 systems as a result of quadrupole interactions.

Sodium-23 is not a nucleus of choice for spectroscopy. Sodium ions generally exist in the form of aquo complexes both inside and outside the cell; therefore, they exhibit very small chemical shift differences (i.e. similar resonance frequencies). This problem is further aggravated by the fact that one is more interested in the behavior of the intracellular ions whose concentrations are small as compared to the uninteresting extracellular ions. Most ^{23}Na MRS studies have focused on the separation of resonance frequencies of the intracellular and extracellular ions. This has been accomplished by the use of paramagnetic shift reagents. The shift reagents selectively induce a hyperfine frequency shift in the resonance frequency of the extracellular nuclei resulting in two separate peaks, as shown below. Studies indicate that shift reagents consisting of lanthanide ions chelated with anionic complexes possess the most desirable properties.[193,194] The commonly used lanthanide ions are

Dy^{+3} and Tm^{+3} and the more popular chelates are PPP^{-5} (tripolyphosphate) and $TTHA^{-6}$ (triethylene tetraminehexaacetic acid).[195] These reagents have been used to determine the intracellular sodium ion concentrations and transmembrane transport in cell suspensions.[194, 196-198] They have also been used to study intact tissues however this situation is much more complex than that encountered with cell suspensions.[194, 199-201] To date, only two reports have appeared dealing with the utilization of ^{23}Na MRS in in-vivo animal studies.[202,203]

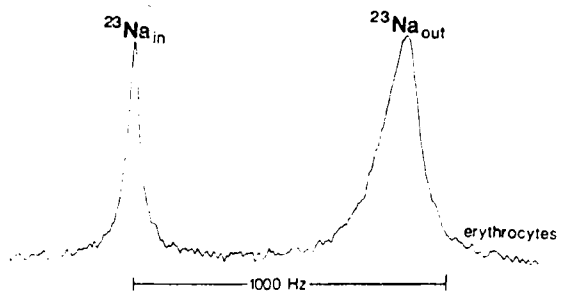

Due to its short T_1 relaxation time, ^{23}Na has become a prime candidate for multinucleur MR imaging because higher sensitivity per unit time can be achieved by decreasing the repetition time (TR).[204] However, due to the low sensitivity of ^{23}Na, the images do not provide anatomical details to the same extent as proton images. The low sensitivity can be somewhat improved by the use of higher field magnets (2.0 T or greater). Clinical sodium images depend on both the spin-density and the T_2 characteristics of sodium in-vivo. In a spin density image, the contrast between different tissues depends on the differences in signal intensities produced by the ^{23}Na nuclei in each tissue type (i.e. differences in ^{23}Na concentration). The ^{23}Na concentration in extracellular spaces is 0.15 M as compared to 0.012-0.02 M

in intracellular spaces. In addition, the ^{23}Na concentration in malignant tumors increases as much as 400% above normal ^{23}Na concentration[205] which has provided the ability to grade neoplasms and detect tumor recurrence. A growing body of evidence suggests that the average T_2 relaxation rate of extracellular ^{23}Na is longer than that of intracellular ^{23}Na.[206,207] In addition, the T_2 decay rate appears to be even longer in abnormal conditions, which is attributed to the expansion of the extracellular space. Since the difference between the intracellular and extracellular T_2 becomes larger with disease, the separation of the two compartments is facilitated. Due to the very short T_2 values of ^{23}Na nuclei in general, gradient-echo protocols are typically used in clinical imaging.[208]

In ^{23}Na images of normal brain, the cerebrospinal fluid and chambers of the eye exhibit a high signal intensity, whereas the actual brain parenchyma produces a signal of lower intensity resulting in good contrast between the brain and ventricles. Contrast between normal brain and lesions is demonstrated in longer TE images due to the increased ^{23}Na content as well as the prolonged T_2 of the ^{23}Na signal in the lesion as compared to normal brain. As a result, ^{23}Na MRI has proven to be useful for the characterization of brain tumors and the detection of lower grade lesions.[208,209] Experimental work has shown that intracellular ^{23}Na increases by 400% in highly malignant tumors while it increases by 150% in lower grade neoplasms. ^{23}Na imaging has also been used to monitor the changes in ^{23}Na concentration associated with cerebral infarctions and strokes.[210,211] Preliminary experiments suggest that similar applications may exist outside the central nervous system.[212,213]

3. Other Elements

In addition to ^{31}P and ^{23}Na, several other elements have been used for MR studies in-vivo. The natural abundance of carbon-13 nuclei (spin 1/2) is only 1.1 percent[18] and this isotope has a sensitivity toward NMR that is approximately four orders of magnitude below the proton (Table 4); therefore, only certain storage compounds with very high intracellular concentrations (triacylglycerols, glycogen) are detectable at the natural abundance level by ^{13}C NMR in-vivo. However, the low natural abundance of ^{13}C in-vivo has proved to be advantageous for metabolic studies by the use of a ^{13}C label introduced by specifically labeled substrates.[214,215] The ^{13}C-enriched substrates are metabolized in the living cell and the resulting signals from intermediates and end-products are used to elucidate pathways and kinetics. This technique has shown considerable promise for investigating various aspects of intermediary metabolism as well as various metabolic disorders such as diabetes mellitus. Fluorine-19 (spin 1/2) has also been used for MR studies in-vivo. Although ^{19}F is 100% naturally abundant[18] and has an NMR sensitivity only slightly less than the proton (Table 4), this isotope has an extremely low biological occurrence and, therefore, the signal cannot be detected at natural levels. However, various fluorine-labeled substrates have been utilized to investigate metabolic mechanisms in-vivo.[216] A prime example is the use of fluorodeoxyglucose for MRS investigations of brain and myocardial metabolism.[217] The use of other non-traditional nuclei, such as boron, aluminum or nitrogen, also hold promise for MRI applications in medicine. For example, ^{27}Al NMR could be used to study Alzheimer's disease.

C. STATEMENT OF THE PROBLEM

Boron neutron capture therapy (BNCT) depends on the successful delivery of agents enriched with the boron-10 isotope to a targeted organ or lesion.[218] A current problem associated with BNCT is the inability to verify, localize and quantitate ^{10}B content in-vivo. Presently, no method is available to assess BNCT agents in a non-invasive manner; current boron detection methodologies such as neutron- capture radiography and emmission spectroscopy require the use of excised tissue.[219-221] Therefore, the development of a non-invasive method for measuring boron distribution in-vivo would expedite BNCT investigations.

Magnetic resonance spectroscopy (MRS) and imaging (MRI) are potentially valuable techniques for the evaluation of BNCT agents in-vivo since both isotopes of boron are magnetically active (Table 4). The purpose of the research project presented in Part II was to develop magnetic resonance techniques for the detection and localization of a representative BNCT agent in solution as well as in animal tissue. The results of these endeavors, from both a spectroscopic and imaging standpoint, as well as the problems encountered when attempting to achieve these purposes will be discussed.

CHAPTER VI

RESULTS AND DISCUSSION

A. INTRODUCTION

Boron neutron capture therapy (BNCT) is brachyradiotherapy by heavy charged particles which involves activation of the ^{10}B isotope by a neutron source as illustrated in equation 21.[222]

$$^{10}B_5 + {}^{1}n_0 \rightarrow {}^{7}Li_3 + {}^{4}\alpha_2 \qquad (21)$$

^{10}B has the unique property of absorbing thermal (low-energy) neutrons resulting in fission of the ^{10}B nucleus to produce a 1.47 MeV alpha particle and a 0.84 MeV lithium atom.[223] This property makes ^{10}B very attractive for neutron capture therapy because the low-energy reactants are converted to the cytotoxic fission products directly within the cancerous cell, therefore, providing treatment to the infected area.

The clinical success of BNCT depends upon a variety of factors. First, a neutron flux of sufficient energy to achieve the prerequisite nuclear reaction while minimizing damage to healthy tissue is required. Early BNCT clinical trials failed to meet this goal and were unsuccessful.[224,225] Recently, systems have been developed which are capable of supplying epithermal neutron beams possessing broadband energies of 1.0 eV to 10 KeV which are sufficient to achieve neutron capture by ^{10}B with minimal damage to normal tissue.[226,227] Second, the delivery of a sufficient quantity of ^{10}B to the targeted lesion at therapeutic BNCT levels ($\geq$10 ppm ^{10}B) is required. In addition, a ratio of lesion/healthy tissue concentration

greater than three is imperative to avoid adverse effects in normal tissue. Several boron-rich agents have been developed which selectively accumulate in tumor cells (melanomas, glioblastomas). A prime example is a sodium mercaptoundecahydro-dodecaborate dimer (BSSB), $Na_4B_{24}H_{22}S_2$, 16.[228,229] The circles in the polyhedra structure represent boron atoms with hydrogen atoms attached except where sulfur is a substituent. BSSB is known to localize in glioblastomas, a particularly destructive brain tumor. This agent has shown success in clinical trials in Japan in which its use in BNCT has prolonged the lives of brain tumor patients by an average of six months and is currently being considered for clinical trials in the USA. These pioneering studies have spurred the development of new boron-enriched compounds including porphyrin and amino acid derivatives.[223,230,231]

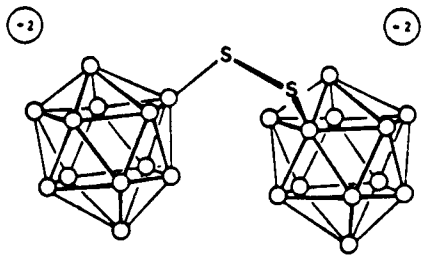

16

Boron is not naturally occurring in living systems, therefore, boron MR spectroscopy and imaging appear to be ideal methods for the detection and localization of BNCT agents in-vivo. For example, MR could be used to monitor the course of distribution of a BNCT agent and help predict the optimum time for neutron irradiation.[232] In addition, it could be used to determine the concentration of boron prior to and following neutron irradiation in an effort to monitor therapy

results. Finally, this technique would aid in the development of new, more effective BNCT agents.

Both isotopes of boron, ^{10}B and ^{11}B, are magnetically active with spin numbers of 3 and 3/2, respectively (Table 4). Boron-11 is more commonly used in NMR spectroscopy because it has a higher natural abundance than boron-10 (80.42% versus 19.58%).[18] ^{11}B NMR is used routinely as an analytical tool in organoborane chemistry. Typical T_1 and T_2 values for ^{11}B are in the range of 10 to 200 ms and are dominated by quadrupolar effects.[18] Boron-hydrogen coupling constants (J values) are between 100 and 190 Hz.[18] Based upon their identical spin numbers, one would expect the in-vivo behavior of ^{11}B to be similar to that of ^{23}Na.

The imaging and spectroscopy experiments to be presented in this chapter were performed utilizing ^{11}B because it has a sensitivity towards NMR approximately two orders of magnitude greater than that of ^{10}B (Table 4). However, its sensitivity is approximately one order of magnitude less than that of the proton. Therefore, dedicated RF coils tuned to the ^{11}B frequency were designed to perform the experiments. Since BNCT agents are not 100% enriched with ^{10}B, there is always a small amount of ^{11}B present (5-25%). In addition, the information gained from these experiments will be used to develop future experiments utilizing ^{10}B. The spectroscopy and imaging results of a BNCT agent in solution as well as in animal tissue will be discussed in the following sections. All of the experiments were performed on a whole-body MR imaging unit having multinuclear capabilities.

B. INITIAL SPECTROSCOPY AND IMAGING EXPERIMENTS

1. $NaBPh_4$ Phantom Studies

The first experiments were performed on an aqueous 0.20 M sodium tetraphenylborate solution (1.7 mg/ml ^{11}B) to check the ability of the instrument to operate at the ^{11}B frequency. The instrument operated at an external magnetic field strength of 1.9 T, which corresponds to a ^{11}B frequency of 25.996 MHz. The ^{11}B NMR spectrum obtained from the phantom using a saturation recovery protocol is illustrated in Figure 39. The spectrum is displayed with the application of zero-order phase correction and a 5 Hz exponential line broadening filter resulting in a S/N ratio of 25. The natural linewidth of the signal, $\Delta f_{1/2}$, is 21 Hz, which corresponds to a T_2^* of approximately 15 ms (equation 6). This relatively narrow linewidth (i.e. long relaxation time) as compared to the values to be reported in later experiments is indicative of quadrupolar nuclei possessing a symmetrical dipole environment (i.e. no quadrupole interaction).

Following the successful detection of the ^{11}B signal, the next step was to perform an imaging experiment on the $NaBPh_4$ phantom. The first ^{11}B MR image[233], obtained utilizing a three-dimensional gradient-echo protocol (refer to pp 29-32), is illustrated in Figure 40. The phantom was oriented in the magnet with the long axis of the bottle aligned along the y direction (refer to Figure 13). The image is displayed as a 10 mm coronal slice with the phase encoding axis (x axis) appearing along the horizontal direction and the frequency encoding axis (z axis) appearing along the vertical direction. The second phase encoding axis which corresponds to

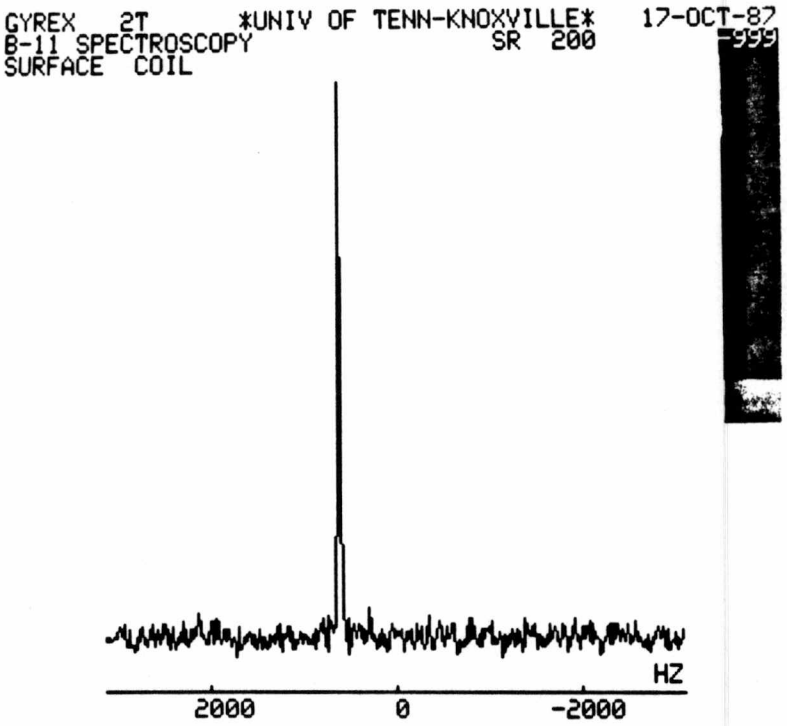

Figure 39. ^{11}B MR spectrum of a 0.2 M $NaBPh_4$ phantom.

Figure 40. ^{11}B MR image of a 0.2 M $NaBPh_4$ phantom obtained using a three-dimensional gradient echo protocol.

the slice direction (y axis), is oriented perpendicular to the page. The image has a S/N ratio of 8 and an in-plane resolution of 0.49 cm along both the horizonal and vertical directions (0.24 cm^2 pixel size, 0.24 cc voxel size). This result indicated that the instrument had the capability of imaging boron at relatively high concentrations using standard imaging protocols.

2. BSSB Phantom Studies

The next set of experiments were performed on aqueous solutions (concentrated and dilute) containing the dimeric sodium mercaptoundecahydrodo-decaborate BNCT agent, 16. The initial experiments were performed on a 0.10 M BSSB solution (natural abundance levels of boron, 0.86 mg/ml ^{11}B). The ^{11}B NMR spectrum obtained using a saturation recovery pulse sequence is presented in Figure 41. The spectrum is displayed with zero-order phase correction and 5 Hz line broadening resulting in a S/N ratio of 43. The large signal appearing at 350 Hz is assigned to the 22 boron atoms bonded to hydrogen and the smaller signal appearing at 650 Hz is assigned to the two remaining boron atoms bonded to sulfur. The large signal appears as a doublet due to a boron-hydrogen coupling interaction (J = 145 Hz). Subsequent experiments performed on a high-resolution NMR spectrometer under decoupled conditions confirmed the presence of the coupling interaction in which the doublet signal collapsed to give a single peak. The increased linewidths (i.e. decreased T_2^* relaxation times) of the various signals as compared to that exhibited by $NaBPh_4$ is indicative of a quadrupolar interaction resulting from a asymmetric distribution of dipoles surrounding the various boron nuclei. Imaging

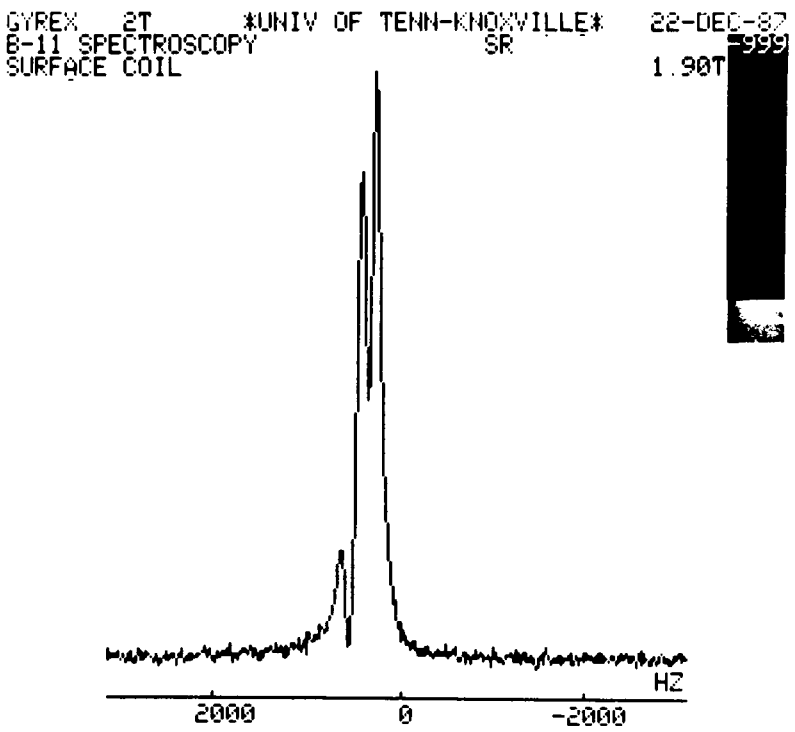

Figure 41. ^{11}B MR spectrum of a 0.1 M BSSB phantom.

experiments were performed on the 0.10 M BSSB phantom using similar conditions as for the $NaBPh_4$ imaging to give good results.

Spectroscopy and imaging experiments were then performed on dilute solutions containing the dimeric BNCT agent (0.01 M BSSB) in which the ^{11}B concentration approximated a therapeutic dose (86 μg/ml).[229] The volume of the dilute solutions was 15 ml in an effort to approximate the volume in which the agent was found in later animal experiments (liver, tumors). In the ^{11}B NMR spectroscopy experiments, an interesting phenomenum was noted when the solutions were contained in glass vials as compared to plastic vials. This is illustrated in the spectra presented in Figure 42. The spectrum presented in Figure 42a was obtained from the 0.010 M BSSB solution contained in a plastic vial using a saturation recovery protocol. The spectrum is displayed with zero-order phase correction and 5 Hz line broadening resulting in a S/N ratio of 8.7. The spectrum is similar to that obtained from the concentrated BSSB phantom; however, the smaller signal becomes lost in the noise level. This result indicated that the sensitivity limits required for detecting the ^{11}B signal at the low boron concentrations present in the animal was available.

The spectrum shown in Figure 42b was obtained under similar conditions as for the above experiment; however, the 0.010 M BSSB solution was contained in a glass vial. This spectrum reveals the presence of a very broad signal ($\Delta f_{1/2} = 1415$Hz) in addition to the expected doublet signal; both signals appear at similar frequencies. The broad peak is attributed to a ^{11}B signal emitted from the borosilicate present in the glass. Peaks possessing very large linewidths (i.e. short T_2 relaxation times)

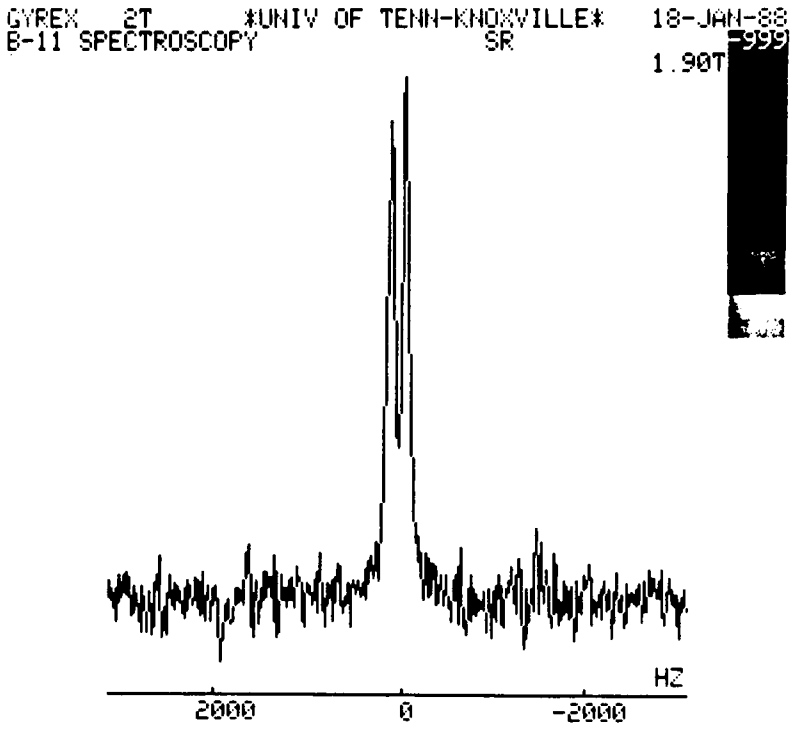

(a)

Figure 42. ^{11}B MR spectra of a 0.01 M BSSB phantom contained in (a) plastic vial and (b) glass vial.

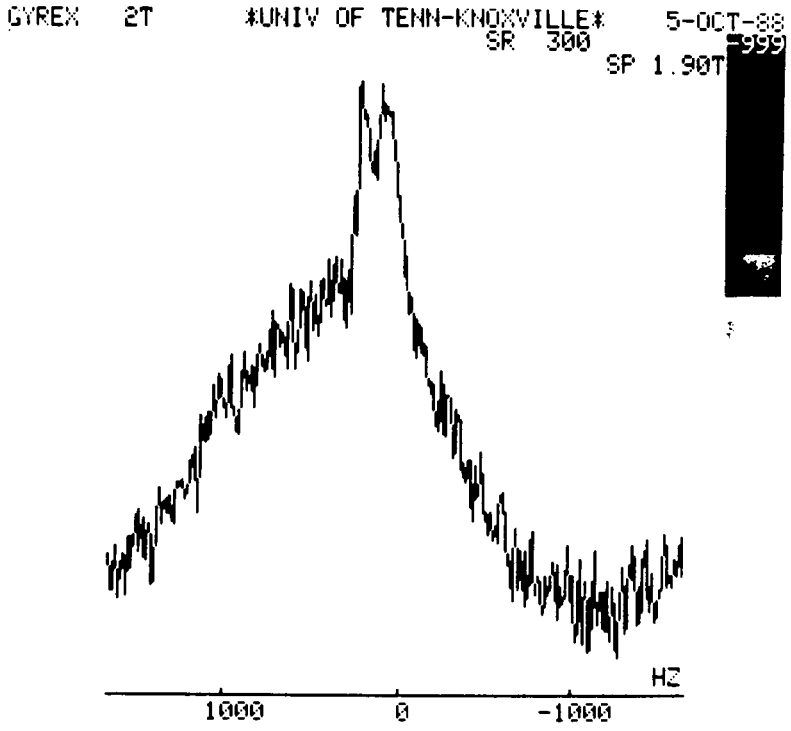

(b)

Figure 42 (continued)

are typical with NMR signals emitted by nuclei in a solid environment.[234] This result prohibited the use of glass in subsequent experiments.

Imaging experiments were performed on the 0.010 M BSSB solution (15 ml) using the gradient-echo protocol. The image of two dilute phantoms separated from one another along the x axis by 14 cm with their long axis aligned along the z direction is displayed as a 30 mm transverse slice in Figure 43. The image has a S/N ratio of 4.25 and an in-plane resolution of 3 cm along both directions (9 cm^2 pixel size, 27 cm^3 voxel size). Both boron images are extended along the vertical direction due to a partial resolution of the doublet signal along the frequency encoding axis. This result demonstrated the sensitivity limits required for imaging boron at the low concentrations present in the animal.

3. BSSB Rat Studies

Following the successful spectroscopy and imaging results of the BSSB agent in solution at therapeutic BNCT levels, the next step was to attempt to detect the signal from the agent present in animal tissue. The first ^{11}B NMR spectrum obtained from an intact rat,[235] which had been sacrificed following infusion with an aqueous BSSB solution via an intraperitoneally implanted osmotic pump which was rated to deliver 2 ml of solution continuously for 7.3 days, is presented in Figure 44. Previous experiments demonstrated that rats infused in this manner attain a boron concentration in the liver approaching 80 $\mu g/g$.[229] The spectrum was obtained using a saturation recovery protocol and is displayed with zero-order phase correction and 10 Hz exponential line broadening resulting in a S/N ratio of 13.8. The ^{11}B signal from the BNCT agent in the rat is less resolved than the signal from the agent in

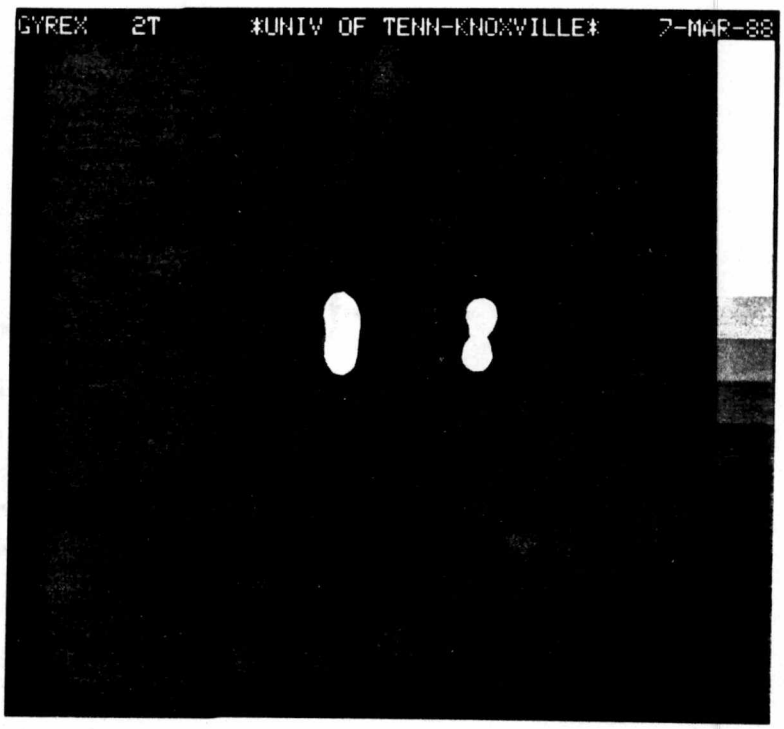

Figure 43. ^{11}B MR image of two 0.01 M BSSB phantoms obtained using a three-dimensional gradient echo protocol.

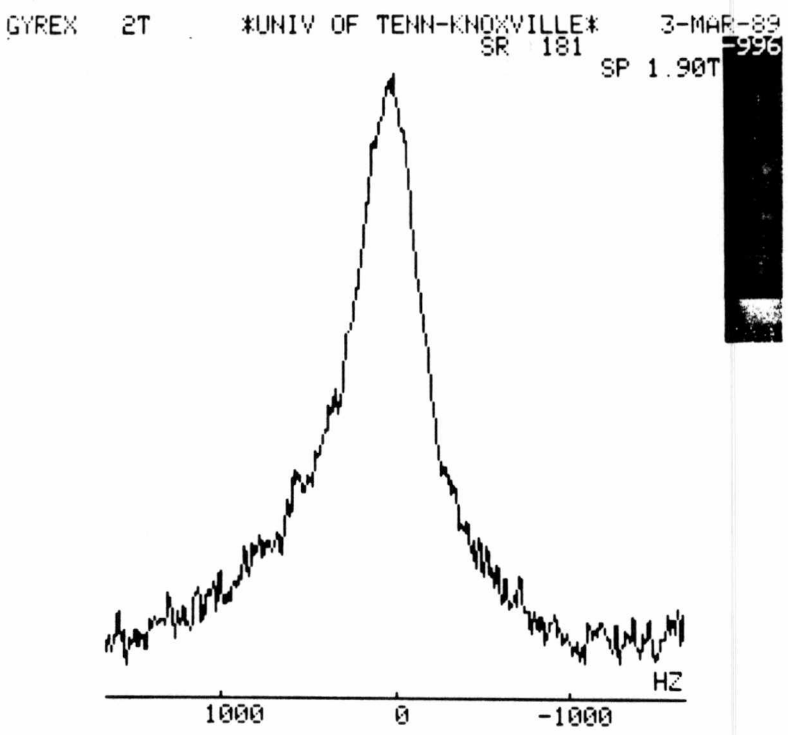

Figure 44. ^{11}B MR spectrum of a BSSB rat.

solution (Figure 42a). The broadening of the signal in the animal ($\Delta f_{1/2} = 470$ Hz) is caused by a shortening of the T_2 relaxation time, which is presumably due to a decrease in the correlation time resulting from a binding of the BNCT agent with a protein or other macromolecule (refer to p 10).

The transverse decay rate (T_2) of the ^{11}B signal from the rat was experimentally determined by acquiring various spectra using a variable time delay between the 90° pulse and the onset of signal acquisition. A plot of the experimental results, which was used to calculate T_2, is presented in Figure 45. The solid line represents a two-parameter, non-linear, least-squares fit to a single exponential with $T_2 = 740 \pm 60$ μs. The contribution of magnetic field inhomogeneity and susceptibility effects to this decay rate should be negligible since the proton MR signal width from the entire rat was on the order of 50 Hz (i.e. the width of the ^{1}H signal is significantly less than the width of the ^{11}B signal). If the line broadening of the ^{11}B signal was due to inhomogeneities, one would expect to see a similar effect on the proton signal. The fit by a single exponential is empirical since there are insufficient data points (and insufficient S/N) to be able to detect multiexponential components of the decay. The very short T_2 decay of the ^{11}B signal in the animal is a major obstacle to successful boron imaging.

Generation of MR images for fast relaxing nuclei is often hampered by the fact that the transverse relaxation times (T_2) are considerably shorter than the available time-to-echo (TE). The minimum obtainable TE in MR imaging using standard spin-echo and gradient-echo protocols is limited by hardware limitations associated with the use of magnetic field gradients. The application of magnetic field

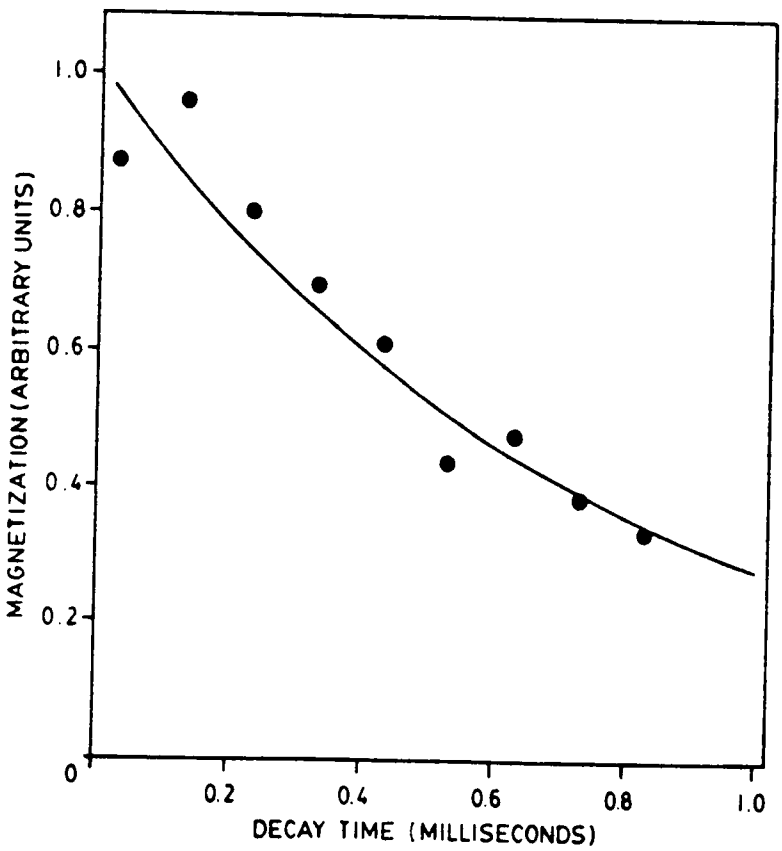

Figure 45. Transverse magnetization decay at variable time delays after a 90° pulse.

gradients is not an instantaneous process; however, there are finite rise times associated with turning on the gradients as well as finite fall times associated with turning off the gradients. Currently, echo times of 2.5 ms have been demonstrated by conventional imaging techniques.[236] It is possible to shorten TE to the order of 1 ms with the use of extremely weak gradients which require shorter rise and fall times; however, this results in poor spatial resolution. In certain situations, the intrinsic T_2 decay of the imaged species is so short that even after 1 ms most of the signal has already decayed, resulting in an unacceptably low signal level available for detection. Imaging requires much higher sensitivity than spectroscopy because the signal is spread over a larger frequency range. Due to instrumental limitations associated with the previously described gradient echo protocol used in the imaging experiments of BSSB in solution, the shortest TE available using this sequence was 1.7 ms. The utilization of a TE of this magnitude to the imaging of a species possessing a T_2 of 740 μs would result in a 90% decay of the original signal intensity prior to detection of the signal. When this sequence was applied towards imaging of the BNCT agent present in the intact rat, the ^{11}B signal was essentially undetectable. Therefore, an alternative method needed to be developed to achieve this purpose.

C. BACKPROJECTION IMAGING

Filtered backprojection techniques (refer to pp 16-20) can be used to image fast relaxing nuclei because the method relies on collecting the signal immediately after the pulse in the form of an FID rather than an echo. Therefore, a

backprojection pulse sequence was developed for ^{11}B imaging of the BSSB rat, which is illustrated in Figure 46. The sequence consisted of a non-selective 90° RF pulse of 100 μs duration followed by acquisition of the FID in the presence of a linear magnetic field gradient. The excitation bandwidth of the pulse was sufficiently broad to assure uniform excitation over the spatial dimension of interest. An important element in attempting to derive spatial information from the FID (rather than from an echo) is the onset of data acquisition as early as possible after the pulse. In the presence of the gradient, most of the signal decays for a time inversely proportional to the resulting width in the frequency domain. In addition, the longer the preacquisition delay, the larger is the frequency-dependent phase correction necessary to phase correctly the spectra; this introduces a baseline roll which interferes with spatial information provided by the lineshape. However, the preacquisition delay cannot be shortened at will due to a transient signal from the transmitter to the receiver which causes large baseline distortions. To minimize these problems, data acquisition was started 30 μs after the end of the pulse. When utilizing a dead time of this magnitude, 95% of the original signal intensity will remain upon data acquisition. The imaging experiment is conducted by acquiring various spectra in the presence of a variably oriented gradient with an amplitude of 0.183 G/cm and the resulting projections are used for filtered backprojection image reconstruction. The orientation of the gradient is rotated in a plane to cover a 360° area. Although the onset of sampling for projection reconstruction is also limited by the rise time of the frequency encoding read-out gradient, which must stabilize before the start of acquisition, this limitation was circumvented by turning on the gradient before the

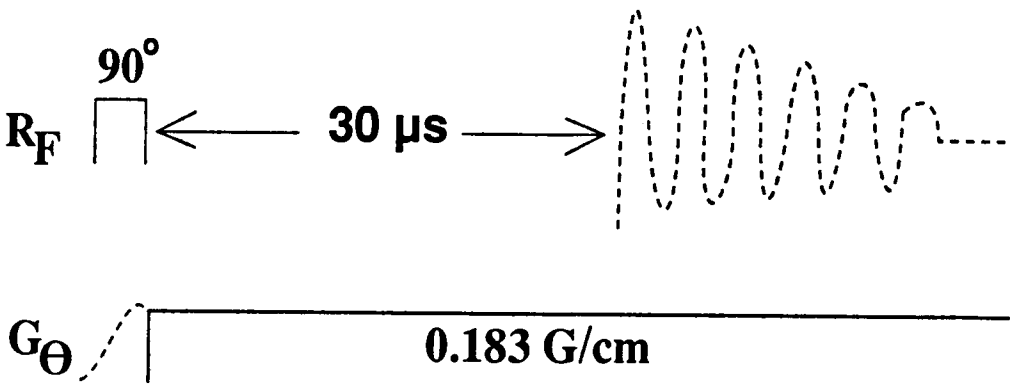

Figure 46. Backprojection imaging pulse sequence.

RF pulse at a time sufficient to allow the gradient to reach its maximum at the end of the pulse. More sophisticated sampling methods have been developed which compensate for finite gradient rise times and allow for the start of data acquisition to take place approximately 200 μs after the pulse.[237,238]

1. BSSB Phantom Studies

The original backprojection imaging experiments were conducted on aqueous BSSB solutions to determine if the technique provided the correct spatial information as well as to check for the existence of any imaging artifacts. The initial experiment was conducted on two of the 0.10 M BSSB phantoms (15 ml). The vials were separated from one another by 3 cm along the x direction with their long axis aligned parallel with the z axis. Various spectra were obtained using the backprojection pulse sequence and the resulting projections are presented in Figure 47. The projections are displayed with 5 Hz line broadening, zero-order phase correction and baseline correction. In the experiment, the gradient was rotated through the xy plane to cover an area of 360°. Ten projections were acquired at 18° increments. The number to the left of each projection denotes the exact angular orientation (in degrees) of the gradient relative to the x axis during data acquisition of that particular projection. For example, the projection designated by 0° was acquired with the gradient oriented parallel to the x axis and since this direction represents the maximum separation of the two vials, two signals result. Conversely, the projection designated by 90° was acquired with the gradient aligned perpendicular to the x axis (parallel with the y axis) and since this direction corresponds to no separation of the

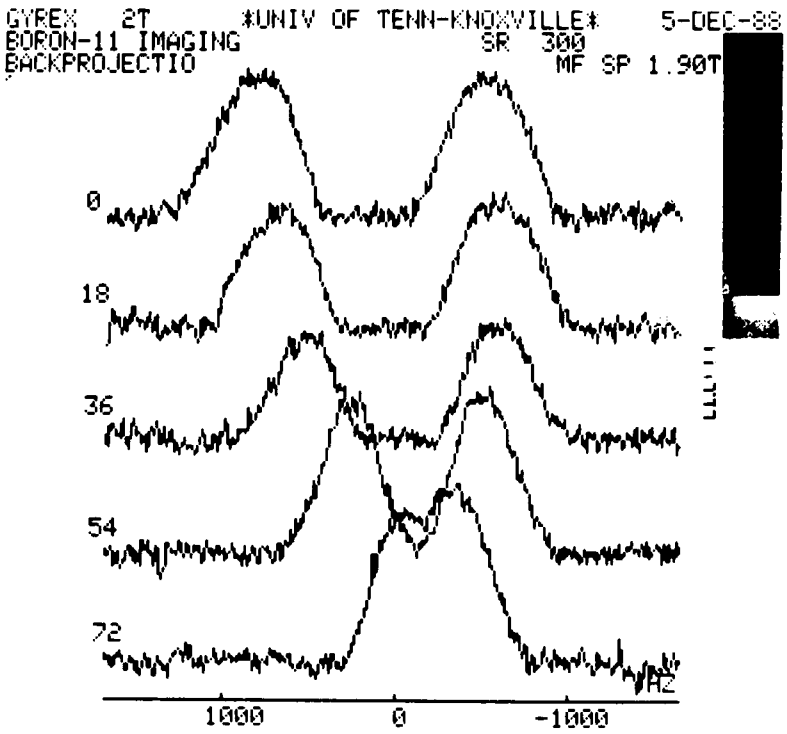

Figure 47. Projections obtained from two 0.1 M BSSB phantoms.

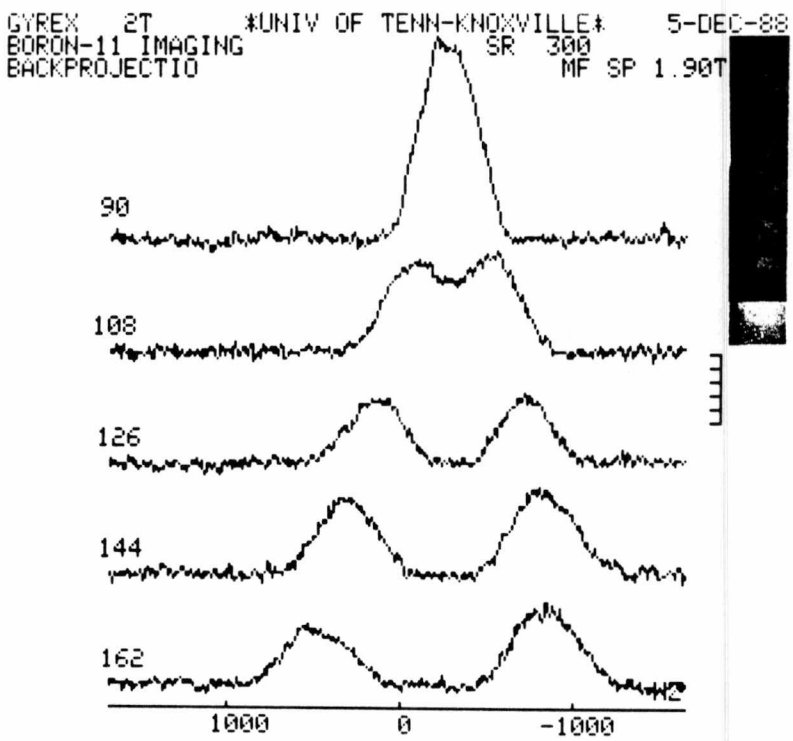

Figure 47 (continued)

two vials, only one signal results. The experiment required a total imaging time of 30 minutes.

The two-dimensional xy image reconstructed from the 10 projections is presented in Figure 48. The image has a S/N ratio of 4.9 and is free of artifacts. Corresponding proton MR images obtained from the phantoms using spin echo protocols revealed that the backprojection technique provides the correct spatial localization of the ^{11}B signal. Backprojection ^{11}B images were also performed on dilute phantoms containing a therapeutic dose of the BNCT agent. Although longer imaging times were required (5 hours), good results were obtained (S/N ratio of 3). The combined solution experiments revealed that the backprojection technique possesses the characteristics required for imaging the dimeric BSSB agent present in rat tissue both from a localization as well as a sensitivity standpoint.

2. BSSB Rat Studies

Following the successful solution experiments, backprojection imaging was conducted on an intact rat which had been infused with a BSSB solution via the previously described procedure.[229] The rat was placed in the magnet (centered along all three axis) with its long axis aligned along the x direction and its anterior-posterior axis oriented along the y direction. The experiment was performed in a similar manner described for the backprojection imaging of the BSSB solutions (refer to p 164) and the resulting projections are presented in Figure 49. The projections are displayed with 10 Hz line broadening, zero-order phase correction and no baseline correction. Although a small frequency-dependent phase shift should have been applied, the baseline distortion from such a correction was more severe than

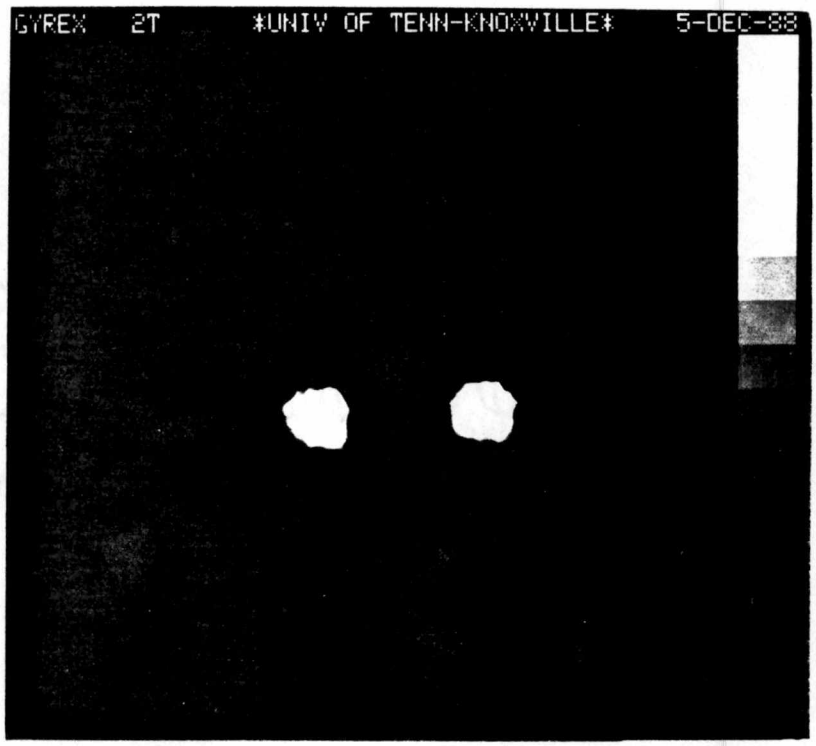

Figure 48. Backprojection xy image of two 0.1 M BSSB phantoms.

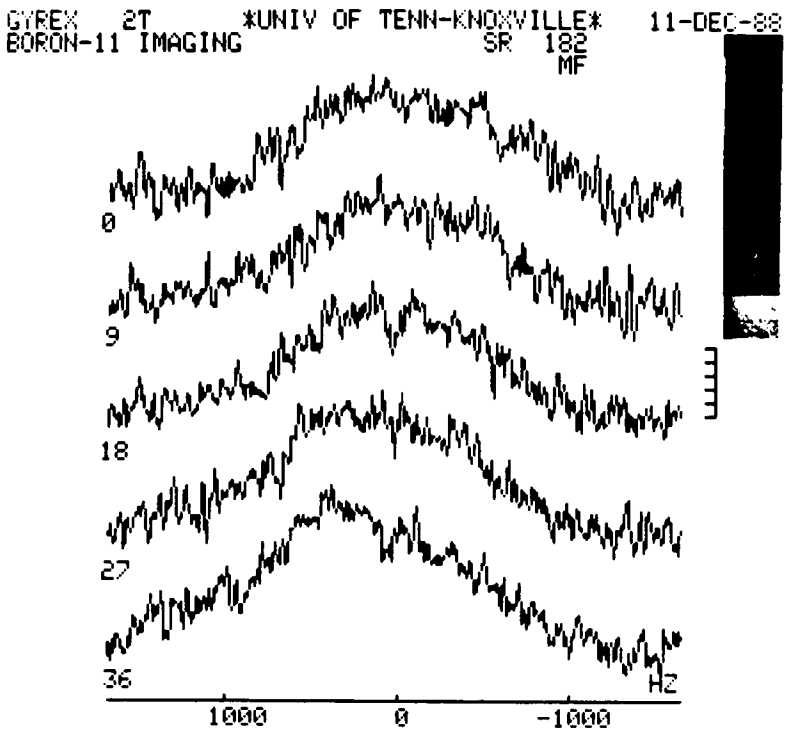

Figure 49. Projections obtained from a BSSB rat.

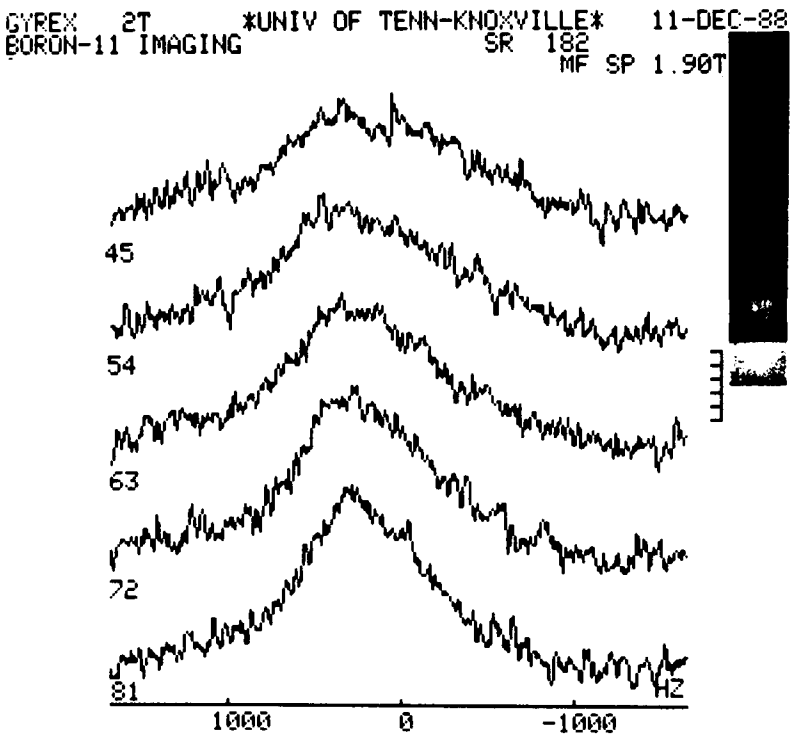

Figure 49 (continued)

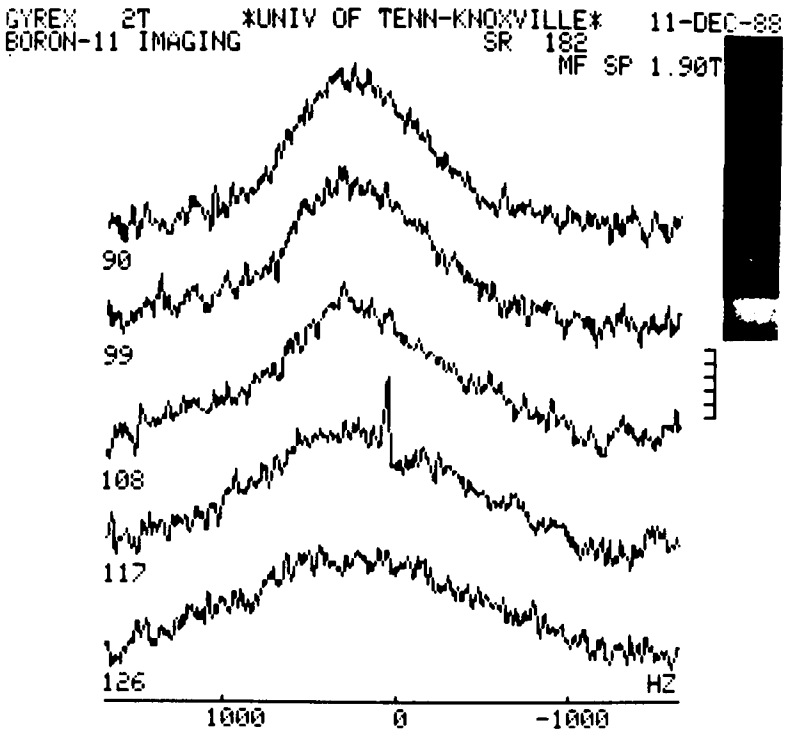

Figure 49 (continued)

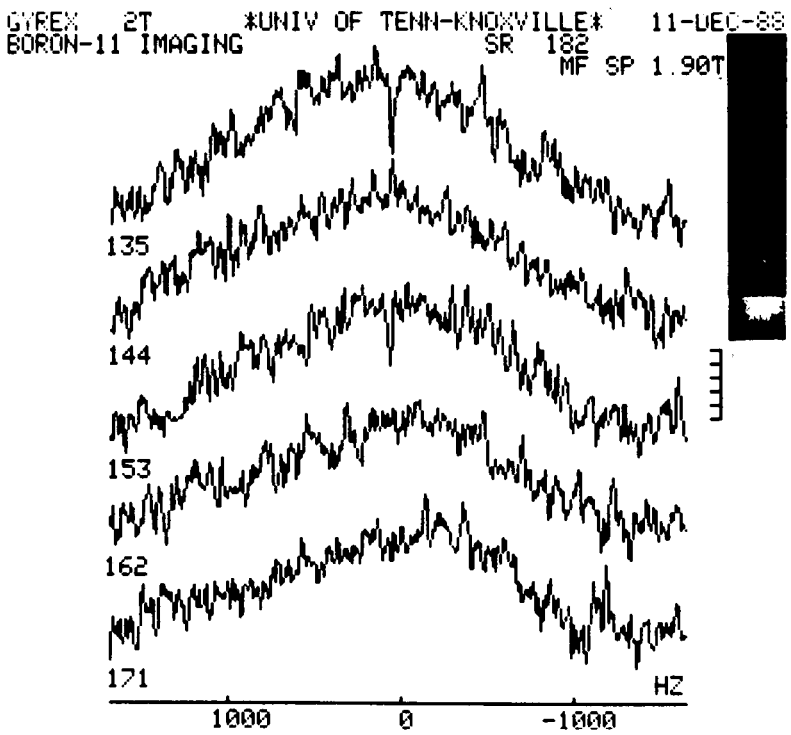

Figure 49 (continued)

the small distortion caused by the phase shift. Twenty projections were acquired at 9° increments. The number to the left of each projection indicates the gradient orientation (in degrees) from the long axis of the animal. The boron compound was localized in a rather small volume of the rat along the anterior-posterior axis which is illustrated in the projections acquired with the gradient oriented close to this axis. The signal is somewhat more spread along the long axis of the animal; the projections with the gradient oriented closely toward this axis show barely detectable signals which presumably adds to image distortion. Each projection was acquired using 8192 scans and a TR of 180 ms resulting in a scan time of 25 minutes per projection (total imaging time of 8.3 hours). The minimum achievable TR was limited due to instrumental constraints. Theoretically, since the T_1 relaxation of the ^{11}B signal in tissue is extremely short, the pulse repetition time can ultimately be reduced by at least one order of magnitude without sacrificing signal-to-noise.

The twenty projections were used for reconstruction of the first two-dimensional ^{11}B image of a BNCT agent present in animal tissue[235] which is presented in Figure 50. The image can be characterized in terms of spatial resolution, which defines the smallest spatial feature recognizable in the image, and contrast resolution or signal-to-noise, which defines the sensitivity within the smallest resolution element. These two performance criteria are intricately related since spatial resolution is limited on one hand by available effective gradient strength but ultimately by signal-to-noise since the smallest resolvable volume element will be one which still generates a detectable signal. Due to the convolution between the gradient-induced lineshape and the inherent broad linewidth of the signal, the linear

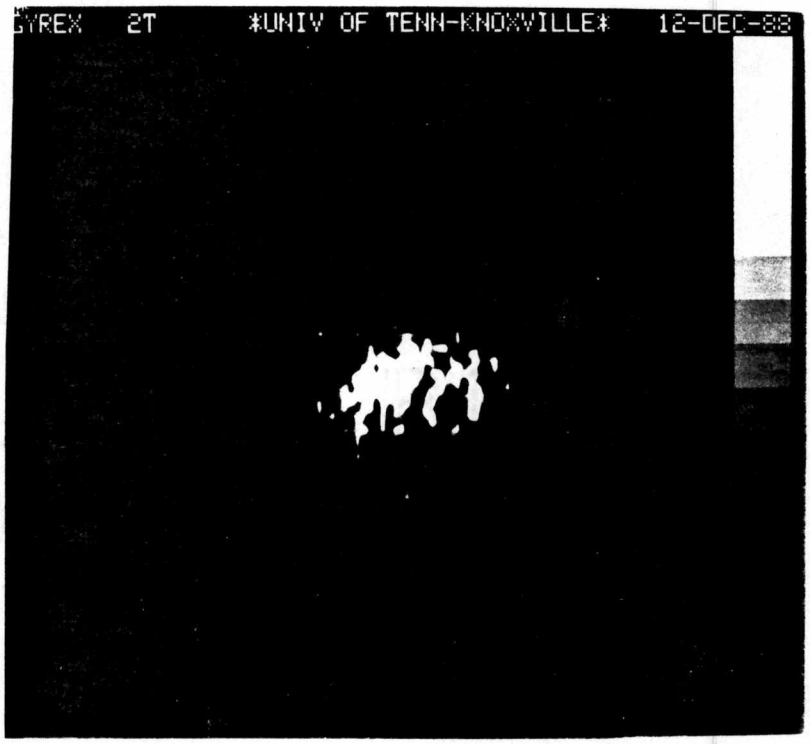

Figure 50. Backprojection xy image of a BSSB rat.

spatial resolution is approximately 3 cm in the imaged plane. The image is not resolved in the third dimension, perpendicular to the imaged plane, resulting in a voxel size of approximately 36 cc (the right-to-left axis of the rat covers a distance of 4 cm). With all the infused ^{11}B contained in a single voxel, the image S/N is about 2.5; therefore, the resolution in boron backprojection imaging experiments will ultimately be S/N limited. The transverse proton image obtained from the BSSB rat in the same plane as the boron image is presented in Figure 51. The imaging experiment was performed using a spin echo protocol (TR = 700 ms/TE = 30 ms/slice width = 5 mm) and a 30 cm Helmholtz saddle coil. The contoured area in the image indicates the location where the ^{11}B signal was detected in the backprojection image (Figure 50). The area corresponds to the rat's liver region, where the agent is known to localize.

The backprojection technique has inherent drawbacks such as the necessity for accurate phasing which is hampered by even a short receiver dead-time delay resulting in image distortion as well as the loss of sensitivity due to the preacquisition delay. In addition, the phenomenon of pulse breakthrough distorts the signal at early times after the pulse. Finally, there are spatial resolution limitations in all dimensions resulting from the convolution of the signal with the natural lineshape which is very broad in tissue. All of these are major obstacles which will probably render the backprojection method impractical in the long run. Therefore, an alternative approach needed to be developed for the imaging of BNCT agents in animal tissue.

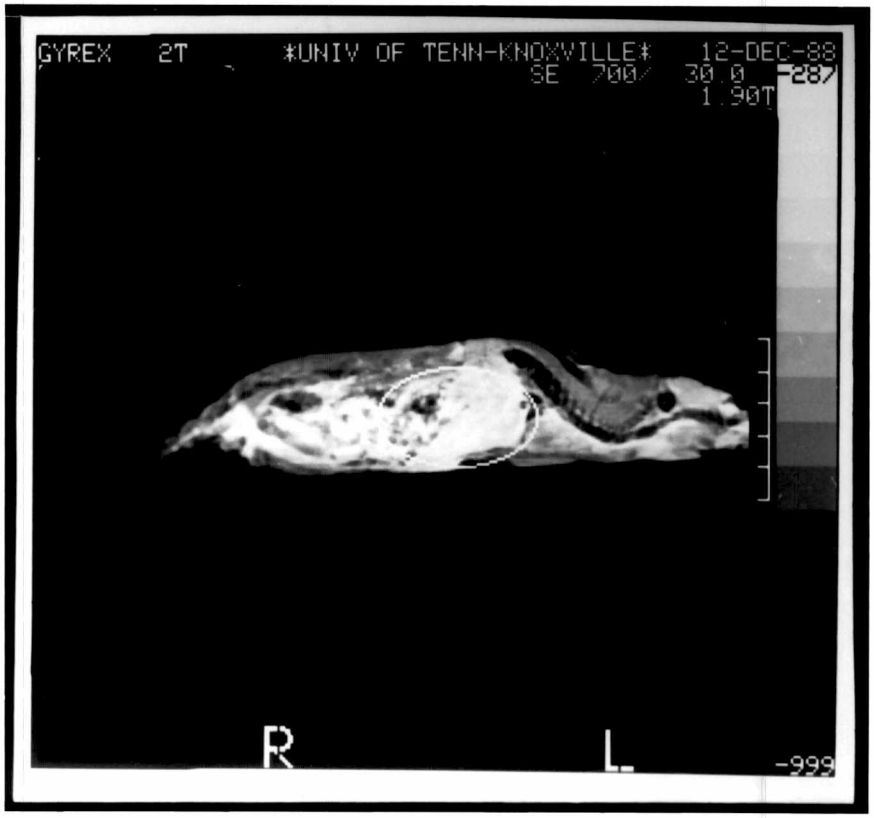

Figure 51. Proton MR image of a BSSB rat obtained using a spin echo protocol.

D. PSEUDO-3D IMAGING

The backprojection imaging technique is basically a one-dimensional NMR experiment. For the imaging of nuclei with very short T_2 relaxation, an alternative strategy which utilizes multi-dimensional Fourier transform reconstruction techniques was developed. In contrast to backprojection, the need to observe the signal immediately after the pulse is circumvented.[239] As with backprojection, the technique utilizes the FID, rather than an echo; however, the signal is entirely phase encoded but frequency encoding is omitted, as illustrated in the schematic description of the pulse sequence presented in Figure 52. The sequence consists of excitation of the nuclei with a 90° RF pulse of 100 μs duration followed by application of two simultaneous phase encoding gradients at directions perpendicular to one another. The time during which the gradients are phase encoding the signal is extremely short, 200 μs. This time is far too short to allow the gradients to rise to (and fall from) reasonable levels using conventional gradient power supplies; therefore, the gradients are turned on before the pulse and maintained at full level during the entire phase encoding time slot. Both spatial dimensions are phase encoded by an amplitude cycling of the gradients along the corresponding directions, which involves incrementing the two gradients in steps to a maximal value of 0.9 G/cm.

Following each phase encoding cycle, the entire FID is sampled (32 points) in the absence of a frequency encoding gradient. Fourier transformation of the signal along this additional dimension yields a third axis in the image which represents chemical shift. Since signal acquisition starts at 200 μs after the pulse, only 25% of the signal intensity from a species possessing a T_2 relaxation of 740 μs

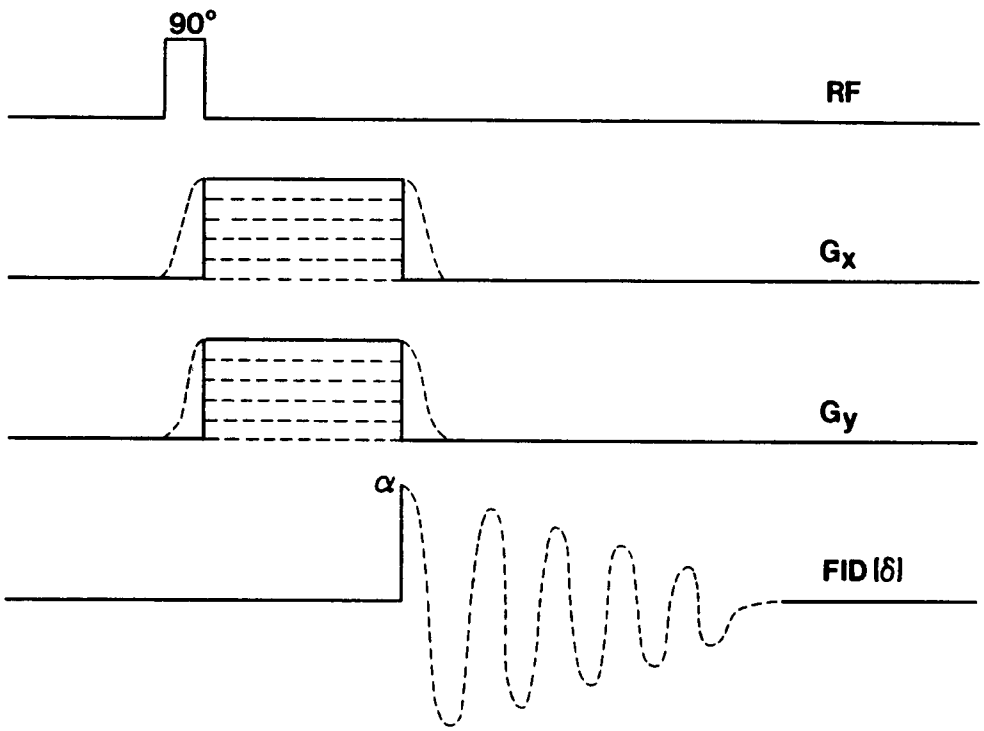

Figure 52. Pseudo-3D imaging pulse sequence.

is lost due to T_2 decay and distortions due to pulse breakthrough are reduced. In fact, the method may even be insensitive to such distortions, provided they are reproducible from cycle to cycle. In addition, since spatial information is reconstructed from phase encoded data only (i.e. no readout gradient is used), the convolution with the inherent broad lineshape is no obstacle to resolution. Therefore, the resulting resolution should be better than that obtained with the backprojection technique. The added advantage of the chemical shift information that is contained in the FID could be used to monitor the state of the BNCT agent in-vivo. For example, molecular changes in the agent as a result of an in-vivo biochemical degradation could be monitored through changes in the chemical shift of the ^{11}B signal. If different boron-containing species were present at different locations, it would easily be observed from the direct correlation of the MRS chemical shift information with the MRI spatial information, provided the different species have different chemical shifts. In addition, the projection of the chemical shift data onto the spatial axis would result in increased signal-to-noise.

The success of this new imaging method depends upon the use of short, intense and nonselective RF excitation pulses. The fact that a gradient is present during the pulse will have two consequences. First , a position dependent phase shift will be acquired by the spins during the excitation which can be shown, to a good approximation, to be linear, so that it will simply add to the total phase shift imposed during the phase encoding period. Second, a position-dependent modulation of the absolute magnitude of the transverse magnetization signal will result from the finite excitation band-width of the pulse. The frequency spread of the signal will depend

upon the spatial extension of the object from the magnet center and upon the value of the encoding gradient, which varies from cycle to cycle. Only the largest gradient values will create frequency offsets which will be significant when compared to the pulse bandwidth. However, the signal-to-noise in the image is determined predominately by the cycles in which the encoding gradient is small (or vanishes), therefore, image artifacts resulting from this phenomenon should be negligible. The minimal performance time of the proposed sequence is much longer than in conventional spin warp imaging, requiring at least one scan for each resolution element. But this is not an obstacle for the imaging of low-sensitivity nuclei, such as ^{23}Na or ^{11}B in-vivo, since the necessary number of scans needed for adequate signal averaging usually exceeds the minimal number of experiments required by the imaging process.

1. Phantom Studies

The new pseudo-3D imaging technique was initially applied to the imaging of boron phantoms to determine if the method provided the correct spatial localization of the ^{11}B signal as well as to check for the existence of image artifacts. The experiment was performed on two phantoms consisting of either a 0.2 M $NaBPh_4$ or a 0.2 M $B(OH)_3$ solution (2 ml). ^{11}B NMR spectroscopy revealed that the $NaBPh_4$ signal ($\Delta f_{1/2} = 21Hz$, $T_2 = 15$ ms) and the $B(OH)_3$ signal ($\Delta f_{1/2} = 78Hz$, $T_2 = 4.1$ ms) are separated from one another by 700 Hz. The two phantoms were placed in the magnet with their long axis aligned parallel with the x axis and separated from one another along that axis by 4.5 cm from the center of their long axis (their orientation along the y and z axis were the same - refer to Figure 13). The phantoms were

positioned along the z axis 2 cm from the magnet center. The $B(OH)_3$ phantom was placed to the right of the magnet center along the x axis while the $NaBPh_4$ phantom was placed to the left of the magnet center along that axis. Both phantoms were centered in the magnet along the y axis. The experiment was performed utilizing the x and z directions as the two phase encoding axis (the z axis was chosen as the slice select direction). The resulting images are presented as three-dimensional slices in which the signal distribution along the x direction is contained in the projected intensity along the horizontal axis of the slice and the distribution along the z axis is contained in the slice position. Vertical cross sections through the slices reveal the chemical shift information. Two of the slices from this experiment are presented as 5 mm transverse images in Figure 53.

Figure 53a shows the two phantoms separated from each other by 45 mm along the spatial axis (horizontal direction) and by 700 Hz along the chemical shift axis (vertical direction). The second spatial dimension was obtained from the spatial location of the slices in which the two phantoms appeared and corresponded to a slice position that was 2 cm from the magnet center along the z axis. When the experiment was repeated with the slice select direction oriented along the x axis, the two phantoms appeared in separate images. The width of the two phantom signals along the chemical shift axis is different due to the different linewidths (T_2 relaxation times) of the two boron species. The image has a S/N ratio of 10 and a linear resolution of 5.3 mm along the x spatial direction. The resolution along the z spatial direction is dictated by the slice width (5 mm). This result revealed that the new

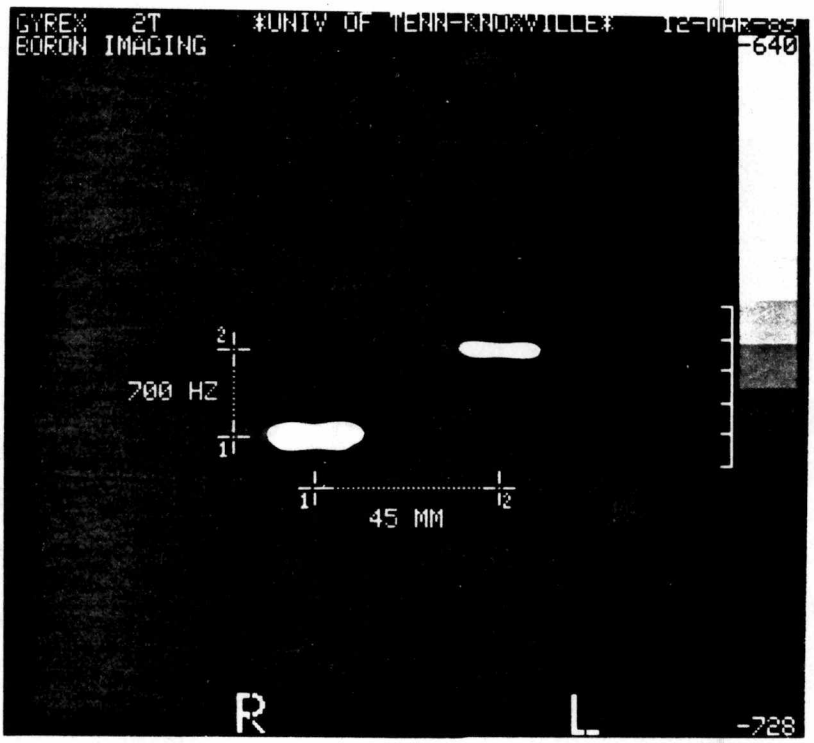

(a)

Figure 53. Pseudo-3D MR images of (a) a 0.2 M $B(OH)_3$ and a 0.2 M $NaBPh_4$ phantom and (b) a smearing artifact.

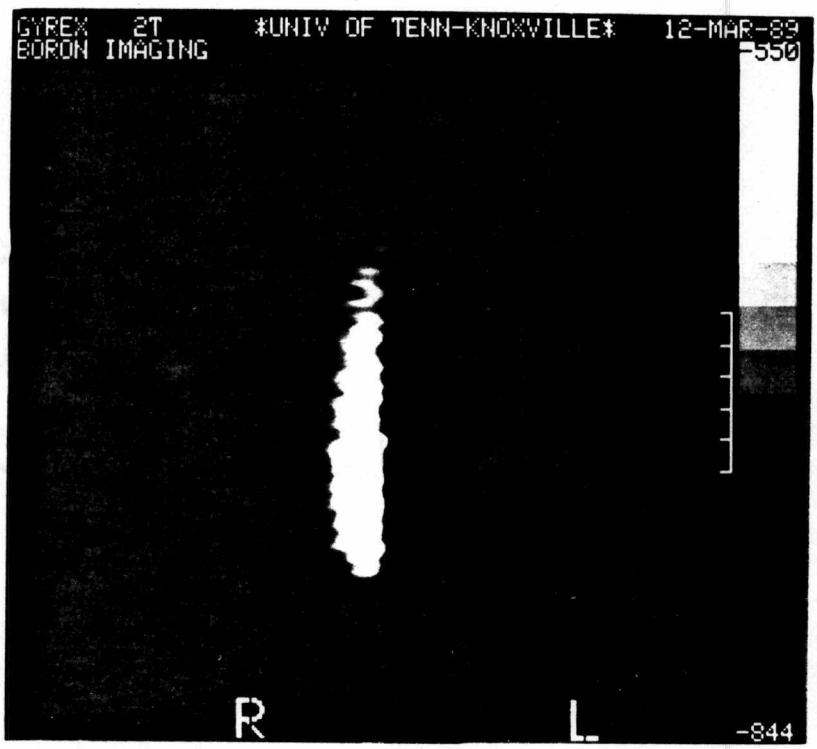

(b)

Figure 53 (continued)

pseudo-3D imaging technique provided the correct spatial as well as chemical shift information pertaining to the ^{11}B signal.

Figure 53b shows a smearing artifact observed when employing this technique which appeared in a different slice than the phantom images. Since the smearing artifact appeared to occupy a solid angle cone within the sampled three-dimensional space (two spatial and one spectral dimensions), with its head positioned at the magnet center and its tail extending toward the actual phantom signal, a clear phantom image (Figure 53a) could be separated from the artifact (Figure 53b) by placing the imaged species slightly off the magnet center along the slice select axis. The origin of the artifact was attributed to the relatively long decay time of the phase encoding gradients during signal detection (refer to Figure 52), which distorts the spectral information along the chemical shift axis. Since the decay occurred during the initial 1 ms of signal acquisition, the smearing appeared to have a more serious consequence for imaging of species having a short T_2 (boric acid phantom on right) as compared to a species having a relatively long T_2 (tetraphenylborate phantom on left) for which the smearing artifact is virtually non-existent. In fact, in an imaging experiment conducted on various boron phantoms with T_2 relaxation times varying from 15 ms to 840 μs, the extent of the smearing artifact became progressively worse with decreasing T_2. When the new technique was applied toward imaging of the BSSB rat, the separation of the true image from the smearing artifact was difficult due to the very short T_2 decay of the ^{11}B signal. However, for magnets equipped with eddy current compensation, the gradient decay times can be made

extremely short and therefore the observed T_2 smearing artifacts should be considerably reduced.[240]

The pseudo-3D imaging technique was modified in an effort to eliminate the smearing artifacts. In principle, following each cycle of the simultaneous phase encoding along two dimensions, a single data point can be sampled and used for the generation of a two-dimensional data matrix. Therefore, after sampling of the first data point (designated as α in Figure 52), the phase encoding gradients are turned off so that their relatively long decay time no longer affects or distorts the data. A fully phase encoded two-dimensional data matrix can thus be generated point by point. Fourier transformation of the data in the usual manner can be performed to yield a two-dimensional image. An extension to three spatial dimensions is achieved by adding a third phase encoding gradient along the remaining axis. With this modification, the chemical shift information is lost; however, this may be a mute point because the short T_2 of the ^{11}B signal in-vivo will cause the spectral data to be distorted (i.e. resolution of the different species will be difficult due to the broad linewidth of the signals).

The modified pseudo-3D imaging method was initially performed on a phantom consisting of a 0.50 M $NaBPh_4$ solution (15 ml). The phantom was placed in the magnet with its long axis aligned along the x direction (refer to Figure 13). The experiment was performed in which phase encoding was applied along the x and y directions to give the resulting two-dimensional image presented in Figure 54. The image shows the x spatial dimension oriented along the horizontal direction and the y spatial dimension oriented along the vertical direction. Due to limitations in the

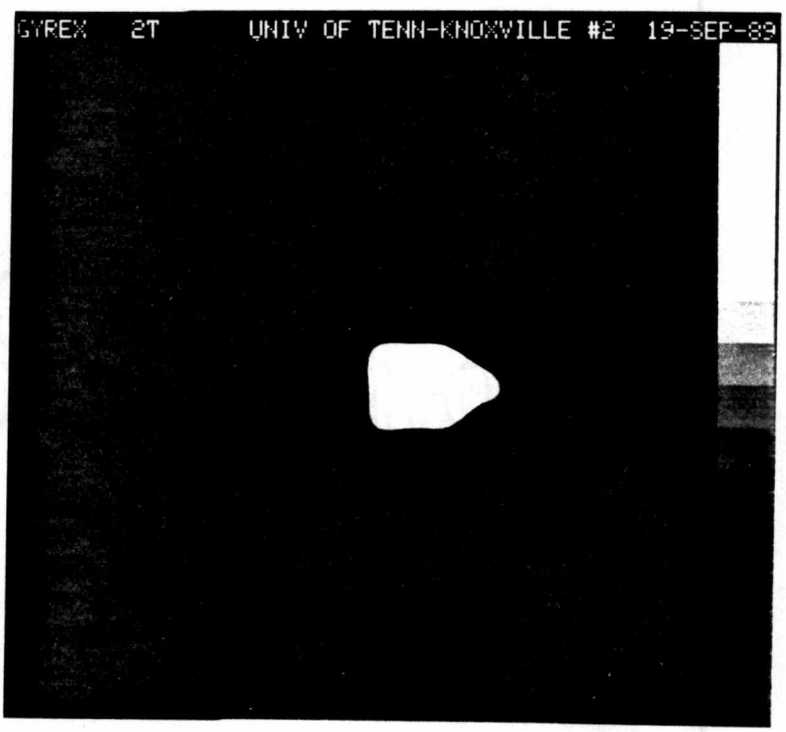

Figure 54. Pseudo-3D ^{11}B MR image of a 0.5 M $NaBPh_4$ phantom using the single point reconstruction method.

software, 32 points (rather than a single data point) were sampled in each cycle. The proper single point data matrix, which was created by a post-processing computer program that picked the first point from each cycle of the acquisition, was used for image reconstruction. The image has a S/N ratio of 90 and linear resolution of 7 mm along both the x and y axis. No spatial resolution along the z axis was achieved; therefore, the effective thickness of the image corresponds to the entire diameter of the bottle. This result revealed that the modified pseudo-3D imaging method provided high quality two-dimensional images that were free of smearing artifacts. The next step was to apply this technique toward the imaging of a species possessing a very short T_2 relaxation time.

2. BSSB Rat Studies

The new fully phase encoded, single point, pseudo-3D imaging method was next applied toward the imaging of the BNCT agent present in the intact rat in an effort to overcome the limitations imposed by the short T_2 of the ^{11}B signal. The experimental set up for the ^{11}B backprojection imaging of the BSSB rat allowed for subsequent proton imaging without moving the animal (refer to p 198). The rat was positioned in the magnet such that its head-to-tail axis was aligned along the x direction and its anterior-posterior axis aligned along the y direction (refer to Figure 13). Two plastic syringes, each containing 0.50 ml of a 50 mM boric acid solution, were fixed to the back of the animal, one towards the head and the other towards the tail section. The imaging experiment, which employed phase encoding along the x and y directions, as well as the data manipulation was performed in a similar manner to that described for the imaging of the 0.50 M $NaBPh_4$ phantom utilizing

the modified technique (refer to pp 185-187). The resulting two-dimensional image, which provides spatial information along the x and y directions and shows the ^{11}B signal intensity integrated along the z axis (the right-to-left axis of the animal), is presented in Figure 55. Three distinct areas of signal intensity are visible, with the two upper spots corresponding to the two syringes and the lower region in-between to the ^{11}B distribution of the BNCT agent within the animal. The signal intensity from the left syringe, which is situated towards the tail of the animal, is decreased (as compared to the right syringe) because it was positioned in a region of inhomogeneous RF at the edge of the ^{11}B solenoidal coil. The experiment was performed utilizing a TR of 36 ms, a FOV along each spatial direction of 26 cm, 20 increments per each phase encoding gradient and 256 signal averages per each phase encoding cycle resulting in an imaging time of 61.5 minutes, a S/N ratio of 20 (as pertaining to the BNCT agent signal) and a linear resolution of 13 mm along both the x and y axis. Since no spatial resolution along the z axis was achieved, the voxel size is approximately 7 cc. Since the T_1 of the ^{11}B signal in tissue is so short, the same resolution and S/N ratio could have been achieved in about one quarter of the actual imaging time; however, instrumental limitations prohibited the utilization of a shorter TR. From the S/N ratio, it can be estimated that roughly half of the boron concentration present in this image could be detected at the same resolution. Detecting smaller amounts would require an increase in the total imaging time proportional to the square of the decrease in the signal.

The two-dimensional proton image of the BSSB rat corresponding to the same view in the boron image (Figure 55), which was obtained with a 30 cm saddle coil

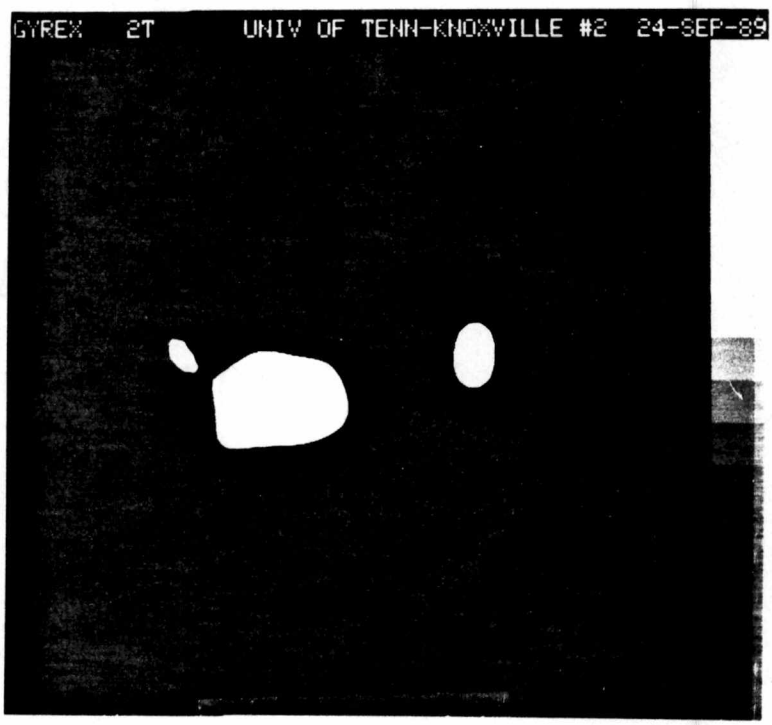

Figure 55. Pseudo-3D ^{11}B MR image of a BSSB rat utilizing the single point reconstruction method.

following removal of the ^{11}B solenoidal coil utilizing a spin echo protocol (TR = 1500 ms/TE = 50 ms/slice width = 10 mm/FOV = 26 cm), is presented in Figure 56. After proper superposition of the boron and proton images which was achieved by the alignment of the syringe signals visible on both images, the location of the ^{11}B intensity from the BNCT agent within the rat was outlined on the proton image (Figure 56). As expected, the area in which the agent is concentrated appears to be the liver of the animal. The contoured area outside of the animal, which corresponds to a distance of 5 mm from the animal's back, is within the experimental resolution limits.

These results revealed that the new single point, pseudo-3D imaging technique can be utilized for the spatial mapping of nuclear species with rapid decay rates of their transverse magnetization. This method has several advantages when compared to the backprojection technique. First, the natural linewidth of the signal (which is expected to be very broad due to the short T_2) does not degrade the spatial resolution since no frequency encoding is employed. In fact, for the same reason, images acquired by this method will be free of artifacts and degradation resulting from magnetic field inhomogeneities, susceptibility variations and chemical shifts. All of this is achieved without having to resort to gradients which are large compared to the prevalent interaction strengths in the spin system. Second, the analog filter can be set to a much smaller frequency cutoff than with backprojection resulting in a substantial improvement in signal-to-noise. Finally, distortions from pulse breakthrough are reduced due to the increased dead time. In addition to the imaging of BNCT agents in-vivo, this technique could find other applications in living

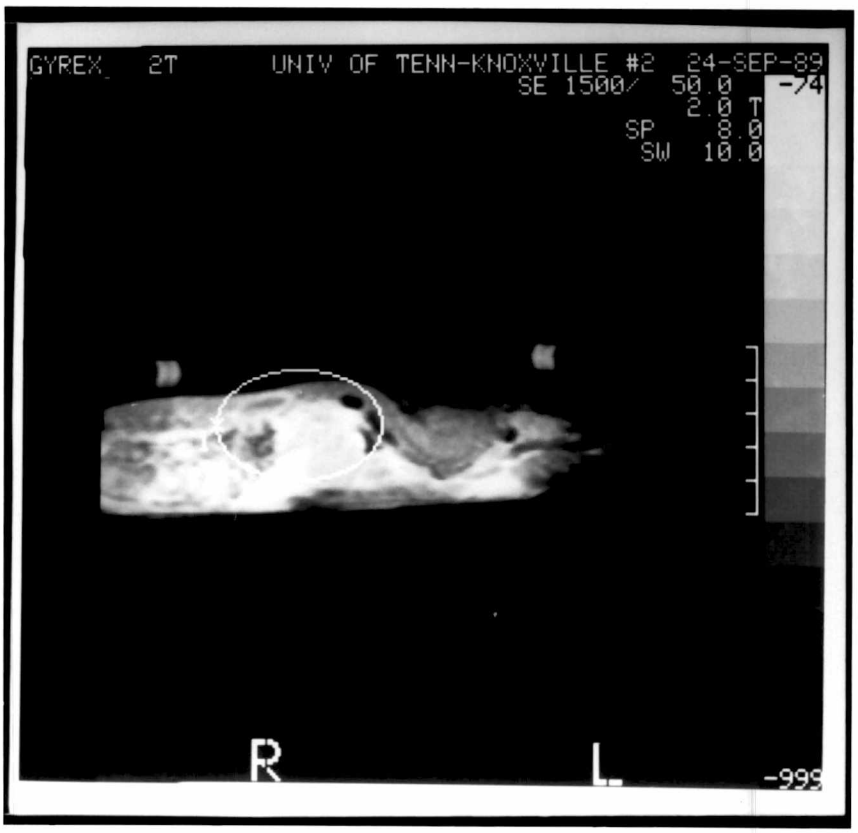

Figure 56. Proton MR image of a BSSB rat obtained using a spin echo protocol.

systems, such as imaging of the short T_2 component of tissue ^{23}Na, and also in non-biological systems where rapid transverse magnetization decay rates are caused by a solid-like character of the spin interaction mechanisms.

E. CONCLUSION

Boron-11 MRS and MRI offer promise for localizing and quantifying BNCT agents in-vivo. The experiments presented in Part II demonstrate that BNCT agents can be successfully imaged by MRI at therapeutic doses. Qualitative assessments of boron concentrations can be inferred but precise measurements are not yet possible. Sensitivity and resolution enhancement will be required before these techniques become clinically useful. A variety of possibilities exist to achieve these purposes. One method involves the improvement of RF coils in order to optimize the coils with respect to sensitivity and also with respect to the recovery or "dead" time, which limits the minimal time between the end of the pulse and the onset of signal acquisition. An additional improvement can be achieved by using higher magnetic field strengths. Currently, magnets with 4.7 Tesla fields are being utilized in animal experiments as well as in human applications. The highest sensitivity for the detection of these agents in-vivo can be achieved by detecting their ^{1}H rather than ^{11}B signals, which utilizes the boron-hydrogen coupling interaction via polarization transfer techniques. Localized spectroscopy experiments via the utilization of small surface coils could provide a method for the direct quantification of the agent at the target site.

CHAPTER VII

EXPERIMENTAL METHODS

A. GENERAL

1. Instrumentation

Imaging and spectroscopy experiments conducted on phantoms and rats were performed using a Gyrex 1.9 T, 90 cm horizontal bore, multinuclear whole-body MRI unit (Elscint Corp.) operating at 26 MHz for ^{11}B and 81 MHz for ^{1}H. An octagonal surface coil (12 cm x 12 cm) or a four-turn solenoidal coil (7 cm diameter, 15 cm length) were used for the ^{11}B experiments. A spin echo imaging protocol and a 30 cm Helmholtz saddle coil was employed for the proton measurements. High resolution NMR experiments were conducted using a Joel FX90Q FT-NMR spectrometer.

2. Phantoms

Phantoms consisted of aqueous solutions (sodium tetraphenylborate, boric acid or BSSB) at various concentrations (0.50 M, 0.20 M, 0.10 M, 0.01 M) and volumes contained in cylindrical plastic containers. $NaBPh_4$ solutions were adjusted to pH 5.0 to avoid decomposition. All solutions were stored at room temperature.

3. BNCT Agent

Cesium μ-disulfido-bis(undecahydro-closo-dodecaborate), $Cs_4B_{24}H_{22}S_2$, was prepared via oxidation of the monomeric sulfhydryl dodecaborane, $Cs_2B_{12}H_{11}SH$

(Callery Chemical Company, Callery, PA).[241] The sodium salt ($Na_4B_{24}H_{22}S_2$), which was obtained by passing the cesium analogue over a Dowex 50 x W8 resin,[225] was used to infuse animals and prepare phantoms.

4. Animals

The animals used were Fischer 344 male rats (Taconic Farms, Germantown, NY) weighing approximately 250 g. Each animal received 250 μg of boron per gram of body weight of the BNCT agent which was infused via an intraperitoneally implanted osmotic pump (Alza Corp., Palo Alto, CA) rated to deliver 2 ml of solution continuously for 7.3 days. Previous experiments demonstrated that rats infused in this manner attain a boron concentration in the liver approaching 80 μg/g.[226] The rats were euthanized one week after the pumps were implanted and the carcasses stored at -10 °C or lower. Imaging and spectroscopy experiments performed on the animals were conducted at ambient temperatures.

B. SPECTROSCOPY EXPERIMENTS

1. $NaBPh_4$ Phantom

The phantom consisted of an aqueous 0.2 M sodium tetraphenylborate solution (1.7 mg/ml ^{11}B) at a volume of 50 ml contained in a cylindrical plastic bottle. The phantom was placed in the magnet centered along all three axis. The ^{11}B NMR spectrum was obtained using a saturation recovery protocol and the octagonal surface coil. The pulse sequence consisted of a nonselective RF pulse of 400 μs duration followed by detection of the FID 1 ms later using an acquisition time

of 82 ms. The experiment was performed using 20 scans and a TR of 200 ms resulting in a scan time of 4 seconds.

2. Concentrated BSSB Phantom

The phantom consisted of an aqueous 0.1 M BSSB solution (natural abundance levels of boron, 0.86 mg/ml ^{11}B) at a volume of 25 ml contained in a cylindrical plastic bottle. The phantom was placed in the magnet centered along all three axis. The ^{11}B NMR spectrum was obtained using the previously described saturation recovery pulse sequence (refer to p 194) and the octagonal surface coil. The experiment was conducted using 1000 scans and a TR of 200 ms resulting in a scan time of 3.3 minutes.

3. Dilute BSSB Phantoms

The phantoms consisted of an aqueous 0.01 M BSSB solution (natural abundance levels of boron, 86 μg/ml) at a volume of 15 ml contained in small cylindrical vials (plastic or glass). The phantoms were placed in the magnet centered along all three axis. The ^{11}B NMR spectra were obtained using the previously described saturation recovery pulse sequence (refer to p 194) and the four-turn solenoidal coil. The coil was placed in the magnet with its long axis aligned along the x axis which is perpendicular to B_o (refer to Figures 13 and 15). The experiment was performed using 2000 scans and a TR of 300 ms resulting in a scan time of 10 minutes.

4. BSSB Rat

The rat was placed in the magnet centered along all three axis. The experiment was performed using the four-turn solenoidal coil, which was oriented perpendicular to B_o, and a spectroscopy protocol similar to the previously described saturation recovery sequence (refer to p 194) except that the time duration between RF excitation and detection of the signal (dead time) was 200 μs as opposed to 1 ms in the solution experiments. The experiment was conducted using 8192 scans and a TR of 180 ms resulting in a scan time of 25 minutes. The spectra utilized for the determination of the T_2 relaxation rate of the ^{11}B signal were obtained in an identical manner except that variable time delays (30 μs, 100 μs, 200 μs, 300 μs, 400 μs, 500 μs, 600 μs, 700 μs, 800 μs) between the 90° pulse and the onset of signal acquisition were employed. A plot of the relative signal intensities versus time was constructed and used to calculate T_2.

C. THREE-DIMENSIONAL GRADIENT ECHO IMAGING EXPERIMENTS

1. $NaBPh_4$ Phantom

The phantom consisted of an aqueous 0.2 M sodium tetraphenylborate solution (1.7 mg/ml ^{11}B) at a volume of 50 ml contained in a cylindrical plastic bottle (5 cm diameter). The experiment was performed with the phantom centered in the magnet along all three axis and the long axis of the bottle aligned along the y direction (refer to Figure 13). The image was obtained utilizing a three-dimensional gradient-echo imaging protocol (refer to pp 29-32) and the octagonal surface coil. The experiment was conducted by obtaining three 10 mm coronal slices

under the following imaging parameters: TE of 6 ms, TR of 60 ms, field-of-view (FOV) of 22 cm, 10 scans per each phase encoding increment and a 45 x 45 acquisition matrix per slice resulting in an imaging time of 1.3 minutes and an in-plane resolution of 0.49 cm.

2. Dilute BSSB Phantoms

The phantoms consisted of an aqueous 0.01 M BSSB solution (natural abundance levels of boron, 86 μg/ml) at a volume of 15 ml contained in small cylindrical plastic vials (2.5 cm diameter, 3.5 cm length). The two dilute phantoms were separated from one another along the x axis by 14 cm with their long axis aligned along the z direction. The image was obtained utilizing a three-dimensional gradient-echo imaging protocol (refer to pp 29-32) and the four-turn solenoidal coil. The experiment was conducted by obtaining one 30 mm transverse slice under the following imaging parameters: TE of 1.7 ms, TR of 100 ms, FOV of 60 cm, 64 scans per phase encoding increment and a 20 x 20 acquisition matrix which resulted in an imaging time of 2.1 minutes and an in-plane resolution of 3 cm.

D. BACKPROJECTION IMAGING EXPERIMENTS

1. Concentrated BSSB Phantoms

The phantoms consisted of an aqueous 0.1 M BSSB solution (natural abundance levels of boron, 0.86 mg/ml) at a volume of 15 ml contained in small cylindrical plastic vials (2.5 cm diameter, 3.5 cm length). The vials were separated from one another by 3 cm along the x direction with their long axis aligned parallel

with the z axis. The experiment was performed using the backprojection pulse sequence (refer to pp 161-164) and four-turn solenoidal coil. Ten projections were acquired at 18° increments by rotating the gradient through the xy plane. Each projection was acquired using 600 scans and a TR of 300 ms resulting in a scan time of 3 minutes per projection (total imaging time of 30 minutes). The ten projections were used for reconstruction of the backprojection image.

2. BSSB Rat

The rat was placed in the magnet centered along all three axis. The experiment was performed with the rat placed in a plastic tube (6.5 cm diameter, 12 cm length) that was mounted in a wooden holder. The diameter of the tube was such that the four-turn solenoidal coil would fit snugly around it. This would allow for the removal of the ^{11}B coil and replacement with the ^{1}H coil for proton imaging without moving the animal. The entire apparatus was placed in the standard QA (quality assurance) phantom holder which situates the sample in the magnet center. The rat was oriented with its long axis aligned along the x direction and its anterior-posterior axis aligned along the y direction. The experiment was performed utilizing the backprojection pulse sequence (refer to pp 161-164) in which twenty projections were acquired at 9° increments by rotating the gradient through the xy plane. Each projection was acquired using 8192 scans and a TR of 180 ms resulting in a scan time of 25 minutes per projection (total imaging time of 8.3 hours). The twenty projections were used for reconstruction of the backprojection image.

E. PSEUDO-3D IMAGING EXPERIMENTS

1. 0.2 M $NaBPh_4$ and 0.2 M $B(OH)_3$ Phantoms

The phantoms consisted of 2 ml of either a 0.2 M $NaBPh_4$ or 0.2 M $B(OH)_3$ solution contained in a cylindrical plastic vial (12 mm diameter, 17 mm length). The two phantoms were placed in the magnet with their long axis aligned parallel with the x axis and separated from one another along that axis by 4.5 cm from the center of their long axis (their orientation along the y and z axis were the same - refer to Figure 13). The phantoms were situated in which their position along the z axis was 2 cm from the magnet center. The $B(OH)_3$ phantom was placed to the right of the magnet center along the x axis while the $NaBPh_4$ phantom was placed to the left of the magnet center along that axis. Both phantoms were centered in the magnet along the y axis. The experiment was performed utilizing the pseudo-3D pulse sequence (refer to pp 177-180) and the four-turn solenoidal coil and the x and z directions were chosen as the two phase encoding axis. The experiment was conducted by obtaining sixteen 5 mm transverse slices (16 increments of the z phase encoding gradient) under the following imaging parameters: TR of 300 ms, FOV of 8.5 cm along the x spatial axis, 2 scans per each phase encoding increment and 16 increments of the x phase encoding gradient resulting in an imaging time of 2.5 minutes and a linear resolution of 5.3 mm along the x spatial direction. The FOV along the z spatial direction is dictated by the slice width and number of slices (8 cm).

2. 0.5 M $NaBPh_4$ Phantom

The phantom consisted of 15 ml of a 0.5 M $NaBPh_4$ solution contained in a cylindrical plastic vial (20 mm diameter, 32 mm length). The phantom was placed in the magnet with its long axis aligned along the x direction (refer to Figure 13). The experiment was performed utilizing the pseudo-3D pulse sequence (refer to pp 177-180) and the four-turn solenoidal coil and phase encoding was applied along the x and y directions. The experiment was conducted utilizing a TR of 300 ms, a FOV along each spatial direction of 14 cm, 20 increments per each phase encoding gradient and two signal averages per each phase encoding cycle resulting in an imaging time of 3.8 minutes and a linear resolution of 7 mm along both the x and y axis.

3. BSSB Rat

The experimental set up used for the ^{11}B backprojection imaging of the BSSB rat which allows for subsequent proton imaging without moving the animal was employed (refer to p 198). The rat was positioned in the magnet such that its head-to-tail axis was aligned along the x direction and its anterior-posterior axis aligned along the y direction (refer to Figure 13). Two plastic syringes, each containing 0.5 ml of a 50 mM boric acid solution, were fixed to the back of the animal; one towards the head and the other towards the tail section. The imaging experiment, which employed phase encoding along the x and y directions, as well as the data manipulation was performed in a similar manner to that described for the imaging of the 0.5 M $NaBPh_4$ phantom (refer to pp 185-187) utilizing the modified pseudo-

3D technique (refer to pp 177-180). The experiment was performed utilizing a TR of 36 ms, a FOV along each spatial direction of 26 cm, 20 increments per each phase encoding gradient and 256 signal averages per each phase encoding cycle resulting in an imaging time of 61.5 minutes and a linear resolution of 13 mm along both the x and y axis. No spatial resolution along the z axis was achieved.

LIST OF REFERENCES

1. Bloch, F. *Phys. Rev.* **1946**, *70*, 460-473.

2. Mansfield, P.; Morris, P.G. *NMR Imaging in Biomedicine*; Academic Press: New York, 1982.

3. Lauterbur, P.C. *Nature* **1973**, *242*, 190-191.

4. Henshaw, W.S.; Bottomley, P.A.; Holland, G.N. *Nature* **1977** *270*, 722-723.

5. Becker, E.D. *High Resolution NMR: Theory and Chemical Applications*; Academic Press: New York, 1969; pp 12-21.

6. Shaw, D. *Fourier Transform NMR Spectroscopy*; Elsevier Science Publishing: New York, 1984; pp 11-17.

7. Farrar, T.C. *An Introduction to Pulse NMR Spectroscopy*; Farragut Press: Chicago, 1987; pp 1-31.

8. Partain, C.L.; James, A.E.; Rollo, F.D. *Nuclear Magnetic Resonance (NMR) Imaging*; W.B. Saunders: Philadelphia, 1983; pp 73-91.

9. Stark, D.D.; Bradley, W.G. *Magnetic Resonance Imaging*; C. V. Mosby Company: St. Louis, 1988.

10. Friedman, B.R. *Principles of MRI*; McGraw-Hill: New York, 1989.

11. Benn, R.; Gunther, H. *Angew. Chem. Int. Ed. Engl.* **1983**, *22*, 350-380.

12. Bax, A. *Two-Dimensional Nuclear Magnetic Resonance in Liquids*; Delft University Press: Boston, 1984; pp 1-48.

13. Kessler, H.; Gehrke, M.; Griesinger, C. *Angew. Chem. Int. Ed. Engl.* **1988**, *27*, 490-536.

14. Kaufman, L.; Crooks, L.E.; Margulis, A.R. *Nuclear Magnetic Resonance Imaging in Medicine*; Igaku-Shoin: New York, 1981.

15. Smith, S.L. *Anal. Chem.* **1985**, *57*, 595-608.

16. Crooks, L.; Arakawa, M.; Hoenniger, J. *Radiology* **1982** *143*, 169-174.

17. Alfrid, R.; Haaga, J. *Radiology* **1982** *143*, 175-181.

18. Harris, R.K.; Mann, B.E. *NMR and the Periodic Table*; Academic Press: New York, 1978; p. 5.

19. Carr, H.Y.; Purcell, E.M. *Phys. Rev.* **1954**, *94*, 630.

20. Hounsfield, G.N. *Br. J. Radiol.* **1973**, *46*, 1016.

21. Brooks, R.A.; DiChiro, G. *Phys. Med. Biol.* **1976**, *21*, 689.

22. Lai, C.M.; Lauterbur, P.C. *J. Phys. E.* **1980**, *13*, 747.

23. Johnson, G.A.; Glover, G.H.; Karis, J.P. *Radiology* **1986**, *161*, 254.

24. Hoult, D.I. *Br. Med. Bull.* **1984**, *40*, 132-138.

25. Bottomley, P.A. *Rev. Sci. Instr.* **1982**, *53*, 1319-1330.

26. Crooks, L.E.; Ortendahl, D.A.; Kaufman, L. *Radiology* **1983**, *146*, 123-128.

27. Ernst, R.R. *Quart. Rev. Biophysics* **1987**, *19*, 183-220.

28. Wehrli, F.W.; Shaw, D.; Kneeland, B. *Principles, Methodology and Applications of Biomedical Magnetic Resonance Imaging*; VCH Publishers: New York, 1987.

29. Edelstein, W.A.; Hutchinson, J.M.; Johnson, G.; Redpath, T.W. *Phys. Med. Biol.* **1980** *25*, 751-756.

30. Young, I.R. *J. Comput. Assist. Tomogr.* **1986**, *10*, 271-286.

31. Ra, J.B.; Hilal, S.K. *Magn. Reson. Med.* **1986** *3*, 296-302.

32. Brateman, L. *AJR* **1986**, *146*, 971.

33. Guilfoyle, D.N.; Mansfield, P. *Magn. Reson. Med.* **1985**, *2*, 479.

34. Ordidge, R.J.; Van de Vyver, F.L. *Radiology* **1985**, *157*, 551.

35. Young, H.N.; Kormas, D.W. *Radiology* **1986**, *159*, 783.

36. Claussen, C.; Laniado, M.; Kazner, E.; Schorner, W.; Felix, R. *Neuroradiology* **1985**, *27*, 165.

37. Perman, W.H.; Hilal, S.K.; Simon, H.E.; Maudsley, A.A. *Magn. Reson. Imaging* **1984**, *2*, 23-32.

38. Damadian, R. *Science* **1971**, *171*, 1151-1153.

39. Weisman, I.D.; Benett, L.H.; Maxwell, L.R. *Science* **1972**, *178*, 1288.

40. Hendrick, R.E.; Nelson, T.R.; Hendee, W.R. *Magn. Reson. Imaging* **1984**, *2*, 193-204.

41. Crooks, L.E.; Arakawa, M.; Hoenninger, J. *Radiology* **1984**, *151*, 127.

42. Hoult, D.I.; Lauterbur, P.C. *J. Magn. Reson.* **1979**, *34*, 425.

43. Sloane, R.M.; Buck, L.L.; Fitzsimmons, J.R. *Radiology* **1985**, *158*, 531.

44. Wesbey, G.E.; Engelstad, B.L.; Brasch, R.C. *Physiol. Chem. Phys. Med. NMR* **1984**, *16*, 145-155.

45. Brasch, R.C.; Ogan, M.D.; Engelstad, B.L. *Contrast Media: Biologic Effects in Clinical Applications*; CRC Press: Boca Raton, 1987.

46. Claussen, C.; Laniado, M.; Kazner, E. *Neuroradiology* **1985**,*27*, 164-171.

47 Boudreaux, E.A.; Mulay, L.N. *Theory and Application of Molecular Paramagnetism*; John Wiley and Sons: New York, 1976.

48. Bloch, F.; Hansen, W.W.; Packard, P. *Phys. Rev.* **1946**, *70*, 474-485.

49. Bloembergen, N.; Purcell, E.M.; Pound, R.V. *Phys. Rev.* **1948**, *73*, 679-712.

50. Reuben, J. *Biochemistry* **1971**, *10*, 2834-2838.

51. Wolf, G.L.; Joseph, P.M.; Goldstein, E.J. *AJR* **1986**, *147*, 367-371.

52. Young, I.R.; Clarke, G.J.; Bailes, D.R.; Pennock, J.M.; Doyle, F.H.; Bydder, G.M. *CT: Journal of Computerized Tomography* **1981**, *5*, 543-546.

53. Pauling, L.; Coryell, C.D. *Proc. Natl. Acad. Sci.* **1936**, *22*, 210-226.

54. Stone, T.J.; Buckman, T.; Nordio, P.L.; McConnell, H.M. *Proc. Nat. Acad. Sci. USA* **1965**, *54*, 1010.

55. Lavin, J.D.; Wesbey, G.E.; Engelstad, B.L.; Brasch, R.C.; Ehman, R.L. *Magn. Reson. Imaging* **1985**, *3*, 73-81.

56. Brasch, R.C.; London, D.A.; Wesbey, G.E.; Tozer, T.N.; Williams, R.D.; Lallemand, D.P. *Radiology* **1983**, *147*, 773.

57. Brasch, R.C.; Nitecki, D.E.; Enzmann, D.R.; Wesbey, G.E. *AJNR* **1983**, *4*, 1035.

58. Wesbey, G.E.; Brasch, R.C.; Engelstad, B.L.; Ehman, R.; Lavin, J. *J. Am. Coll. Cardiol.* **1984**, *3*, 510.

59. Brasch, R.C.; Ehman, R.L.; Wesbey, G.E.; Williams, R.D. *Radiology* **1983**, *149*, 99.

60. Couet, W.R.; Brasch, R.C.; Sasnovsky, G.; Tozer, T.N. *Magn. Reson. Imaging* **1985**, *3*, 83-88.

61. Griffith, L.K.; Rosen, G.M.; Rauchman, E.J.; Drayer, B.P. *Invest. Radiol.* **1984**, *19*, 553.

62. Afzol, V.; Brasch, R.C.; Nitecki, D.E.; Wolff, S. *Invest. Radiol.* **1984**, *19*, 549-552.

63. Runge, V.M.; Stewart, R.G.; Lukehart, C.M.; Partain, C.L.; James, A.E. *Radiology* **1984**, *147*, 789.

64. Kang, Y.S.; Gore, J.C.; Armitage, I.M. *Mag. Reson. Med.* **1984**, *1*, 396.

65. Caille, J.M.; Lemanceau, B.; Bonnemain, B. *AJNR* **1983**, *4*, 1041.

66. Lauterbur, P.C.; Mendoca-Dias, M.H.; Ruden, A.M. *Frontiers in Biological Energetics*; Academic Press: New York, 1978; pp 752-759.

67. Brady, T.J.; Goldman, M.R.; Pykett, I.L.; Buonanno, F.S.; Kistler, J.P.; Hinshaw, W.S.; Pahost, G.M. *Radiology* **1984**, *144*, 343.

68. Young, I.R.; Clark, G.J.; Gailes, D.R.; Pennock, J.M.; Doyle, F.H.; Bydder, G.M. *Comp. Tomogr.* **1981**, *5*, 534.

69. Wesbey, G.E.; Brasch, R.C.; Engelstad, B.L.; Crooks, L.E. *Radiology* **1983**, *149*, 175.

70. Caille, J.M.; Kien, P.; Lemancean, B.; Bonnemain, B. *Invest. Radiol.* **1984**, *19*, 149.

71. Browning, E. *Toxicity of Industrial Metals*; Appleton-Century Crofts: New York, 1969.

72. Wolf, G.L.; Baum, L. *Am. J. Roenten.* **1983**, *141*, 193.

73. Chilton, H.M.; Jackels, S.C.; Hinson, W.H.; Ekstrand, K.E. *J. Nucl. Med.* **1984**, *25*, 604-607.

74. Runge, V.M.; Clanton, J.A.; Partain, C.L.; *Invest. Radiol.* **1984**, *19*, 408.

75. Engelstad, B.L.; Wesbey, G.E.; Huberty, J.P.; Mosely, M.E.; McNamara, M.T.; Brasch, R.C. *Invest. Radiol.* **1984**, *19*, 149.

76. Burnett, K.R.; Wolf, G.L.; Shumocher, H.R.; Goldstein, E.J. *Magn. Reson. Imaging* **1985**, *3*, 65-71.

77. Levine, W.G. *The Chelation of Heavy Metals*; Permangon Press: Oxford, 1984.

78. Carr, D.H.; Brown, J.; Leung, A.; Pennock, J.M. *J. Comp. Assist. Tomogr.* **1984**, *8*, 385.

79. Koenig, S.H.; Boglin, C.; Brown, R.D. *Magn. Reson. Med.* **1984**, *1*, 478.

80. Lauffer, R.B.; Brady, T.J. *Magn. Reson. Imaging* **1985**, *3*, 11-16.

81. Schreve, P.; Aisen, A.M. *Magn. Reson. Med.* **1986**, *3*, 336-340.

82. Runge, V.M.; Clanton, J.A.; Lukehart, C.M.; Mallard, J.R.; Partain, C.L.; James, A.E. *Radiology* **1984**, *152*, 123.

83. Runge, V.M.; Claussen, C.; Felix, R.; James, A.E. *Contrast Agents in Magnetic Resonance Imaging*; Excerpta Medica: Princeton, 1986.

84. Gadian, D.G. *J. Comput. Assist. Tomogr.* **1985**, *9*, 242.

85. Pople, J.A.; Schneider, W.G. Bernstein, H.J. *High Resolution Nuclear Magnetic Resonance*; McGraw Hill: New York, 1958; p 209.

86. Weinmann, H.J.; Brasch, R.C.; Press, W.R.; Wesbey, G.E. *AJR* **1984**, *142*, 619-624.

87. Weinmann, H.J.; Laniado, M.; Mutzel, M. *Physiol. Chem. Phys. Med. NMR* **1984**, *16*, 167-172.

88. Carr, D.H.; Bydder, G.M.; Brown, J.; Weinmann, H.J.; Thomas, D.J.; Speck, U.; Young, I.R. *Lancet*, **1984**, *1*, 484-486.

89. Felix, R.; Schoerner, W.; Laniado, M. *Radiology* **1985**, *156*, 681-688.

90. Claussen, C.; Laniado, M.; Kazner, E.; Schoerner, W.; Felix, R. *Neuroradiology* **1985**, *27*, 164-171.

91. Bydder, G.M. *J. Comput. Assist. Tomogr.* **1985**, *9*, 847.

92. Brasch, R.C.; Weinmann, H.J.; Wesbey, G.E. *AJR* **1984**, *142*, 625-630.

93. McNamara, M.T.; Higgins, C.B.; Ehman, R.L.; Rivel, D.; Seivers, R.; Brasch, R.C. *Radiology* **1984**, *153*, 157.

94. Hnatowich, D.J.; Layne, W.W.; Childs, R.L.; Lanteigne, D.; Davis, M.A.; Griffin, T.W.; Daherty, P.W. *Science* **1983**, *220*, 613.

95. Krejcarek, G.E.; Tucker, K.L. *Biochem. Biophys. Res. Comm.* **1977**, *77*, 581.

96. Lauffer, R.B.; Koenig, S.H.; Brown, R.D.; Brady, T.J. *Radiology* **1984**, *153*, 145.

97. Brady, T.J.; Rosen, B.R.; Gold, H.K.; Haber, E. *Magn. Reson. Med.* **1984**, *1*, 286.

98. McNamara, M.T.; Ehman, R.L.; Quay, S.C.; Epstein, A.L. Schmidt, H.; Brasch, R.C. *Radiology* **1984**, *153*, 292.

99. Nelson, J.A.; Jackson, L.; Burnham, B. *Invest. Radiol.* **1984**, *19*, 20.

100. Patronas, N.J.; Knap, R.H.; Cohen, J.S.; Dwyer, A.J.; Colcher, D.; Lundy, J.; Doppman, J.L. *Radiology* **1984**, *153*, 171.

101. Bangham, A.D.; Standish, M.M.; Watkins, J.C. *J. Mol. Biol.* **1965**, *13*, 238-252.

102. Scherphof, G.; Roerdink, F.; Hoekstra, D.; Zborowski, J.; Wisse, R. *Liposomes in Biological Systems*; Wiley: New York, 1980; pp 179-209.

103. Roerdink, F.; Regts, J.; Van Leeuwen, B.; Scherphof, G. *Biochem. Biophys. Acta* **1984**, *770*, 195-202.

104. Weinstein, J.N.; Leserman, L.D. *Pharmacol. Ther.* **1984**, *24*, 207-233.

105. Yatvin, M.B.; Lelkes, P.J. *Med. Phys.* **1982**, *19*, 149.

106. Szoka, F.; Papahadjopoulos, D. *Annu. Rev. Biophys. Bioeng.* **1980**, *9*, 467-508.

107. Schwendener, R.A.; Supersaxo, A.; Rubas, W.; Wider, H.G. In *Liposomes as Drug Carriers*; K. H. Schmidt, Ed.; Stuttgart: Theime, 1986; pp 170-181.

108. Caride, V.J.; Sastman, H.D.; Winchell, R.J.; Gore, J.C. *Magn. Reson. Imaging* **1984**, *2*, 107-112.

109. Parasassi, T.; Bombieri, G.; Conti, F.; Croatto, V. *Inorg. Chim. Acta* **1985**, *106*, 135-139.

110. Magin, R.L.; Wright, S.M.; Neisman, M.R.; Chan, H.C.; Swartz, H.M. *Magn. Reson. Med.* **1986**, *3*, 440-447.

111. Navon, G.; Panigel, R.; Valensen, G. *Magn. Reson. Med.* **1986**, *3*, 876.

112. Borkowski, G.P.; Buonocore, E.; George, C.R. *J. Comput. Assist. Tomogr.* **1983**, *7*, 768-774.

113. Buonocore, E.; Borkowski, G.P.; Paulicek, W.; Ngo, F. *AJR* **1983**, *141*, 1171-1178.

114. Strich, G.; Hagan, P.L.; Gerber, K.H.; Slutsky, R.A. *Radiology* **1985**, *154*, 723-726.

115. Laniado, M.; Weinmann, H.J.; Schoerner, W.; Felix, R.; Speck, U. *Physiol. Chem. Phys. Med. NMR* **1984**, *16*, 157-165.

116. Kabalka, G.; Buonocore, E.; Hubner, K.; Moss, T.; Norley, N.; Huang, L. *Radiology* **1987**, *163*, 255-258.

117. Kabalka, G.; Buonocore, E.; Hubner, K.; Huang,L.; Moss, T.; Norley, N. In *Contrast Agents in Magnetic Resonance Imaging*; V. M. Runge, C. Claussen and A. E. James, Eds.; Excerpta Medica: Princeton, 1986; pp 88-91.

118. Hnatowich, D.J.; Friedman, B.; Clancy, B.; Novak, M. *J. Nucl. Med.* **1981**, *22*, 810-814.

119. Eckelman, W.C.; Karesh, S.M.; Reba, R.C. *J. Pharmacol. Sci.* **1975**, *64*, 704-706.

120. Adrian, G.; Huang, L. *Biochemistry* **1979**, *18*, 5610-5614.

121. Moss, T.M.; MS Thesis, University of Tennessee, Knoxville, 1986.

122. Stryer, L. *Biochemistry*; W. H. Freeman and Company: San Francisco, 1975; p 207.

123. Carey, F.A.; Sandberg, R.J. *Advanced Organic Chemistry: Structure and Mechanisms*; Plenum Press: New York, 1977; p 341.

124. Kabalka, G.W.; Buonocore, E.; Hubner, K.; Davis, M.; Huang, L. *Magn. Reson. Med.* **1988**, *8*, 89-95.

125. Nystrom, R.F.; Brown, W.G. *J. Am. Chem. Soc.* **1947**, *69*, 2548-2549.

126. March, J. *Advanced Organic Chemistry*; John Wiley and Sons: New York, 1985; p 347.

127. Fersht, A.R.; Jencks, W.P. *J. Am. Chem. Soc.* **1970**, *92*, 5432.

128. Lehninger, A.L. *Principles of Biochemistry*; Worth Publishers: New York, 1982; p 513.

129. Janssen, M.J. In *The Chemistry of Carboxylic Acids and Esters*; S. Patai, Ed.; Interscience Publishers: New York, 1969; pp 705-764.

130. Satchell, D.P. *Q. Rev. Chem. Soc.* **1963**, *17*, 182-184.

131. Nakamato, K. *Infrared and Raman Spectra of Inorganic and Coordination Compounds*; John Wiley and Sons: New York, 1986; pp 189-371.

132. Swaminathon, K.; Busch, D.H. *J. Inorg. Nucl. Chem.* **1961**, *20*, 159.

133. Weast, R.C.; Astle, M.J.; Beyer, W.H., Eds. *CRC Handbook of Chemistry and Physics*; CRC Press: Boca Raton, 1987.

134. Welch, M.J.; Welch, T.J. In *Radiopharmaceuticals*; G. Subramanian, B.A. Rhodes, J.F. Cooper and V.J. Sodd, Eds.; Society of Nuclear Medicine, Inc.: New York, 1975; p 75.

135. Maudsley, A.A. In *Magnetic Resonance Imaging; Physical Principles and Instrumentation*; C.L. Partain, R. R. Price, J.A. Patton, M.V. Kulkarni and A.E. James, Eds.; W.B. Saunders Co.: Philadelphia, 1988; pp 1584-1589.

136. Weiner, M.W. *Investigative Radiology* **1988**, *23*, 253-262.

137. Chan, L. *West. J. Med.* **1985**, *143*, 773.

138. Shulman, R.G. *Biological Applications of Magnetic Resonance*; Academic Press: New York, 1979.

139. Bottomly, P.A.; Foster, T.B.; Darrow, R.D. *J. Mag. Reson.* **1984**, *59*, 338-342.

140. Bottomly, P.A.; Smith, L.S.; Leue, W.M.; Charles, C. *J. Mag. Reson.* **1985**, *64*, 347-351.

141. Ordidge, R.J.; Connelly, A.; Lahman, J. A. B. *J. Mag. Reson.* **1986**, *66*, 283-294.

142. Ackerman, J.J.H.; Grave, T.H.; Wang, G.G.; Gadian, D.G.; Radda, G.K. *Nature* **1980**, *283*, 167-170.

143. Chance, B.; Leigh, J.S.; McLaughlin, A.C.; Schnall, M.; Sinnwell, T. In *Magnetic Resonance Imaging; Physical Principles and Instrumentation*; C.L. Partain, R.R. Price, J.A. Patton, M.V. Kulkarni and A. E. James, Eds.; W.B. Saunders Co.: Philadelphia, 1988; pp 1501-1520.

144. Hoult, D.I.; Busby, S.J.W.; Gadian, D.G.; Radda, G.K.; Richards, R.E.; Seeley, P.J. *Nature* **1974**, *252*, 285-287.

145. Nuccitelli, R.; Webb, D.J.; Logier, S.T. *Proc. Natl Acad. Sci. USA* **1981**, *78*, 4421.

146. Radda, G.K.; Taylor, D.J.; Styles, P. *Magn. Reson. Med.* **1983**, *1*, 286.

147. Taylor, D.J.; Bare, P.J.; Styles, P. *Med. Biol. Med.* **1983**, *1*, 77.

148. Ross, B.D.; Radda, G.K.; Gadian, D.G.; Rocker, G.; Esiri, M. *N. Engl. J. Med.* **1981**, *304*, 1338-1342.

149. Chance, B.; Eleff, S.; Bank, W.; Leigh, J.S.; Wornell, R. *Proc. Nat. Acad. Sci. USA* **1982**, *79*, 7714-7718.

150. Matson, G.B.; Weiner, M.W. In *Magnetic Resonance Imaging;* D.D. Stark and W.G. Bradley, Eds.; C.V. Mosby Co.: Washington D.C., 1988; pp 201-228.

151. Gadian, D.G.; Hoult, D.I.; Radda, G.K.; Chance, B. *Proc. Nat. Acad. Sci. USA* **1976**, *73*, 4446-4448.

152. Garlick, P.B.; Radda, G.K.; Seeley, P.J.; Chance, B. *Biochem. Biophys. Res. Commun.* **1977**, *74*, 1256-1262.

153. Jacobus, W.E.; Taylor, G.J.; Hollis, D.P.; Nunnally, R.L. *Nature* **1977**, *265*, 756-758.

154. Jacobus, W.E.; Taylor, G.J.; Weisfeldt, M.L.; Nunnally, R.L. In *Biomolecular Structure and Function*; P.F. Agris, Ed.; Academic Press: New York, 1978; pp 207-215.

155. Gorlick, P.B.; Radda, G.K.; Seeley, P.J. *Biochem. J.* **1979**, *184*, 547-554.

156. Bailey, I.A.; Williams, S.R.; Radda, G.K.; Gadian, D.G. *Biochem. J.* **1981**, *196*, 171-178.

157. Grove, T.H.; Ackerman, J.J.H.; Radda, G.K.; Bore, P.J. *Proc. Natl. Acad. Sci. USA* **1980**, *77*, 299-302.

158. Koretsky, A.P.; Wang, S.; Klein, M.P.; James, T.L.; Weiner, M.W. *Proc. Natl. Acad. Sci. USA* **1983**, *80*, 7491-7495.

159. Kantar, H.L.; Briggs, R.W.; Balabon, R.O.S. *Circ. Res.* **1984**, *55*, 261-266.

160. Toyo-Oka, T.; Nagayama, K.; Umeda, M.; Eguchi, K.; Hasasda, S. *Biochem. Biophys. Res. Commun.* **1986**, *135*, 808-815.

161. Seymour, A.L.; Keaugh, J.M.; Radda, G.K. *Biochem. Soc. Trans.* **1983**, *11*, 376-377.

162. Barbour, R.L.; Satak, C.H.; Levy, G.C.; Chan, S.H. *Biochemistry* **1984**, *23*, 6053-6062.

163. Bernard, M.; Menosche, P.; Fontanacava, E. *Clin. Chim. Acta* **1985**, *152*, 43-53.

164. Seymour, A.L.; Bailey, I.A.; Radda, G.K. *Biochem. Biophys. Acta* **1983**, *762*, 525-530.

165. Chance, B.; Nakase, Y.; Bond, M.; Leigh, J.S.; McDonald, G. *Proc. Natl. Acad. Sci. USA* **1978**, *75*, 4925-4929.

166. Prichard, J.W.; Shulman, R.G. *Annu. Rev. Neurosci.* **1986**, *9*, 61.

167. Bottomley, P.A.; Kogure, K.; Noman, R. *Magn. Reson. Imaging* **1982**, *1*, 81.

168. Prichard, J.W.; Alger, J.R.; Behar, K.L. *Proc. Natl. Acad. Sci. USA* **1983**, *80*, 2748.

169. Thulborn, K.R.; du Boulay, G.; Radda, G.K. *J. Cereb. Blood Flow Metab.* **1981**, *1*, 580.

170. Cohen, S.M.; Ogawa, S.; Rottenburg, H.; Glynn, P.; Yamane, Y.; Brown, T.R. *Nature* **1978**, *273*, 554-556.

171. Iles, R.A.; Griffiths, J.R.; Stevens, A.M.; Gadian, D.G.; Parteous, R. *Biochem. J.* **1980**, *192*, 191-202.

172. Radda, G.K.; Sehr, P.B.; Bore, P.J.; Sells, R.A. *Biochem. Biophys. Res. Commun.* **1977**, *77*, 195-202.

173. Ackerman, J.J.H.; Lowry, M.; Radda, G.K.; Ross, B.D.; Wang, G.G *J. Physiol.* **1981**, *319*, 65-79.

174. Evanochko, W.T.; Ng, T.C.; Glickson, J.P. *Magn. Reson. Med.* **1984**, *1*, 508-534.

175. Griffiths, J.R.; Stevens, A.N.; Iles, R.A.; Gordon, R.E.; Shaw, D. *Biosci. Rep.* **1981**, *1*, 319-325.

176. Ng, T.C.; Evanochko, W.T.; Hiromato, R.N. *J. Magn. Reson.* **1982**, *49*, 271-286.

177. Naruse, S.; Hirokawa, K.; Horikawa, Y. *Cancer Res.* **1985**, *45*, 2429-2433.

178. Naruse, S.; Horikawa, Y. Tanaka, C. *Radiology* **1986**, *160*, 827-830.

179. Maudsley, A.A.; Hilal, S.K.; Seman, H.E. *Magn. Reson. Med.* **1984**, *1*, 202-203.

180. Cameron, I.L.; Smith, N.K.; Pool, T.B.; Sparks, R.L. *Cancer Res.* **1980**, *40*, 1493-1500.

181. Moore, R.D.; Munford, J.W.; Pillsworth, T.J. *J. Physiol. (Lond.)* **1983**, *338*, 277-294.

182. Blaustein, M.P. *Am. J. Physiol.* **1977**, *232*, 165-175.

183. Civan, M.M.; Shporer, M. In *Biological Magnetic Resonance*; L.J. Berlinear and J. Reuben, Eds.; Plenum Press: New York, 1978; pp 1-32.

184. Belton, P.S.; Ratcliffe, R.G. *Prog. Nucl. Magn. Reson. Spectrosc.* **1985**, *17*, 241-279.

185. Springer, C. *Ann. Rev. Biophys. Chem.* **1987**, *16*, 375-399.

186. Dos, T.P.; Hahn, E.L. *Nuclear Quadrapole Resonance Spectroscopy*; Academic Press: New York, 1958.

187. Abragam, A. *The Principles of Nuclear Magnetism*; Oxford University Press: London, 1961.

188. Cope, F.W. *Proc. Natl. Acad. Sci. USA* **1965**, *54*, 225-227.

189. Martinez, D.; Silvidi, A.A.; Stokes, R.M. *Biophys. J.* **1969**, *9*, 1256-1260.

190. Cope, F.W. *Biophys. J.* **1970**, *10*, 843-858.

191. Hubbard, P.S. *J. Chem. Phys.* **1970**, *53*, 985-989.

192. Bull, T.E. *J. Magn. Reson.* **1972**, *8*, 344-353.

193. Pike, M.M.; Springer, C.S. *J. Magn. Reson.* **1982**, *46*, 348-353.

194. Gupta, R.K.; Gupta, P. *J. Magn. Reson.* **1982**, *47*, 225-227.

195. Chu, S.C.; Pike, M.M.; Fossel, E.T.; Smith, T.W.; Springer, C.S. *J. Magn. Reson.* **1984**, *56*, 33-47.

196. Balschi, J.A.; Cirillo, V.; Springer, C.S. *Biophys. J.* **1982**, *38*, 323-326.

197. Castle, A.M.; Macnab, R.M.; Shulman, R.G. *J. Biol. Chem.* **1986**, *261* 3288-3294.

198. Pike, M.M.; Fossel, E.T.; Smith, T.W.; Springer, C.S. *Am. J. Physiol.* **1984**, *246*, 528-536.

199. Burnstein, D.; Fossel, E.T. *Magn. Reson. Med.* **1987**, *4*, 261-273.

200. Matweyoff, N.A.; Gasparavic, C.; Wenk, R.; Wicks, J.D.; Roth, A. *Magn. Reson. Med.* **1986**, *3*, 164-168.

201. Pike, M.M.; Frazer, J.C.; Dedrick, D. *Biophys. J.* **1985**, *48*, 159-173.

202. Blum, H.; Schnall, M.D.; Buzby, G.P.; Chance, B. *Soc. Magn. Reson. Med. (abstract)* **1986**, *2*, 339.

203. Balschi, J.A.; Bittle, J.A.; Ingwall, J.S. *Soc. Magn. Reson. Med (abstract)* **1986**, *2*, 343-344.

204. Berendsen, H.J.; Edzes, H.T. *Ann. NY Acad. Sci.* **1973**, *204*, 459-485.

205. Cameron, I.L.; Smith, N.K.; Pool, T.B.; Sparks, R.L. *Cancer Res.* **1980**, *40*, 1493-1500.

206. Burnstein, D.; Fossel, E.T. *Magn. Reson. Med.* **1987**, *4*, 261-273.

207. Shinar, H.; Navon, G. *Magn. Reson. Med.* **1986**, *3*, 927-934.

208. Hilal, S.K.; Ra, J.B.; Oh, C.H.; Mun, I.K.; Einstein, S.G.; Raschmann, P. In *Magnetic Resonance Imaging*; D.D. Stark and W.G. Bradley, Eds.; C.V. Mosby Company: St. Louis, 1988; pp 715-731.

209. Hilal, S.K.; Maudsley, A.A.; Ra, J.B. *J. Comput. Assist. Tomogr.* **1985**, *9*, 1-7.

210. Hilal, S.K.; Maudsley, A.A.; Bann, J. *Magn. Reson. Med.* **1984**, *1*, 165-166.

211. Hilal, S.K.; Maudsley, A.A.; Simon, H.E. *Am. J Neuroradiol.* **1983**, *4*, 245-249.

212. Ra, J.B.; Hilal, S.K.; Oh, C.H. *Radiology* **1985**, *157*, 60.

213. Simon, H.E.; Hilal, S.K.; Maudsley, A.A. *Appl. Radiol.* **1986**, *15*, 77.

214. Cohen, S.M. In *Magnetic Resonance Imaging; Physical Principles and Instrumentation*: C.L. Partain, R.R. Price, J.A. Patton, M.V. Kulkarni and A.E. James, Eds.; W.B. Saunders Co.: Philadelphia, 1988; pp 1521-1535.

215. Scott, A.I.; Baxter, R.I. *Ann. Rev. Biophys. Bioeng.* **1981**, *10*, 151.

216. Thomas, S.R. In *Magnetic Resonance Imaging; Physical Principles and Instrumentation;* C.L. Partain, R.R. Price, J.A. Patton, M.L. Kulkarni and A.E. James, Eds.; W.B. Saunders Co.: Philadelphia, 1988; pp 1536-1552.

217. Nakoda, T.; Kwee, I.L.; Canboy, C.B. *J. Neurochem.* **1986**, *46*, 198.

218. Locker, G.L. *Amer. J. Roentgenol.* **1936**, *36*, 1.

219. Matsumoto, T.; Aizawa, O. *Phys. Med. Biol.* **1985**, *30*, 897.

220. Morris, K.J.; Batchelor, A.L. *Phys. Med. Biol.* **1987**, *32*, 1501.

221. Schremmer, J.M.; Noonan, D.J. *Med. Phys.* **1987**, *14*, 818.

222. Taylor, H.J.; Goldhaber, M. *Nature (London)* **1935**, *135*, 341.

223. Baum, R.M. *Chemical and Engineering News* **1988**, *66 (44)*, 18-22.

224. Soloway, A.H.; Wright, R.L.; Messer, J.R. *J. Pharmacol. Exp. Ther.* **1961**, *134*, 117.

225. Fairchild, R.G.; Goodman, L.J. *Phys. Med. Biol.* **1966**, *2*, 15.

226. Zamehof, R.G.; Murray, B.W.; Brownell, G.L.; Wellum, G.R.; Tolpin, E.I. *Medical Physics* **1975**, *2*, 47.

227. Zamehof, R.G.; Harling, O.K.; Bernard, J.A. In *Clinical Aspects of Neutron Capture Therapy*; R.G. Fairchild, V.P. Bond and A.D. Woodhead, Eds.; Plenum Press: New York, 1989; pp 121-134.

228. Slatkin, D.N.; Micca, P.; Forman, A.; Golsel, D.; Wielopolski, L.; Fairchild, R. *Biochem. Pharmacol.* **1986**, *35*, 1771.

229. Slatkin, D.N.; Joel, D.D.; Fairchild, R.G.; Micca, P.L.; Nawrocky, M.M.; Laster, B.H.; Coderre, J.A.; Finkel, G.C.; Poletti, C.E.; Sweet, W.H. In *Clinical Aspects of Neutron Capture Therapy*; R.G. Fairchild, V.P. Bond and A.D. Woodhead, Eds.; Plenum Press: New York, 1989; pp 179-191.

230. Coderre, J.A.; Glass, J.D.; Fairchild, R.G.; Ray, V.; Cohen, S.; Fond, I. *Cancer Research* **1987**, *47*, 6377.

231. Alam, F.; Soloway, A.H.; Bopat, B.V.; Barth, R.F.; Adams, D.M. In *Clinical Aspects of Neutron Capture Therapy;* R.G. Fairchild, V.P. Bond and A.D. Woodhead, Eds.; Plenum Press: New York, 1989; pp 107-111.

232. Sweet, W.H. *N. Eng. J. Med.* **1951**, *245*, 875.

233. Kabalka, G.W.; Bendel, P.; Davis, M.A.; Slatkin, D.N.; Micca, P.L. In *Clinical Aspects of Neutron Capture Therapy*; R.G. Fairchild, V.P. Bond and A.D. Woodhead, Eds.; Plenum Press: New York, 1989; pp 243-249.

234. Loeffler, W. In *Nuclear Magnetic Resonance and Correlative Imaging Modalities*; C.L. Partain, Ed.; Society of Nuclear Medicine: New York, 1984; p. 63.

235. Kabalka, G.W.; Davis, M.A.; Bendel, P. *Magn. Reson. Med.* **1988**, *8*, 231-237.

236. Perman, W.H.; Thomasson, D.M.; Bernstein, M.A.; Turski, P.A. *Magn. Reson. Med.* **1989**, *9*, 153.

237. Oh, C.H.; Hilal, S.K.; Mun, I.K.; Cho, Z.H. *Proc. Sixth SMRM, New York* **1987**, 906.

238. Ra, J.B.; Hilal, S.K.; Oh, C.H. *J. Comp. Assist. Tomogr.* **1989**, *13*, 302.

239. Bendel, P.; Davis, M.A.; Berman, E.; Kabalka, G.W. *J. Magn. Reson.*, in press.

240. Mansfield, P.; Chapman, B. *J. Magn. Reson.* **1987**, *72*, 211-223.

241. Wellum, G.R.; Tolpin, E.I.; Soloway, A.H.; Kaczmarczyk, A. *Inorg. Chem.* **1977**, *16*, 2120.

VITA

Mark Allen Davis was born on July 23, 1957 in England. After a series of moves, he settled in Biloxi, Mississippi where he graduated from Biloxi High School in 1975. He attended Mississippi Gulf Coast Junior College in Perkinston, Mississippi where he received an Associate of Science Degree in Radiologic Technology in 1979. After working in this field for a few years, he attended the University of Southern Mississippi in Hattiesburg, Mississippi where he received a Bachelor of Science Degree in Chemistry in 1985. In September 1985, he entered the University of Tennessee, Knoxville and began his graduate studies under the direction of Dr. George W. Kabalka and received a Doctor of Philosophy Degree in Chemistry in May 1990. He has accepted a research chemist position at Ethyl Corporation in Baton Rouge, Louisiana. He married Julia Lyn Woods on January 30, 1988 to whom he remains happily married.